



BACK TO SINGLE-CARRIER FOR BEYOND-5G COMMUNICATIONS ABOVE 90 GHz
GRANT AGREEMENT ANR-17-CE25-0013

D2.1: Propagation channel model and RF impairments definition and waveform design

Authors:

CentraleSupélec (*Editor*): Majed Saad, Nizar Bouhlel,
C. Faouzi Bader

CEA-Leti: Simon Bicaïs, Jean-Baptiste Doré

SIRADEL: Yoann Corre,

Mohammed Zahid Aslam .

Nov. 2020



Contents

1	Introduction	9
2	Propagation channel modelling	9
2.1	Introduction	9
2.2	Outdoor subTHz channel characterization	10
2.2.1	Scenario and Setup	11
2.2.2	Ray-based sub-THz channel model and parameters	12
2.2.3	Channel characterization in the urban canyon case	13
2.2.4	Point-to-point backhaul links	16
2.2.5	Mobile access coverage	16
2.2.6	Fixed Wireless Access (FWA) coverage	17
2.3	Scattering by the vegetation	18
2.4	Conclusions	20
3	RF impairments Modelling	21
3.1	Introduction	21
3.2	System Description	21
3.2.1	Oscillator	21
3.2.2	Channel	22
3.3	Phase Noise Models	23
3.3.1	Correlated phase noise	23
3.3.2	Uncorrelated phase noise	24
3.4	Model Selection	25
3.4.1	Accuracy of the Gaussian model	25
3.4.2	Models comparison	26
3.5	Application to Link Adaptation	30
3.5.1	BER analysis for PSK and DPSK	30
3.5.2	Adaptive systems	31
3.6	Conclusion	32
4	Modulation shaping for phase noise channel	34
4.1	Introduction	34
4.2	System Model	35
4.2.1	Channel model	35
4.2.2	Phase noise model	35
4.3	Receiver Algorithms Design	36
4.3.1	Optimum demodulation	36
4.3.2	Channel estimation	42
4.4	Modulation Scheme Design	43
4.4.1	Optimum constellation from sphere packing	43
4.4.2	Performance of constellations based on polar-lattices	45
4.4.3	Polar-QAM	47
4.4.4	Theoretical performance analysis	49
4.4.5	Numerical simulations results	51



4.4.6	Comparative studies	53
4.5	Applications & Perspectives	55
4.5.1	Link adaptation	56
4.5.2	Beyond memoryless phase noise	57
4.5.3	Perspectives	57
4.6	Conclusion	58
5	MIMO Schemes and waveform design	59
5.1	Introduction	59
5.2	Generalized Spatial Modulation (GSM) MIMO System	60
5.2.1	System and Channel Models	60
5.2.2	Channel Model	62
5.2.3	Performance analysis	63
5.2.4	Link budget and discussion	66
5.2.5	General conclusions	70
5.3	Generalized Spatial Modulation in Highly Correlated Channels	71
5.3.1	Channel Model	71
5.3.2	Transmit Antenna Combination Selection	71
5.3.3	GSM System Relying on Channel State Information (EGSM)	72
5.3.4	Simplified GSM System (S-EGSM)	73
5.3.5	Index-to-Bit Mapping: Spatial Mapping	73
5.3.6	Simulations results and discussions	75
5.3.7	General conclusions	79
5.4	Dual Polarized Generalized Spatial Modulation Scheme	80
5.4.1	Introduction	80
5.4.2	System model: Dual-Polarized GSM system	81
5.4.3	Joint-ML Detector	82
5.4.4	Modified OB-MMSE Detector	82
5.4.5	Channel model	84
5.4.6	Performance analysis	85
5.4.7	Performance with real sub-THz MIMO Channel	90
5.5	General conclusions	93
6	Deliverable final conclusions	94

List of Figures

1	Study main principles.	11
2	Considered area including all three scenarios.	12
3	Scenarios in (a) urban canyon, (b) residential, and (c) main street environments.	13
4	Scenario parameters.	14
5	Significant simulated paths for the urban canyon P2P links at height 3 m.	15
6	Significant simulated paths for the urban canyon P2P links at height 6 m.	15
7	Average number of significant paths per P2P LoS link.	17
8	Rx power map around two different nodes.	17
9	Average covered area per node for different heights.	18
10	Average covered facade length per node for different heights.	18
11	Propagation paths diffused by the vegetation.	19
12	Simulated path contributions due to the vegetation diffusion.	19
13	PSD of the considered 200 GHz oscillator [1].	22
14	PSD of the considered correlated PN model.	24
15	Frequency of accepting the Gaussian model H_0 with a χ^2 goodness of fit test for simulated correlated PN.	27
16	Frequency of accepting the Gaussian model H_0 with a χ^2 goodness of fit test for simulated realistic PN.	27
17	Mean value of LLR $\Lambda_{G/W}$ on simulated correlated PN.	30
18	Mean value of LLR $\Lambda_{G/W}$ on simulated realistic PN.	31
19	BER performance of PSK and DPSK for correlated PN.	32
20	16-QAM Voronoi regions	39
21	Performance of a low-density parity check (LDPC) coded 16-QAM with LLR based on the Euclidean distance or on the polar metric for different phase noise (PN) variances σ_ϕ^2	41
22	Voronoi regions for the polar metric of polar-lattice based constellations with 16 signal points	44
23	BER performance of different constellations with $M = 16$ on the GPN channel	45
24	Achievable rates in bit/symbol for different constellations and $M = 16$	46
25	Illustration of a 16-PQAM(2) in the complex plane	47
26	Binary labeling of a 16-PQAM(4)	49
27	Analytical performance of a 16-PQAM(Γ) for modulation shape $\Gamma \in \{4, 8, 16\}$ with PN variance $\sigma_\phi^2 = 1.25 \times 10^{-1}$	50
28	16-QAM and 16-PQAM(8) performance with PN variance $\sigma_\phi^2 = 1.25 \times 10^{-1}$	51
29	Achievable rate in bit/symbol of the QAM and PQAM schemes with a LDPC code and PN variance $\sigma_\phi^2 = 10^{-1}$	52
30	Comparison of PQAM to the spiral constellation [2] with $M = 64$ and $\sigma_\phi^2 = 10^{-1}$	54
31	Spiral and PQAM constellations in ℓ^2 (first row) and in p^2 (second row)	54
32	PQAM parameters M and Γ with the highest spectral efficiency such that $\text{BER} < 10^{-4}$	56
33	System Model	61
34	GSM Derivatives	62

35	Minimum number of required RF chains for GSM and BLAST systems as function of APM spectral efficiency. The system spectral efficiency for both systems (BLAST and GSM) with any APM spectral efficiency (0.8–10 b/s/Hz) is in the order of 25 b/s/Hz.	64
36	BER vs SNR for various systems over uncorrelated Rayleigh channel	65
37	BER vs SNR for various systems over uncorrelated Ricain channel	66
38	BER vs SNR for (D)QPSK-GSM and CPM-GSM over correlated Rayleigh channel	66
39	BER vs SNR for (D)QPSK-GSM and CPM-GSM over correlated Rician channel	67
40	System comparison between different SC modulations with GSM for achieving a Tb/s (see Table 4)	70
41	System model of GSM with TAC selection	72
42	BER vs E_b/N_0 for various TAC selection with $\beta_t = 0$	77
43	BER vs E_b/N_0 for various TAC selection with $\beta_t = 0.4$	77
44	BER vs E_b/N_0 for various TAC selection with $\beta_t = 0.8$	78
45	BER vs E_b/N_0 for different TAC spatial mapping with $\beta_t = \{0.2, 0.6\}$	78
46	Spatial BER vs E_b/N_0 for binary and gray coding for spatial bits	79
47	$N_r \times N_t$ DP-GSM system model.	81
48	BER performance of $N_r \times N_t$ DP-GSM system with power leakage parameter $\mu = 0.2$ and different APMs (QPSK, DPSK, 16QAM) over uncorrelated Rayleigh channel (Solid line) and uncorrelated Rician channel (Dashed line). The spectral efficiency is 18bpcu.	86
49	BER performance of $N_r \times N_t$ DP-GSM system with spatial correlation $\beta \in \{0.2, 0.5, 0.8\}$, power leakage parameter $\mu = 0.2$ and different APMs (QPSK, DPSK, 16QAM) over a correlated Rayleigh channel. The spectral efficiency is 18bpcu.	87
50	BER performance of $N_r \times N_t$ DP-GSM system with spatial correlation $\beta \in \{0.2, 0.5, 0.8\}$, power leakage parameter $\mu = 0.2$ and different APMs (QPSK, DPSK, 16QAM) over correlated Rician channel ($K = 3$). The spectral efficiency is 18bpcu.	88
51	BER performance of $N_r \times N_t$ DP-GSM system with spatial correlation $\beta \in \{0.2, 0.5, 0.8\}$ and power leakage parameter $\mu = \{0.2, 0.8\}$ for QPSK over correlated Rayleigh channel. The spectral efficiency is 18bpcu for $N_t = 8$, $N_a = 4$ and $N_r = 4$	89
55	BER performance comparison of DP-GSM and DP-SMX systems with spatial correlation $\beta \in \{0.2, 0.8\}$ and power leakage $\mu = 0.2$ over correlated Rayleigh channel (Solid line) and correlated Rician channel (Dashed line) for QPSK using ML detector. The spectral efficiency is 12bpcu.	89
52	BER performance of $N_r \times N_t$ DP-GSM system with spatial correlation $\beta \in \{0.2, 0.5, 0.8\}$ and power leakage parameter $\mu = \{0.2, 0.8\}$ for QPSK over correlated Rician channel ($K = 3$). The spectral efficiency is 18bpcu for $N_t = 8$, $N_a = 4$ and $N_r = 4$	90

53	BER performance comparison of $N_r \times N_t$ DP-GSM system with spatial correlation $\beta \in \{0.2, 0.5, 0.8\}$ and power leakage parameter $\mu = 0.2$ for QPSK over correlated Rayleigh channel (Solid line) and correlated Rician channel (Dashed line) using for both channels MOB-MMSE and ML detectors. The spectral efficiency is 18bpcu.	91
56	In-door MIMO channel measurements [3].	91
54	BER performance comparison of $N_r \times N_t$ DP-GSM and $2N_r \times 2N_t$ UP-GSM system with spatial correlation $\beta \in \{0.2, 0.8\}$ and power leakage $\mu = 0.2$ over correlated Rayleigh channel (Solid line) and correlated Rician channel (Dashed line) for QPSK using MOB-MMSE detector. The spectral efficiency is 18bpcu.	92
57	BER performance of DP-GSM, DP-SMX and UP-GSM systems from sub-THz measurements for QPSK using ML detector. The concerned sub-THz indoor MIMO channels are generated using ULA array geometry with 4λ antenna separation. The spectral efficiency is 12bpcu.	93

List of Tables

1	Spectral density K_0 (dBc/Hz) of the white PN floor.	25
2	Comparison of error floors for different constellations and $\sigma_\phi^2 = 10^{-2}$	53
3	Simulation parameters	64
4	Link Budget and Power Consumption for different GSM parameters achieving Tb/s	69
5	HD matrix for Spatial Mapping example with $N_t = 5$ and $N_a = 2$	75
6	Simulation parameters and a sub-THz system example.	86

List of acronyms

5G-NR 5G new radio

APM amplitude-phase modulators

APSK amplitude-phase-shift keying

AWGN additive white Gaussian noise

BER bit error rate

BICM bit-interleaved coded modulation

BLAST Bell laboratories layered space-time

C2P cartesian-to-polar

CFO carrier frequency offset

CSI channel-state information

CPM continuous phase modulation

CRLB Cramer-Rao lower bounds

DP dual-polarized

EGSM enhanced generalized spatial modulation

ED euclidian distance

FEC forward error correction

FWA fixed wireless access

GPN gaussian phase noise

GSM generalized spatial modulation

IM index modulation

IQ in-phase quadrature

ITU international telecommunication union

LDPC low-density parity check

LiDAR light detection and ranging

LLR log-likelihood ratios

LoS line-of-sight

MC multiple carriers

MI mutual information

ML maximum likelihood

MSE mean squared error

MVUE minimum-variance unbiased estimator

OB-MMSE ordered block minimum mean-squared error

P2F point-to facade

P2P point-to-point

PAPR peak-to-average power ratio

PER packet error rate

PLL phase-locked loop

PN phase noise

PSK phase-shift keying

QAM quadrature amplitude modulation

RF radio-frequency

SC single carrier

SEP symbol error probability

SM spatial modulation

SMX spatial multiplexing

SNR signal-to-noise ratio

TAC transmit antenna combination

TAS transmit antenna set

TPC transmit polarization combinations

THz terahertz

UP-GSM uni-polarized generalized spatial modulation

XPD cross-polarization discrimination

Executive Summary

This technical deliverable D2.1, provides valuable results on propagation channel and RF impairments modelling, proposed waveform, related transceiver architecture/algorithm and initial performance evaluation.

A first and very important achieved result is the achievement in developing tools validated with measurements at 28 GHz and 60 GHz used to analyze the channel propagation at 150 GHz frequency band. As a main observation, the channel at 150 GHz does not necessarily benefit from better conditions at higher node heights (as usually observed at lower frequencies). It can behave significantly different depending on the height of the nodes, power and angular sensitivity of the receiver and the considered transmit power.

The second important achieved result is to be able model the phase noise (PN) for sub-THz communications. We have first introduced two PN models: one correlated, accurate but complex, and another uncorrelated analytically simpler. We have also investigated the design of robust communications impaired by strong PN for future sub-THz applications.

Third, important achievements related with the development of the Generalized Spatial Modulation (GSM) MIMO System scheme for sub-THz communications are presented in this deliverable. Proposed scheme proves that the constant or near-constant envelope modulation CPM-GSM and (D)QPSK-GSM systems with limited number of RF chains, feasible antenna array size, and acceptable complexity are able to reach a high system spectral efficiency $\approx 25\text{b/s/Hz}$, and hence ultra-high data rates while maintaining a low power consumption.

Last but not least, the deployment of the dual polarized antennas in GSM (DP-GSM) allows to add an additional level of indexation and leads to the increase of the spectral efficiency (SE). The DP-GSM system offers the opportunities to be more robust against channel deficiencies such as Rician fading and inter-antenna correlation and to be beneficial for the spectral efficiency.

Keywords: *Sub-THz, Channel modelling and characterization, Sub-THz backhauling, P2P links, FWA, RF impairments, Phase Noise, Link adaptation, Polar metric, Polar-QAM, Link adaptation, Single Carrier, Index Modulation, Generalized Spatial Modulation, Highly Correlated Channels, Transmit antenna combination, Spectral efficiency, Energy efficiency.*

1 Introduction

This technical deliverable D2.1, provides valuable results on propagation channel and RF impairments modelling, proposed waveform, related transceiver architecture/algorithm and initial performance evaluation. It provides models and analysis based on the preliminary outcomes that were published in the BRAVE project's deliverable D2.0 titled "Propagation channel model and RF impairments definition".

First, this document provides in Section 2, new results on outdoor subTHz channel characterization and ray-based channel modelling. Second, a complete and deep analysis on RF impairment modelling is provided in technical works presented in Section 3, where the accuracy and application of two phase noise (PN) models of different complexities are discussed and analytically compared; it is demonstrated as well how the modulation can be optimally adapted according to PN characteristics. Third, the design of robust communications impaired by strong PN for future sub-THz applications is investigated in Section 4, it can be shown in this section that optimizing the communication schemes is essential to realize high rate communications on practical systems impaired by strong PN. Accordingly, the proposed schemes offer valuable low-complexity solutions for future sub-THz systems.

Fourth, a deep analysis work is undertaken in Section 5 related to MIMO schemes and waveform design where efficient modulations schemes for sub-THz and Tbps data rate based on GSM scheme and using index modulation (IM) strategy are presented. More "avant garde" results related to generalized spatial modulation (GSM) with IM scheme in sub-THz under highly correlated channels, and dual polarized GSM scheme is also provided in this last section.

Finally, the reader has in Section 6, the synthesis and the main conclusions of the main developed technical works and the outstanding results presented in this deliverable D2.1.

2 Propagation channel modelling

2.1 Introduction

The modelling of the sub-THz propagation channel is needed for research and test, but the channel understanding is still limited due to the very recent interest and the few available measurements.

It was decided in BRAVE to employ the Volcano ray-tracing tool previously validated in the millimeter-wave in order to characterize the sub-THz channel and support the PHY-layer studies and demonstrations. The adaptation of the tool for higher frequencies was described in a previous BRAVE's deliverable [4]. It was then applied to an in-office scenario to produce statistics on the path-loss, delay spread, and angular spread for frequencies between 2 GHz and 200 GHz, and for different antenna beamwidths. The in-street node-to-node propagation channel was simulated as well at 150 GHz, using LiDAR geo data for accurate prediction of the foliage blockage and attenuation. Path-loss statistics were derived for line-of-sight (LoS), obstructed LoS, and non-LoS situations [4].

In this Section 2, the same ray-based tool is used to further analyze and characterize the outdoor propagation channel at 150 GHz. Different environments like urban canyon, residential and a wide main street are considered, in order to assess the propagation properties

for several outdoor antenna configurations: mesh backhaul, Fixed Wireless Access (FWA) and mobiles access.

2.2 Outdoor subTHz channel characterization

The characterization and modeling of the in-street backhaul at 60 GHz is still in initial stages today [5] and the channel at 150 GHz is mostly unexplored yet. However the in-depth analysis and characterization of such channels is required in order to design appropriate physical-layer technologies, elaborate communications protocols, assess the new systems performance, formulate deployment rules and create reliable radio-planning tools. In [6] measurements at 60 GHz, outdoor backhaul P2P links were obtained using Terragraph nodes as part of the Telecom Infra Project (TIP) [7]. The measurements were performed on the Darmstadt campus of Deutsche Telekom, with different kinds of building façades, medium tree density, and some street furniture. These measurements were used to characterize the propagation properties, but also compare and validate the simulations of the ray-based Volcano model [8] [9]. The simulations were performed using highly accurate representation of the geographical environment, based on LiDAR (Light Detection and Ranging) point cloud data that was collected at street level at the same time as the measurements, i.e. in the summer season when the vegetation contains most of the foliage. The point cloud data was obtained with a density and a measurement protocol that guarantee a precise 3D representation of most trees located in the street.

The measurements were employed for validating the model and adjusting some of its parameters e.g. for vegetation losses, while the measurements and simulations were together analyzed in order to understand the main channel properties by close inspection in the simulation environment. Besides, the simulator provides a very convenient way to explore the channel characteristics in additional non-measured scenarios, e.g. to get a more global insight on the urban backhaul link conditions. This could easily be extended to higher frequencies as well, as the same physics are applied to the environment; the prediction changes occur in the interactions with the environment such as transmission losses, reflection and diffraction losses etc., provided accurate material or medium properties are available.

In [10] the authors explained what simple assumptions have been made to extend the ITU material properties beyond the existing 100 GHz limit until 150 GHz. This extended ray-based Volcano model is utilized here to complement the initial analysis [6] and investigate other scenarios at 60 and 150 GHz. Different propagation environments have been considered: urban canyon with limited vegetation, residential with dense non-uniform vegetation, and a main street with uniform distribution of vegetation. Three potential sub-THz use cases have been reproduced in those environments and studied: dense mesh backhauling based on multiple point-to-point (P2P) links; fixed wireless access towards the building façades; and in-street mobile access. Note this latter use case is not an a priori target for outdoor sub-THz deployments, but it is worth getting a better insight in it. Four different heights of nodes have been compared for backhaul and FWA use cases. Finally, a combined perspective is provided by averaging the characteristics over the considered environments. The followed methodology is summarized in Fig. 1; step 1 was reported in [6] leading to the validation of channel model at 60 GHz, while steps 2 and 3 rely on the ray-tracing capability to adapt; their results are described here below.

The chapter is organized as follows. Sub-section 2.2.1 gives a description of the different

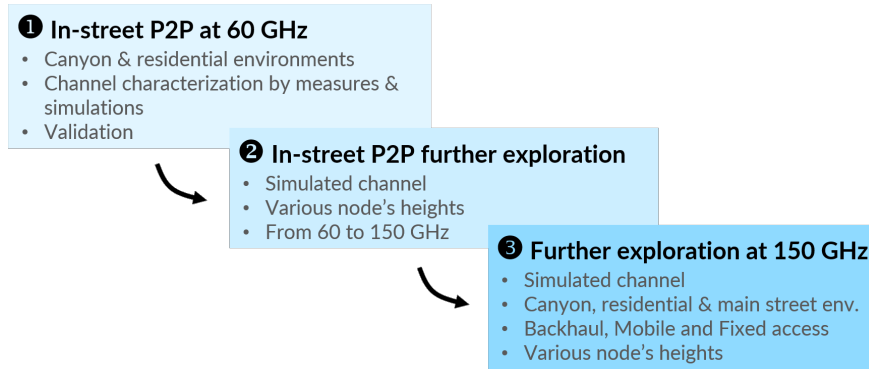


Figure 1: Study main principles.

scenarios used and the simulation setup. The ray-based channel model is introduced in Section 2.2.2. The channel characterization of the urban canyon case at 150 GHz is provided in Section IV. Then the different simulation results for the P2P backhaul links, the mobile access coverage, and the FWA façade coverage are provided in Section 2.2.3. Some perspectives and conclusions are then drawn in Section 2.2.4.

2.2.1 Scenario and Setup

The present study is based on the same scenario as measured and simulated in [6]. The measurement campaign was performed at 60 GHz using Terragraph nodes from the Facebook connectivity initiative [7]. The analysis and validation of the mmWave urban channel model was supported by the accuracy of the obtained same-season LiDAR data in the measurement area. The display of 3D LiDAR point cloud allows for a very accurate and visual understanding of the in-street blockage situations. And its usage by the Volcano ray-based model permits for automatic detection and computation of obstruction losses.

Point-to-point backhaul links in two different environments; urban canyon and residential were considered. Apart from the blockage due to the high frequency, one of the key factors for the channel sparsity observed in [6] was attributed to the height of the nodes used. The nodes placed at 3 m above the ground had significant blockage through the vegetation, particularly in the urban canyon environment. Investigating how the blockage conditions evolve with the height of nodes and at higher frequencies (sub-THz spectrum) would have been complex, long, and expensive if based on measurements. But using the LiDAR data and the validated ray-based tool, an extension of the initial scenario is easily feasible; it is explored in the present section, including additional heights and node positions.

Three locations with different properties have been considered for the further analysis and channel characterization. The first location considered is the urban canyon environment, which is a street in between two multi-floor buildings with a mixture of glass and metallic frame façade, separated by a distance of 35 m. The length of the street is 150 m-long and consists of some trees and bushes as shown in Fig. 2. The positions of the 5 nodes placed in the area are on average separated by 30 m. In case of the point-to-point scenario, the distance between the links is considered from the first node (marked N1 in Fig. 2) and the other individual nodes. Therefore, the link distances vary with each pair of nodes ranging from 27.8 m to 118 m.

The second location considered is a narrow residential street with thick vegetation, dif-

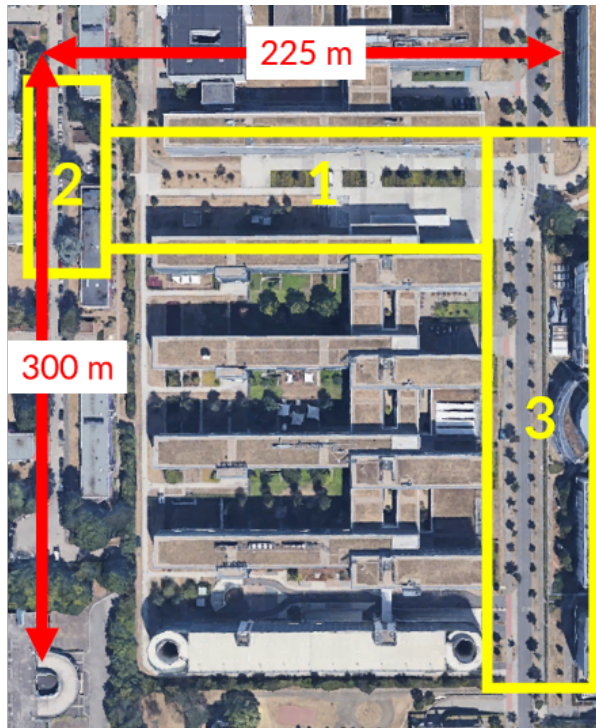


Figure 2: Considered area including all three scenarios.

ferent types of trees, and different heights, as shown in Fig. 3. Apartment buildings with three floors are located on both sides of the street consisting of a complex façade with large windows, concrete walls and balconies. Other in-street objects like sign posts and street lights are also present at regular intervals in the area. The positions of nodes are considered along a sidewalk located 7 m from the closest building wall. A total of 8 different node positions have been considered in this environment at an average distance of 10 m from each other. For the P2P case, the node N1 is considered as the Tx and the remaining nodes as receivers, therefore consisting of varying link distances, similar to the previous location.

The third location is along a wide urban main street with two-lanes for traffic with vegetation lined on both sides of the road as shown in Fig. 3(c). There are also pedestrian paths on both sides of the road. The street is approximately 45 m wide, almost twice as wide as the first location in the urban canyon. The street is about 300 m long and the nodes are placed 29.3 m apart on average on the existing street light positions (found from the LiDAR data).

2.2.2 Ray-based sub-THz channel model and parameters

The Volcano ray-based tool [8] creates multi-paths caused by various channel phenomena like reflection and diffraction on building façades and ground. In-street objects like vegetation or urban furniture generates blockage or attenuation, and above-clutter diffraction. When available, the LiDAR point cloud data is used to detect the in-street obstructions (intersection between the point cloud and the clear ray trajectory) and calculate an accurate penetration length in case of a through-foliage transmission. The tool has been adjusted and validated with various measurements at different mmWave frequencies over the years in different scenarios. Since measurements are mostly only available for frequencies upto 100 GHz,

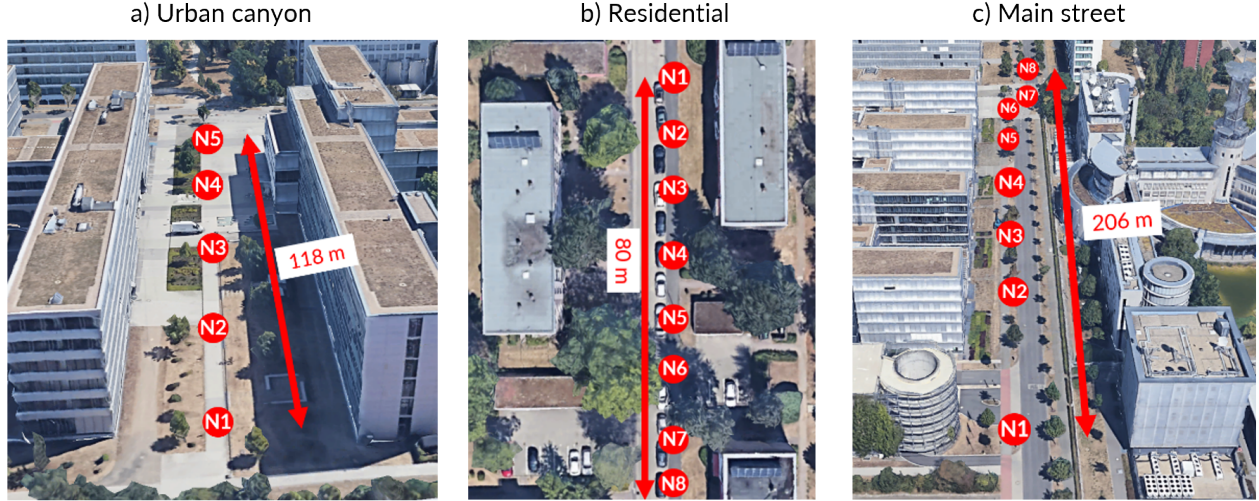


Figure 3: Scenarios in (a) urban canyon, (b) residential, and (c) main street environments.

an extension of the channel model in the sub-THz has been proposed in [9] based on some assumptions (materials, vegetation loss), which is convenient for preliminary investigations.

A vegetation linear loss of 5 dB/m was tuned from cross-analysis of the measurements and simulated paths in the previous 60-GHz validation study [6]. This value has been extrapolated to 12 dB/m at 150 GHz, following the same tendency (but not same absolute values) as in the ITU recommendations [11].

We have supposed clear weather condition, i.e. no rainfall attenuation, as the time availability will be investigated in a later step. Finally, note there is no car blockage or scattering considered in the present study, where the minimum height of nodes is 3 m.

Three deployment scenarios have been evaluated in each environment: 1) Mesh backhaul, being formed of dense pole-to-pole line-of-sight (LoS) links, as studied in the measurements; 2) FWA with access points positioned on poles and user devices a.k.a. CPE installed on the building façades; and 3) Mobile access with same FWA access points but user devices distributed in the outdoor environment at ground level. A link budget summary for all the scenario parameters is presented in Fig. 4, where a 1 GHz signal bandwidth and the polar demodulation described in [4], section 4, are assumed. Different kinds of prediction modes have been performed to match each scenario's specificity: point-to-point (P2P), point-to-façade (P2F), or area coverage, as available in the tool.

The in-street blockage differs significantly from one deployment scenario to the other, but also from one environment to the next. The vegetation in the urban canyon environment is smaller and sparsely spaced whereas the residential area is densely covered with vegetation of different types of trees with varying heights and foliage cross-sectional width. In the main street environment, the vegetation is mostly uniformly distributed along the road with similar heights and types of trees. This environmental diversity was considered on purpose. And section 2.2.4 is gathering the results from the three different environments to get average and fair statistics.

2.2.3 Channel characterization in the urban canyon case

The network of nodes in different environments described in Section 2.2.2 and the ray-tracing tool described in Section 2.2.3 have been used together to analyze both the 60-GHz and 150-

Parameter	Backhaul	FWA	Mobile Access		
Node/AP height	3, 6, 9, 12 m				
CPE/UE height	N/A	3 m	1.5 m		
Bandwidth	1 GHz				
Carrier	60, 150 GHz	150 GHz			
Tx power	0.1, 1 W	0.1 W			
Tx antenna gain	25 dBi				
Sensibility at the Rx input	-73.2 dBm				
Rx antenna gain	25 dBi	15 dBi			
Sensibility at the Rx antenna input	-98.2 dBm	-88.2 dBm			
Add. loss	3 dB				
Weather	Clear				

Figure 4: Scenario parameters.

GHz outdoor backhaul channels, as well as the sub-THz FWA and mobile access propagation ranges.

The differences in the received powers and number of significant paths when increasing the height of the nodes from 3m to 6m for 150 GHz point-to-point links in the urban canyon environment is shown in Fig. 5 and 6. At the mmWave and sub-THz frequencies, the blockage and vegetation linear losses have a significant impact on the propagation environment. The variations in the received power based on the cross-sectional width of the vegetation through which propagation occurs can be significantly different. Some trees are widest (having most foliage) towards the lower parts of the foliage and narrower as the height increases. Due to this, the propagation through the vegetation can have significantly different losses depending on the height. If the considered height is higher than the locally available vegetation or below the foliage, the losses are minimized. A reduction in the linear losses can also be expected in the winter season when the vegetation has lost its leaves.

In Fig. 5, the nodes are located at a height of 3m and even though the vegetation mostly consists of small trees and bushes in this urban canyon environment, there is a significant reduction in the received power components from all the paths apart from the direct LoS path. Although the reflection loss at higher frequencies does not significantly change, the blockage caused due to the vegetation and other in-street objects deteriorates the propagation, making it sparse. Considering only a single height (at which there is maximum blockage), conclusions like a highly sparse channel could be made. However, depending on the local environment and blockage conditions, the tradeoff between the ideal node height providing better connectivity and practical deployment issues must be considered. In particular, the presence of multiple significant paths may be an advantage for spatial multiplexing, or resilience in the face of interferences. Ray-based tools like [8] provide the possibility to analyze and evaluate the channel conditions for a given environment with limited effort, and automatically decide best options.

The number of paths significantly increase with the height of the node as illustrated in Fig. 5-6. While the propagation may be concluded to be highly sparse at height 3 m, due to the vegetation blockage, the same environment can be observed as a canyoning situation with a few strong reflections at a different height.

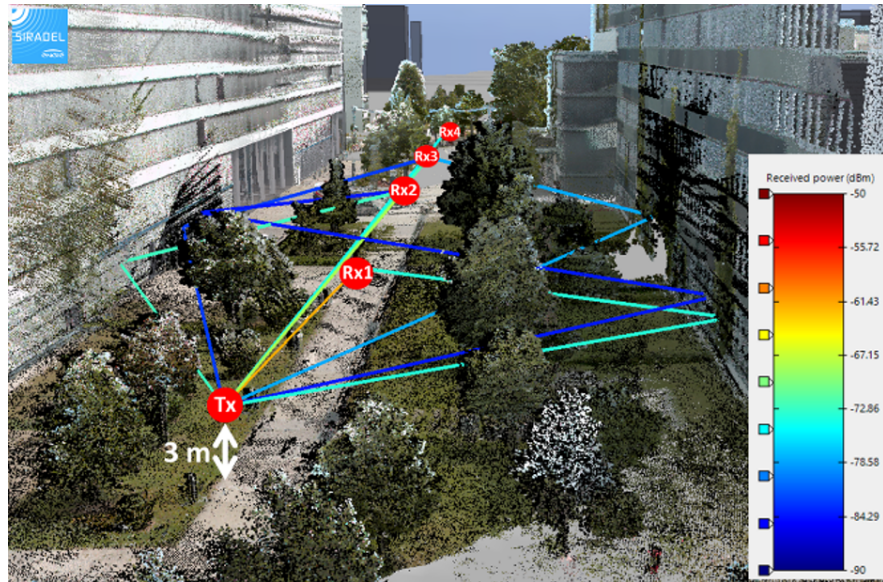


Figure 5: Significant simulated paths for the urban canyon P2P links at height 3 m.

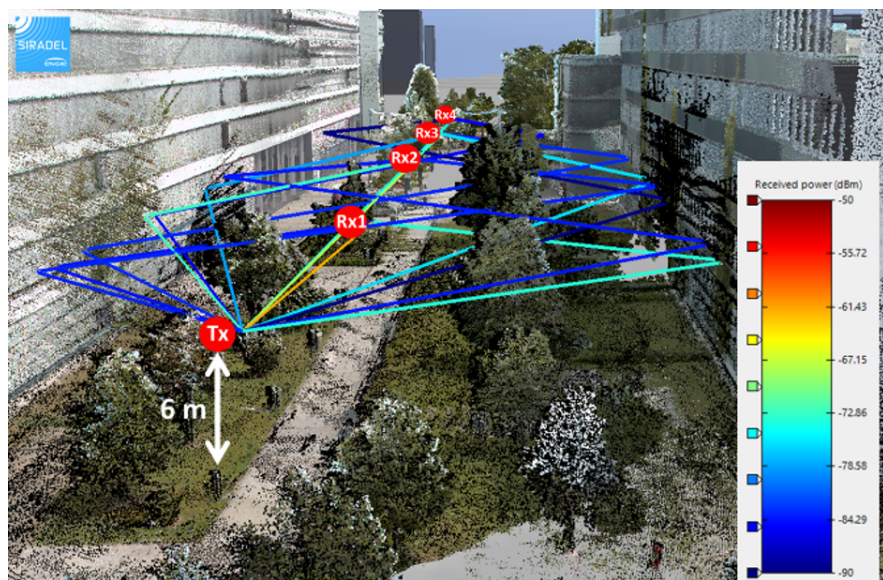


Figure 6: Significant simulated paths for the urban canyon P2P links at height 6 m.

2.2.4 Point-to-point backhaul links

All the 20 nodes described in Section 2.2.2. have been utilized to obtain three different results based on backhaul, fixed access and mobile access links. P2P, P2F and coverage maps have been respectively used to compare the performance of different node heights. To calculate the number of significant paths for each link, a receiver sensitivity of -98.2 dBm is considered, which corresponds to a spectral efficiency 0.6 bps/Hz.

The ideal height of the nodes can vary from one scenario to another and even from one node to another depending on the immediate obstacles around the nodes. Due to the higher path losses, the importance of significant propagation paths which have the strongest power after the direct LoS path like reflections increases. Not just to provide a connection if the direct-path is blocked but also to provide spatial diversity of reception. If these paths are significantly attenuated, it has a major impact on the propagation channel.

Different link lengths are considered by using the first node (N1 in Fig. 3) in each environment as a transmitter and the other nodes as receivers (N2-N5 in Fig. 3). The total number of nodes considered are 20 and the number of links are 3, 7 and 7 respectively for the urban canyon, residential and main street scenarios with a total of 17 P2P links. Transmit powers corresponding to 0.1 W (20 dBm) and 1 W (30 dBm) are plotted. The average of the total number of significant paths for each link is plotted against the height of the nodes in Fig. 6. As the transmit power is increased, more paths through the same vegetation become visible at the receiver. In the main street (Fig. 3(c)), the nodes are located on existing light poles and between each light pole there exists a tree. At a height of 6m, the vegetation losses are the highest due to the largest vegetation cross-section along the direct LoS path. This results in an average of just 1.3 and 1.4 significant paths at this height for respectively 20 dBm and 30 dBm transmit powers. Finally, Fig. 7 shows significantly better channel diversity statistics at the lowest (3 m) and highest heights (9 m and above). The plot also indicates that the multi-path diversity reduces by 0.3 in average for same link budget at 60 and 150 GHz, with a maximum of 0.7 at height 6 m.

2.2.5 Mobile access coverage

A coverage (or received power) map is computed around each node, as illustrated in Fig. 8, for an outdoor mobile device at 1.5 m above ground. Fig. 9 shows the average of the single-node covered surfaces for a varying received power threshold and for different node heights. The covered areas obtained from the link budget given in Fig. 4 is highlighted by the vertical dotted line.

At the highest received power thresholds, the coverage is due to the direct LoS path in the immediate vicinity of the node. As the distance increases, corresponding to a larger covered area, the probability of blockage is greater. By consequence, the rate of additional coverage surface due to every 1 dB sensibility gain degrades very rapidly. The best coverage is always obtained from the nodes at height 3 m whatever the receiver sensibility is, first because those nodes are closer to the user equipment's at 1.5 m, but also due to the favorable propagation met below the foliage. The coverage may locally be improved by using a node height of 12 m, as highlighted by the red circles in Fig. 7; this occurs when the obstructing foliage is low; nevertheless, if considering a receiver threshold of -88.2 dBm (link budget given in Fig. 4), the coverage at 12 m is globally 7% lower than the coverage at 3 m. Those results

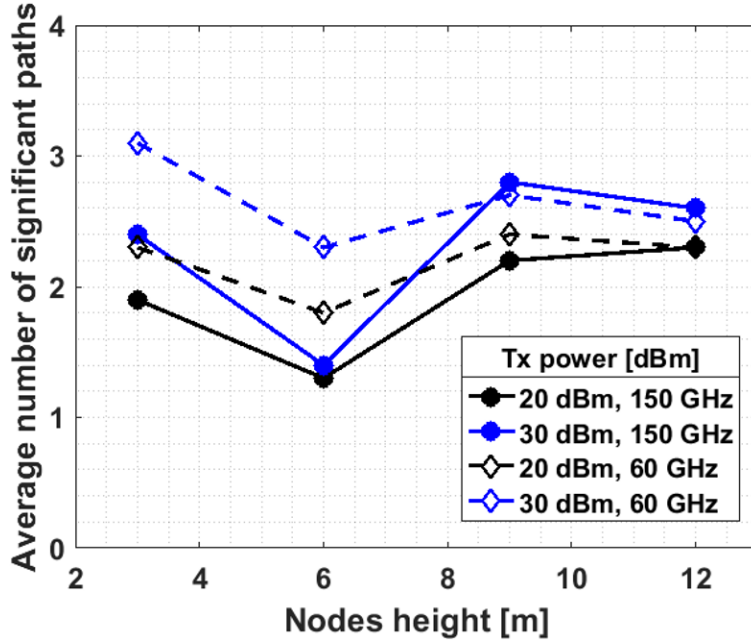


Figure 7: Average number of significant paths per P2P LoS link.

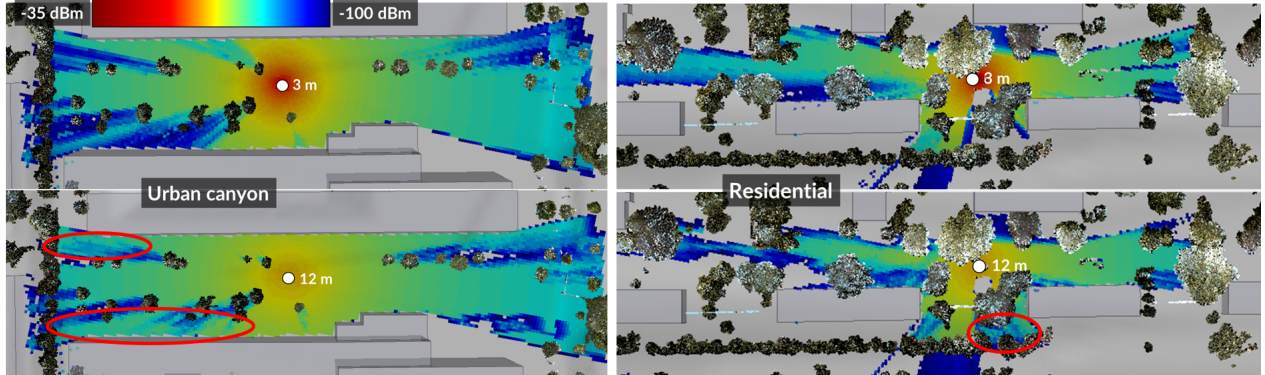


Figure 8: Rx power map around two different nodes.

demonstrate the significant impact of vegetation at higher frequencies. It also stresses the sensitivity of the propagation simulations to accurate representation of the environment; we believe a realistic sub-THz channel model needs to integrate some geographical data and some physics into it.

2.2.6 Fixed Wireless Access (FWA) coverage

Another promising outdoor application of the sub-THz frequencies apart from the point-to-point back-haul links is Fixed Wireless Access (FWA). The same 20 node positions have been utilized and the coverage is evaluated as obtained at 3 m above ground along the building facades. Fig. 10 shows the average of the covered "façade" length for each single-node and for a varying received power threshold considering different node heights. The coverage at the highest received power thresholds is found to be better for lowest node heights (maximum 9 m) due to reduced blockage probability and smallest vegetation transmission lengths in the node vicinity. High node elevation is not an advantage, because most CPE's are located

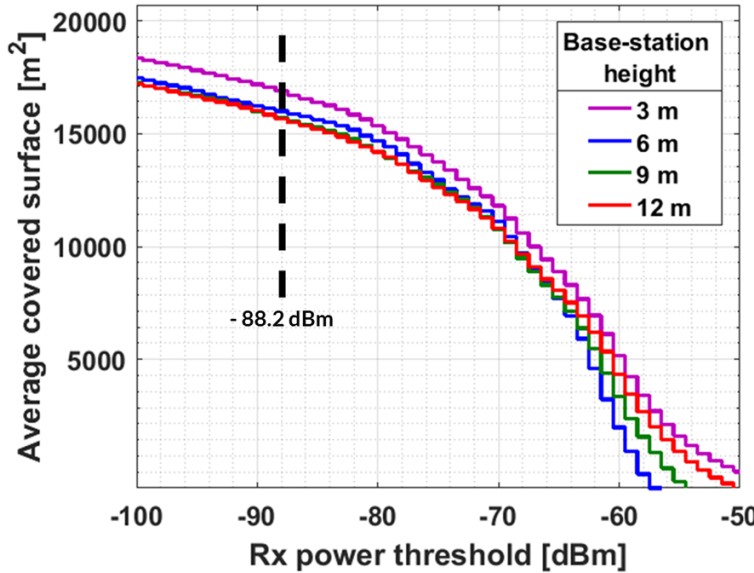


Figure 9: Average covered area per node for different heights.

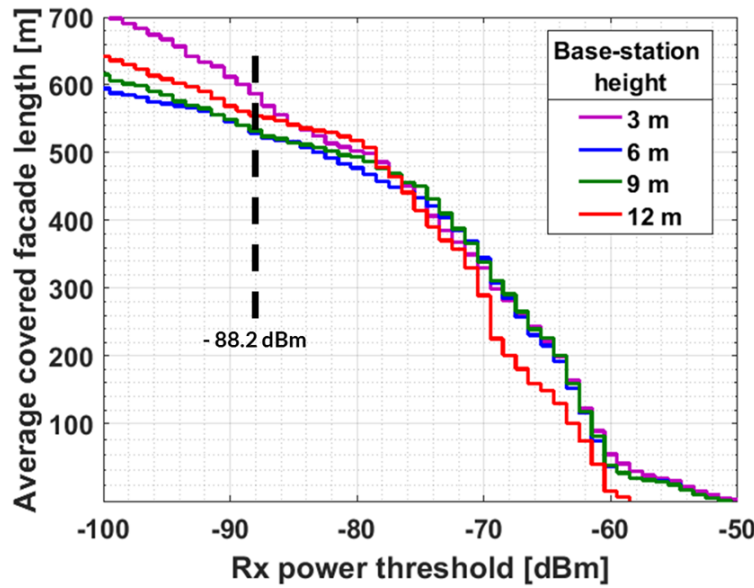


Figure 10: Average covered facade length per node for different heights.

behind trees and below foliage. At lower received power thresholds, the nodes at 12 m still suffer from a more severe attenuation at the CPE's located behind a row of trees, but do benefit from a better propagation above trees in some directions. Finally, the intermediate heights appear as slightly less advantageous.

2.3 Scattering by the vegetation

The Volcano ray-tracing model has also been extended in order to predict diffuse scattering in addition to the two previously existing interactions due to foliage i.e. top diffraction and transmission. Actually, the foliage volume is divided into small voxels. And when a voxel is

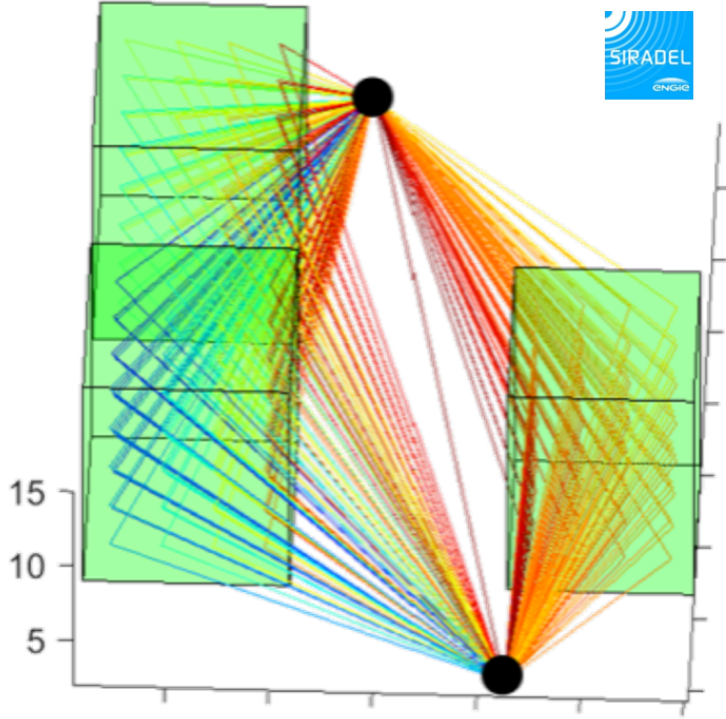


Figure 11: Propagation paths diffused by the vegetation.

[width=0.6]./prop/Diffuse scattering simulation.png

Figure 12: Simulated path contributions due to the vegetation diffusion.

visible (no building obstruction) from together the transmit and receive antennas, a scattered path is constructed that propagates from the transmit position to the foliage's voxel, and then to the receive position. The diffused path gain is derived from the bi-static radar equation [12] along with the scattering pattern given in [13]. The principles are illustrated in Fig. 11.

SIRADEL had recently the opportunity to validate and calibrate this model from measurements at 28 GHz in a highly-vegetated scenario. However we are not able to validate the scaling from 28 to 150 GHz (the simulated frequency here), we have used the same calibrated model in order to observe how the foliage scattering could affect the subTHz propagation channel.

The foliage scattering has been computed in the residential scenario, for the LoS link between the transmit antenna and the receive position referred as N3 in Fig. 3. Three trees are creating significant diffused components, which are located on both sides of the sidewalk, marked as trees "1", "2" and "3" in Fig. 12. The resulting diffused field is reaching a maximum of -27 dB (relative to the LoS direct-path), and contributes to the delay and angular spreading of the channel as shown by the Power delay profile and Power angular profile in Fig. 12. The foliage scattering is likely not a dominant or strong component in the sub-THz channel, but it leads to some delay and angular diversity that may not be negligible when the LoS path is obstructed. However this has not been modeled yet, the wind and foliage diffusion surely introduces some time-variant fading and Doppler into the propagation channel.

2.4 Conclusions

As the need for larger bandwidths and capacity drives beyond-5G applications towards the promising spectrum available in sub-THz bands, better understanding of the channel, characterization, validation and evaluation of such high frequency channels is required. Due to physical constraints in measurement campaigns, it is often very difficult to obtain a holistic perspective of a channel, especially new spectrum that has not yet been explored significantly. The validated tools can then be exploited to explore other scenarios utilizing the same physics phenomenon like analyzing the height of the nodes to better understand the channels.

In this section, tools validated with measurements at 28 and 60 GHz have been used to analyze propagation channels at 150 GHz. Both backhaul and access links have been considered at 4 different heights. Various scenarios like urban canyon, residential and main street have been considered with different link distances and situations; the channel does not necessarily benefit from better conditions at higher node heights (as usually observed at lower frequencies). It can behave significantly different depending on the height of the nodes, power and angular sensitivity of the receiver and the considered transmit power. Vegetation is a significant cause for the in-street blockages at higher frequencies and accurate representations using for instance LiDAR data must be considered for physical-layer evaluations. However this must be validated later by measurements, it shown the foliage can be a source of diffuse propagation paths possibly significant for short-range NLoS links.



3 RF impairments Modelling

3.1 Introduction

To reach 100+ Gbit/s data rates, classical coherent architectures are combined with high spectral efficiency schemes. This entails numerous constraints on the design of radio-frequency components especially at the oscillator level. Indeed, high frequency oscillators severely impair sub-THz systems with Phase Noise (PN) [14]. It is hence essential to discuss the PN model selection to design dedicated signal processing and thus performant schemes.

A wide range of PN models have been introduced in the literature: Non-linear [15], Tikhonov [16], Wiener [17], ... The selection of the PN model is application dependent. For millimeter-wave systems, the PN is usually modeled by the superposition of a correlated contribution (colored PN) and an uncorrelated one (white PN floor) [18]. However, sub-THz systems exploit wider bands and thus require to reconsider the PN model. It has been shown in [17] that performance of wide-band systems are significantly more impacted by the uncorrelated contribution of PN than the correlated one. This result prompts us to compare the efficiency of an uncorrelated Gaussian PN model to the common correlated one used for millimeter-wave, superposition of Wiener PN and Gaussian PN.

In this work, we intend to provide analytical tools for sub-THz communication design and circuit specifications. Firstly, we present two PN models: one correlated (Wiener PN + Gaussian PN) and another uncorrelated (Gaussian PN). Secondly, these two models are confronted by means of numerical simulations as well as an analytical analysis. The accuracy of the uncorrelated Gaussian PN model is first checked with a Pearson's χ^2 goodness of fit test. We next derive the closed-form expression of the likelihood-ratio of the two models. Thereupon, an analytical condition is proposed to determine whether the correlated or the uncorrelated model is the most efficient given a system bandwidth and an oscillator spectral characterization. Numerical simulations are performed with realistic PN generated according to a state-of-the-art sub-THz oscillator. Simulation results show that an uncorrelated Gaussian process is appropriate to model the impact of PN in sub-THz systems. Thirdly, the proposed results on model selection are applied to link adaptation in the presence of PN. Upon the analysis of the Bit-Error-Rate (BER) of phase modulated signals, we are able to choose the most robust scheme between a coherent and a differential modulation.

3.2 System Description

3.2.1 Oscillator

The modeling of the complex output v of a practical oscillator with central frequency f_0 is given by

$$v(t) = \left(1 + \varepsilon(t)\right) \exp\left(j2\pi(f_0 + \zeta)t + j\phi(t)\right), \quad (1)$$

where ε , ζ and ϕ denote respectively the amplitude noise, the Carrier Frequency Offset (CFO) and the PN. The amplitude noise ε is mitigated by applying a limiter on the oscillator output and is considered negligible [19]. It is also assumed that the receiver is synchronized in frequency s.t. the CFO term ζ is compensated. When it comes to PN, the common figure to characterize the performance of an oscillator is its Single-Side-Band (SSB) spectrum $\mathcal{L}(f)$.

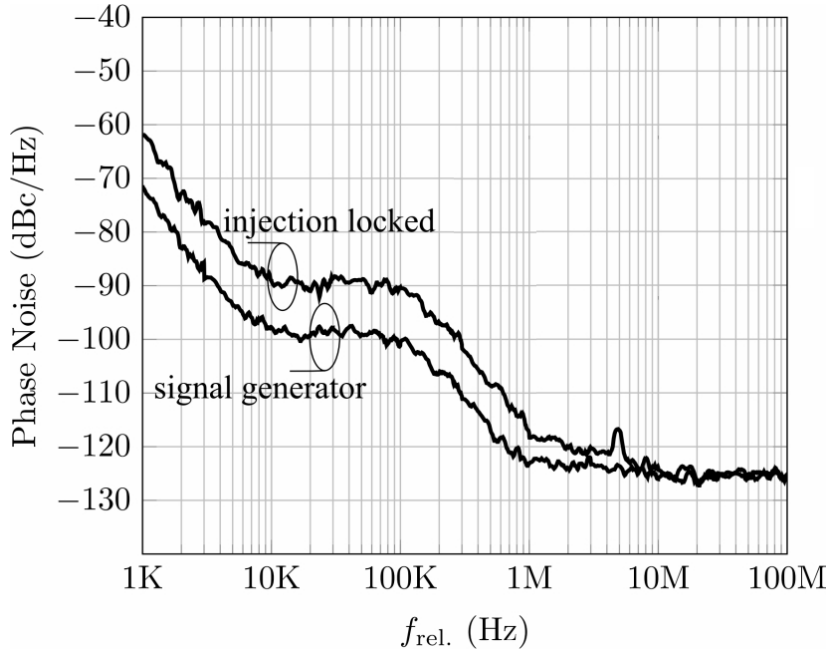


Figure 13: PSD of the considered 200 GHz oscillator [1].

It is obtained throughout the following measurements

$$\mathcal{L}(f) = \frac{S_v(f_0 + f)}{P_v}, \quad (2)$$

with S_v the Power Spectral Density (PSD) and P_v the power of the oscillator output v . Though the total power of an oscillator should ideally be concentrated in f_0 and the PSD of the oscillator a pure tone, PN induces the power to be spread over frequencies around f_0 . We denote S_ϕ the PSD of PN ϕ . For large f , the small angle approximation $e^{j\phi} \simeq 1 + j\phi$ leads to $S_\phi(f) \simeq \mathcal{L}(f)$. The latter equation bonds the PN ϕ and the oscillator output v . This link enables us to calibrate the PN model on the oscillator spectral characterizations. In this work, we intend to confront PN models on realistic observations. We therefore select a state-of-the-art 200 GHz oscillator [1], whose PSD is illustrated in Fig. 13. The simulated PN will correspond to this oscillator by respecting the spectral characteristics measured in Fig. 13. We refer the reader to [17] for PN simulation based on oscillator spectral characterizations and also to [20] for simulation of power law noise.

3.2.2 Channel

The recent measurement campaigns [21] have confirmed the expectations from theory that the line-of-sight component prevails in sub-THz channels, hence considered as frequency flat. We study a single carrier communication system¹ impacted by oscillator PN. It is assumed that the channel is ideally equalized² and the receiver synchronized in time and frequency. Subsequently, we consider the discrete-time symbol model of an Additive White Gaussian

¹Though the presented results may also be exploited for channel bonding or multi-carrier modulation schemes.

²The phase shift of the channel is compensated and the propagation gain is normalized.

Noise (AWGN) channel impacted by PN. The received symbol at instant k is expressed by

$$r_k = s_k e^{j\phi_k} + w_k, \quad (3)$$

where s_k is the modulated symbol with duration T and $w_k \sim \mathcal{CN}(0, \sigma_w^2 = N_0/T)$. The spectral density of the white noise is denoted N_0 . The discrete stochastic process ϕ_k represents the oscillator PN to be modeled. Further, the discrete-time symbol model in Eq. (3) is discussed in [22]. Conditions on the PN intensity and the sampling rate of the system are given for this model to be accurate. It is also worth mentioning that communication systems may use separate oscillators at the transmitter and the receiver. In this case, both PN contributions must be added together.

3.3 Phase Noise Models

We present in this section two PN models. The first one is a correlated model based on the physical modeling of the PN generation in oscillators. This model is frequently used for millimeter-wave systems [18] and describes the superposition of a correlated contribution (colored PN) and an uncorrelated one (white PN floor). The second one is an uncorrelated model describing only the white PN floor. Its mathematical expression is hence simple and commonly exploited to optimize the signal processing for PN channels [23].

3.3.1 Correlated phase noise

PN generation in oscillators is due to the transformation of amplitude fluctuations into phase fluctuations. In practical systems, free-running oscillators are stabilized by means of a Phase-Locked Loop (PLL). With respect to the linear time-invariant model of the PLL, the PN generation mechanism may be modeled as an amplification and an integration of the noise sources present in the circuits [17] [19]. The integration of noise sources by the PLL gives a cumulative and correlated nature to PN. We make the assumption that the circuitry is only subject to white noise³. Accordingly, the oscillator PN ϕ_k may be modeled by the superposition of a Wiener (Gaussian random-walk) process $\phi_{w,k}$ and a Gaussian one $\phi_{g,k}$ [19] *i.e.*

$$\phi_k = \phi_{w,k} + \phi_{g,k}. \quad (4)$$

The Gaussian PN $\phi_{g,k} \sim \mathcal{N}(0, \sigma_g^2)$ is caused by the amplification of the thermal noise in the oscillator. The Wiener PN is defined by

$$\phi_{w,k} = \phi_{w,k-1} + \delta\phi_{w,k}, \quad (5)$$

where $\delta\phi_{w,k} \sim \mathcal{N}(0, \sigma_w^2)$. It expresses the integration by the PLL and hence the cumulative nature of PN. Fig. 14 presents the PSD described by this PN composed of two characteristics. The uncorrelated Gaussian process with variance $\sigma_g^2 = K_0/T$ has a flat spectrum of density K_0 . The correlated Wiener PN presents a Lorentzian characteristic (*i.e.* $1/f^2$) [19] with density K_2 . The variance of the Wiener increment verifies $\sigma_w^2 = 4\pi^2 K_2 T$ [19]. The variances σ_g^2 and σ_w^2 of the two processes are bonded by the corner frequency $f_c^2 = K_2/K_0$. We use hereafter the normalized corner frequency $f_c \cdot T$ expressed as a fraction of the band. In the

³The influence of flicker noise is disregarded in this work.

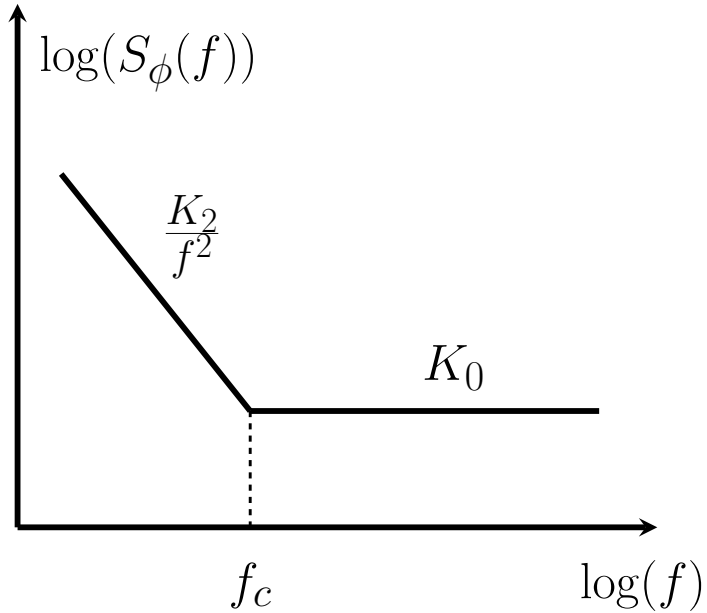


Figure 14: PSD of the considered correlated PN model.

following, we will refer to this model as M_W for short. Based on the physical modeling of the PN generation in oscillators, this model is frequently used in the literature for its accuracy – see [17] and references therein. However its complexity motivates the introduction of an uncorrelated Gaussian PN model.

3.3.2 Uncorrelated phase noise

By definition, modeling a stochastic process represents a trade-off between the accuracy and the complexity of description. Since the development of communication systems highly benefits from analytical analyses, the low analytical complexity of a model can be preferred over its accuracy. By means of illustration, the Gaussian PN model has already been exploited in [23] to optimize constellations for PN channels and also in [24] to improve demodulation in the presence of PN. We thus turn away from the accurate but complex M_W to consider the Gaussian PN model. Besides its mathematical convenience, the Gaussian distribution is also a relevant PN model for wide-band systems. The work in [17] has studied separately the influences of the different PN spectrum regions on communications. It has exhibited a strong dependence with the system bandwidth $1/T$. In particular, when considering high symbol rate systems, the oscillator noise floor – characteristic K_0 in Fig. 14 – represents the greatest contribution to the overall PN. This result may also be appreciated by evaluating the ratio

$$\gamma = \frac{\sigma_w^2}{\sigma_g^2} = 4\pi^2 f_c^2 T^2. \quad (6)$$

For wide-band systems, $f_c \ll 1/T$ leads to $\sigma_w^2 \ll \sigma_g^2$. It follows that the Wiener PN becomes negligible compared to the Gaussian PN. For these reasons, it is worth considering a Gaussian PN model denoted M_G . The oscillator PN ϕ_k is described by a truncated Gaussian distribution,

$$\phi_k \sim \mathcal{N}(0, \sigma_g^2). \quad (7)$$

Table 1: Spectral density K_0 (dBc/Hz) of the white PN floor.

		Bandwidth $1/T$		
		100 MHz	1 GHz	10 GHz
Strong PN	$\sigma_g^2 = 10^{-1}$	-90	-100	-110
Medium PN	$\sigma_g^2 = 10^{-2}$	-100	-110	-120
Low PN	$\sigma_g^2 = 10^{-3}$	-110	-120	-130

As the phase is naturally bounded by $[-\pi, \pi]$, the Gaussian distribution must be truncated. The probability density function is normalized⁴ by $\lambda = (F_N(\pi) - F_N(-\pi))^{-1}$ to ensure that $\int_{-\pi}^{\pi} p(\phi)d\phi = 1$, where F denotes the cumulative distribution function. Returning to oscillator characterization, Table 1 presents some values of spectral density K_0 of the white PN floor for different variances σ_g^2 and system bandwidth $1/T$. The following work evaluates the efficiency of M_G to model PN observations. It is clear from Eq. (6) that the accuracy of M_G is function of the normalized corner frequency $f_c \cdot T$.

3.4 Model Selection

We have previously introduced two PN models: M_W correlated with a complex and accurate description of PN, and M_G uncorrelated with a simple mathematical expression. In this section, we first evaluate the accuracy of M_G , the Gaussian distribution, to model PN observations. Then, we compare the likelihood of the correlated M_W and uncorrelated M_G models in order to select the most efficient one given the system bandwidth and the oscillator spectral characterization.

3.4.1 Accuracy of the Gaussian model

To assess the accuracy of M_G , we perform a Pearson's χ^2 goodness of fit test on simulated PN. By doing so, we intend to determine the systems parameters, communication bandwidth and oscillator spectral characteristics, for which M_G models accurately the PN observations. The simulated PN samples are generated either according to M_W , considered as an accurate and realistic PN model, or to the oscillator described in Fig. 13. First, the goodness of fit test is described, and then, the simulations results are presented.

Pearson's χ^2 goodness of fit test

The aim of this subsection is to establish whether an observed PN frequency distribution differs from a truncated Gaussian distribution. In other words, we operate normality tests on simulated PN. Let $\phi = \{\phi_k\}_{1 \leq k \leq N}$ denote the observed values of random PN and N the number of symbols within a communication frame. Two different communication frames hence represent two independent realizations of PN. The null hypothesis can now be described

⁴It is worth mentioning that most of algorithms are not subject to a normalization of the likelihood function and hence a factor multiplication does not increase the complexity.

as

$$H_0 : M_G \text{ is consistent with the observations } \phi. \quad (8)$$

To test this hypothesis, a *Neyman-Pearson approach* is a reasonable choice. This approach is designed for binary detection problem with a given significance α [25]. The hypothesis testing δ takes the following form

$$\delta(\phi) = \begin{cases} \text{accept } H_0, & \text{if } S(\phi) < \lambda_c, \\ \text{reject } H_0, & \text{otherwise,} \end{cases} \quad (9)$$

where S is the test statistic of observed samples ϕ compared to a decision threshold λ_c which maximizes the probability of detection. Further, we exploit the common Pearson's χ^2 goodness of fit to test the observations against the null hypothesis H_0 . In this case, the value of the statistic S is

$$S(\phi) = N \sum_{i=1}^M \frac{\left(\frac{O_i(\phi)}{N} - p_i \right)^2}{p_i}, \quad (10)$$

where O_i is the number of observations $\phi_k \in I_i$, while M denotes the number of intervals I_i partitioning $(-\pi, \pi]$ and $p_i = Pr(\phi_k \in I_i)$. To determine the goodness of fit we compare the value of $S(\phi)$ to a χ^2_{M-2} distribution with $M - 2$ degrees of freedom⁵. The critical value is given by $\lambda_c = F^{-1}_{\chi^2_{M-2}}(1 - \alpha)$, where α is the given significance.

Simulations results

We first perform the χ^2 test on PN samples generated according to M_W , with significance $\alpha = 0.1$. Fig. 15 illustrates the frequency of accepting H_0 as a function of the normalized corner frequency $f_c \cdot T$. This confirms the aforementioned intuition in Eq. (6) that M_G is accurate when $f_c \ll 1/T$. The value 0.9 of the frequency of accepting is consistent with the significance of 0.1. It must be pointed out that N , the length of the studied sequence, has a great influence on the selection of the model. For long sequences, the impact of the PN correlation is significant and cannot be neglected. Secondly, we test H_0 against realistic PN samples simulated according to the oscillator described in Fig. 13. The frequency of choosing $\delta(\phi) = H_0$ is presented in Fig. 16 as a function of the system bandwidth $1/T$. Properties observed in Fig. 16 and the resulting conclusions are similar to the ones of Fig. 15. We have confirmed with the Pearson's χ^2 goodness of fit test that the uncorrelated Gaussian PN model M_G is accurate if the corner frequency remains small compared to the system bandwidth. However, we have not yet derived an analytical expression of the dependence between the accuracy of M_G and the system features N and $f_c \cdot T$. This is carried out in the following subsection.

3.4.2 Models comparison

We have previously witnessed the limitations of the Neyman-Pearson approach. The properties of M_G have been highlighted, still they have not been expressed analytically. To do so, we compare the efficiency of M_W and M_G to model some PN observations $\phi = \{\phi_k\}_{1 \leq k \leq N}$.

⁵The variance is estimated from observations, the mean is not.

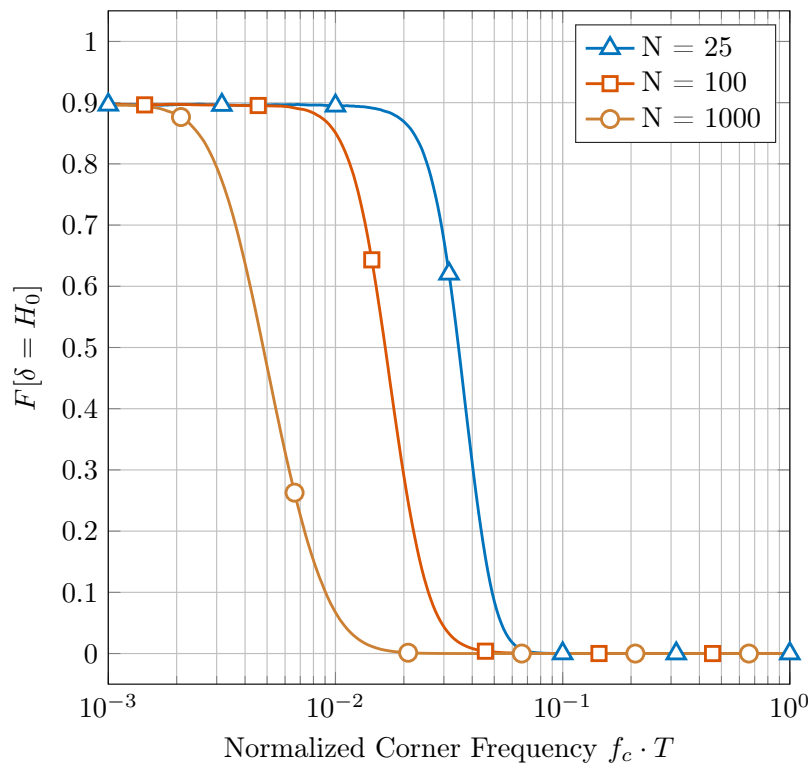


Figure 15: Frequency of accepting the Gaussian model H_0 with a χ^2 goodness of fit test for simulated correlated PN.

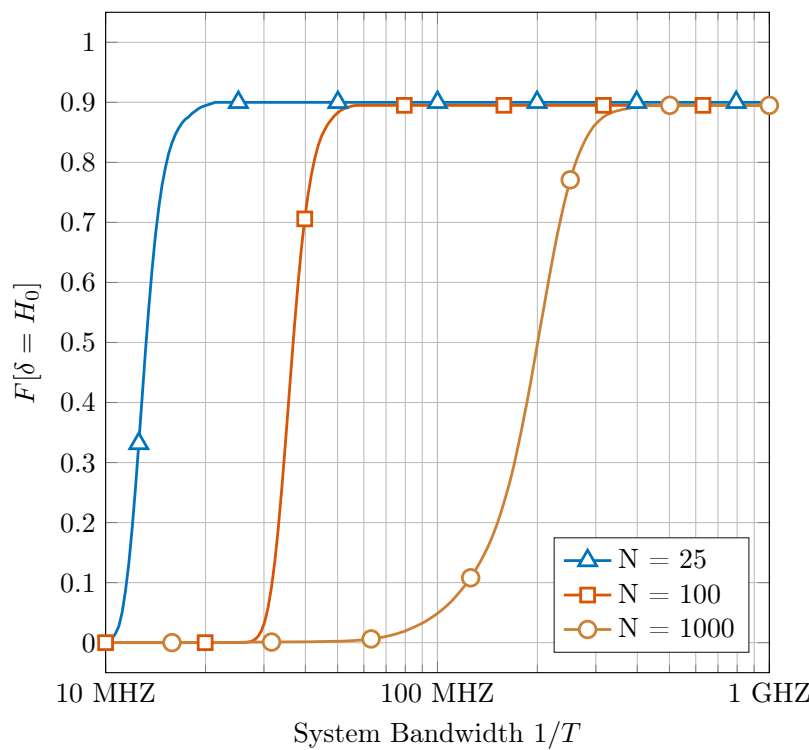


Figure 16: Frequency of accepting the Gaussian model H_0 with a χ^2 goodness of fit test for simulated realistic PN.

We recall that N denotes the number of symbols within a frame and that different frames represent independent realizations of PN.

Log-likelihood ratio

Given the oscillator PSD, the comparison between M_G and M_W can be achieved by evaluating the Log-Likelihood Ratio (LLR) of the models for observations ϕ , *i.e.*

$$\Lambda_{G/W} = \ln \left(\frac{P(\phi|M_G)}{P(\phi|M_W)} \right), \quad (11)$$

denoted Λ for brevity. While the sign of Λ infers the model to select (M_G if $\Lambda \geq 0$, M_W otherwise), its absolute value quantifies the reliability of this decision. So, $|\Lambda|$ small leads to the conclusion that M_G and M_W are equally likely. Conversely, a high value of $|\Lambda|$ indicates that the observations are particularly in favor of one model over the other. To derive the expression of Λ , we must express the joint distributions $p(\phi|M_G)$ and $p(\phi|M_W)$. Regarding M_G , ϕ_k are i.i.d.. It is hence straightforward from Eq. (7) that

$$p(\phi|M_G) = (2\pi\sigma_g^2)^{-\frac{N}{2}} \cdot \exp \left(-\sum_{k=1}^N \frac{\phi_k^2}{2\sigma_g^2} \right). \quad (12)$$

As for M_W , PN is correlated and we must start by applying the conditional chain rule. Denoting $\phi_{k-1} = (\phi_1, \dots, \phi_{k-1})$,

$$p(\phi|M_W) = \prod_{k=1}^N p(\phi_k|M_W, \phi_{k-1}) = \prod_{k=1}^N p(\phi_k|M_W, \phi_{k-1}). \quad (13)$$

The latter equality holds as M_W is a Markov chain of order 1. To evaluate the factors in the previous equation, we next define $\Delta\phi_k = \phi_k - \phi_{k-1}$ which yields

$$\begin{aligned} p(\phi_k|M_W, \phi_{k-1}) &\sim \mathcal{N}(\phi_{k-1}, \sigma_g^2(2 + \gamma)), \\ &= p(\Delta\phi_k|M_W) \sim \mathcal{N}(0, \sigma_g^2(2 + \gamma)), \end{aligned} \quad (14)$$

where $\gamma = \sigma_w^2/\sigma_g^2$ as defined in Eq. (6). Substituting Eq. (14) into (13), we have

$$p(\phi|M_W) = (2\pi\sigma_g^2(2 + \gamma))^{-\frac{N}{2}} \cdot \exp \left(-\sum_{k=1}^N \frac{\Delta\phi_k^2}{2\sigma_g^2(2 + \gamma)} \right). \quad (15)$$

At last, we obtain the closed-form expression of the LLR:

$$\Lambda = \frac{N}{2} \ln(2 + \gamma) + \sum_{k=1}^N \frac{\Delta\phi_k^2}{2\sigma_g^2(2 + \gamma)} - \sum_{k=1}^N \frac{\phi_k^2}{2\sigma_g^2}, \quad (16)$$

which completes our derivation.

Simulation results with correlated phase noise

Let us now consider that the PN observations are generated by a M_W process and study the

expected value $E[\Lambda]$. Given the system features N and $f_c \cdot T$, the expected value of the LLR yields the selected model in average. Since M_W is considered as an accurate and realistic PN model, studying the expected value of the LLR enables us to characterize analytically the observed properties in Fig. 15 and 16. When ϕ_k are generated according to M_W , we have in Eq. (16)

$$\sum_{k=1}^N \frac{\Delta\phi_k^2}{\sigma_g^2(2+\gamma)} \sim \chi_N^2, \quad \text{with } E[\chi_N^2] = N. \quad (17)$$

Then, the second sum in Eq. (16) has for expected value

$$\begin{aligned} E\left[\sum_{k=1}^N \phi_k^2\right] &= \sum_{k=1}^N E[(\phi_{w,k} + \phi_{g,k})^2], \\ &= \sum_{k=1}^N E[\phi_{w,k}^2] + E[2\phi_{w,k} \cdot \phi_{g,k}] + E[\phi_{g,k}^2], \\ &= \sigma_g^2 \cdot \sum_{k=1}^N (k \cdot \gamma + 1) = \sigma_g^2 \left(\frac{N(N+1)}{2} \gamma + N \right). \end{aligned} \quad (18)$$

It follows that the expected value of the LLR is given by

$$E[\Lambda] = \frac{N}{2} \left(\ln(2+\gamma) - \gamma \cdot \frac{N+1}{2} \right). \quad (19)$$

Several remarks must be mentioned with regard to this expression. Firstly, $E[\Lambda] \propto -\gamma \cdot N$ confirms the simulation results that the longer the sequence, the lower the normalized corner frequency must be to ensure that M_G remains an accurate model. Furthermore, we are now able to give a condition on N and $f_c \cdot T$ for the correlated PN to be negligible. By evaluating the inequality $E[\Lambda] \geq 0$ with a 1st-order approximation, we claim that the PN is appropriately modeled by M_G if

$$N \cdot f_c^2 \cdot T^2 \leq \frac{\ln(2)}{2\pi^2}. \quad (20)$$

Regarding communication design, the condition in Eq. (20) may either be exploited to specify the normalized corner frequency $f_c \cdot T$ or to set the length N of the frame. Secondly, when the PN is generated from M_W with γ small, the value of Λ may be greater than zero. The LLR actually penalizes the complexity of M_W in comparison to M_G . This illustrates the Occam's razor: if both M_G and M_W accurately model the observations, then the simplest model should be favored. Eventually, Fig. 17 presents the mean LLR value for different frame lengths with M_W simulated PN. Fig. 17 and condition in Eq. (20) may be exploited to select the best PN model – M_G if $E[\Lambda] \geq 0$, M_W otherwise – with regard to system features N and $f_c \cdot T$.

Simulation results with realistic PN

In this paragraph, the simulation results are presented for a realistic PN corresponding to the sub-THz oscillator described in the Fig. 13. The Fig. 18 shows the mean value of the

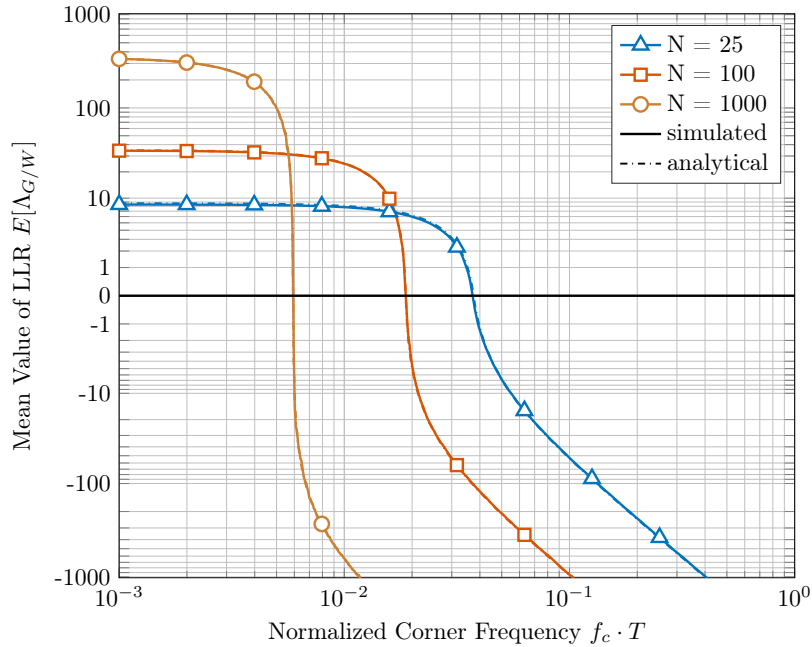


Figure 17: Mean value of LLR $\Lambda_{G/W}$ on simulated correlated PN.

LLR as a function of the system bandwidth $1/T$ for several frame lengths N . The analytical curves correspond to the expected value of the LLR if the PN samples were generated according to M_W with characteristics K_0 and K_2 measured on Fig. 13. We can deduce from these results that the condition given in Eq. (20) does indeed ensure that an uncorrelated PN model is valid. Nevertheless, it can be observed that this analytical condition is slightly conservative in view of the results obtained by simulation. This may be explained by the fact that the correlated PN of the oscillator close to the center frequency is not as strong as the one described by a Lorentzian characteristic. In other words, M_W models a stronger correlated PN contribution than the one measured in practice. Furthermore, considering that the bandwidths of sub-THz systems will be of the order of the GHz [26], we can conclude from these results that an uncorrelated Gaussian model is appropriate to describe the PN in sub-THz communications.

3.5 Application to Link Adaptation

The objective of this section is to give the reader some application examples. In particular, it aims to illustrate that the proposed model selection may be exploited to adapt the modulation with regards to the oscillator PN performance.

3.5.1 BER analysis for PSK and DPSK

High-rate communications over wireless links in the sub-THz domain demand tremendous amount of power. For this reason, constant envelope modulations are valuable since they offer an efficient use of amplifiers. Yet, coherent Phase Shift Keying (PSK) are very sensitive to phase related impairments. Differential PSK (DPSK) has been introduced to enable non-coherent demodulation. It is hence not subject to the cumulative nature of PN. This robustness is achieved at the expense of a noise enhancement – $\simeq 3$ dB – and so a BER

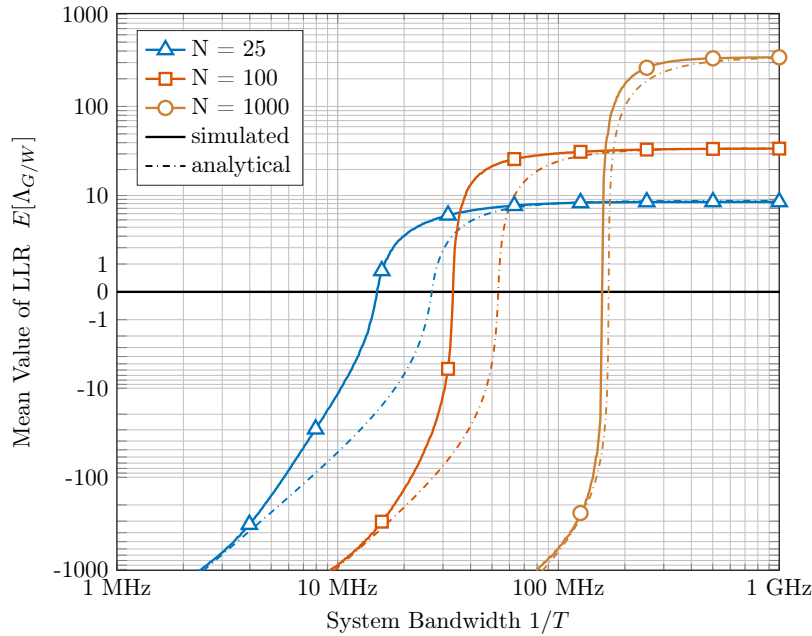


Figure 18: Mean value of LLR $\Lambda_{G/W}$ on simulated realistic PN.

degradation. Still, the stronger the phase impairments, the more interesting it is to select a differential modulation. This leaves an open question: With regard to normalized corner frequency, when does DPSK become more robust than PSK? The closed form expressions of PSK and DPSK BER subject to M_W PN have been derived in [27]. Fig. 19 depicts the BER performance for a 4-PSK and a 4-DPSK with a Signal-to-Noise Ratio (SNR) of 20 dB and a frame length of $N = 7$ symbols. The aforementioned intuition is confirmed: Though the DPSK presents a loss in BER performance, it is more robust than the PSK for strong correlated PN. It may be observed on Fig. 19 that the PSK and DPSK performance are equal in a critical value γ_c independent from the white PN variance. It can also be shown that γ_c is independent from the SNR. For this reason, γ_c provides a general criterion for link adaptation. Moreover, it is worth noting that the plotted BER satisfies the condition in Eq. (20). With a sequence length $N = 7$, Eq. (20) gives that it is not relevant to consider the correlated PN if $f_c \cdot T \leq 0.71$. This agrees with the critical value measured in Fig. 19 of $f_c \cdot T \simeq 0.853$ greater than 0.71.

3.5.2 Adaptive systems

To guarantee robustness or to maximize spectral efficiency, communication systems implement adaptive modulation schemes. The modulation is inferred from a channel estimation. For sub-THz communications, a link adaptation scheme function of the PN level is highly valuable. Indeed, aggregated bands by sub-THz systems with channel-bonding are wide enough to exhibit differences in oscillators performance between the higher frequencies and the lower ones. In our study, the link adaptation lies in the choice of a differential or coherent modulation and sums up to following question: Is the cumulative PN strong enough to

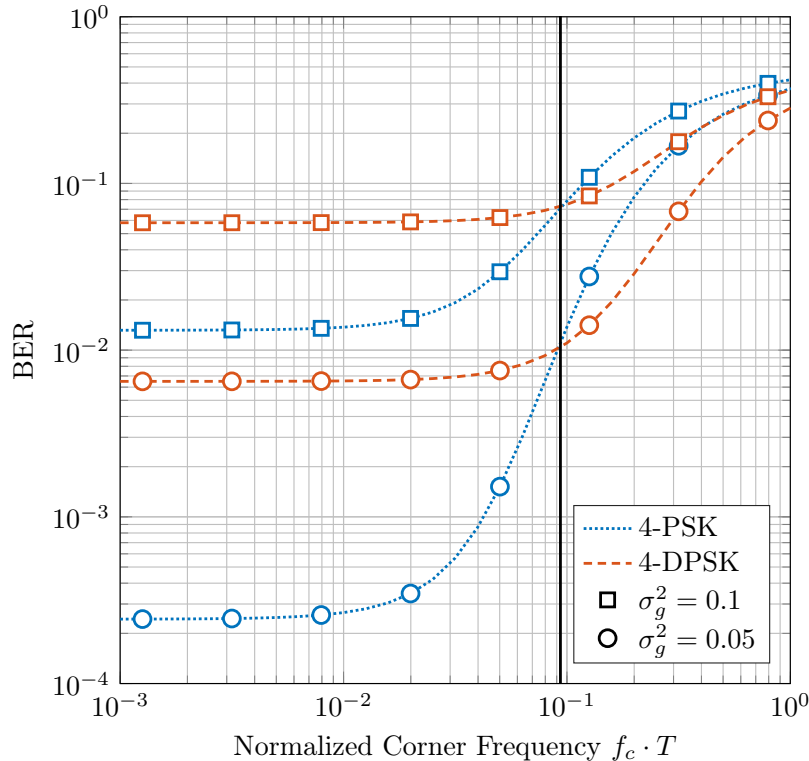


Figure 19: BER performance of PSK and DPSK for correlated PN.

advantage a differential modulation? The link adaptation decision δ takes the following form

$$\delta(\mathbf{r}) = \begin{cases} \text{DPSK}, & \text{if } \sigma_w^2/\sigma_g^2 > \gamma_c, \\ \text{PSK}, & \text{otherwise} \end{cases}, \quad (21)$$

where $\mathbf{r} = (r_1, \dots, r_N)$ is a received sequence of pilots symbols to estimate channel. The link adaptation problem can be expressed as a detection problem

$$\begin{aligned} H_0 : \sigma_w^2/\sigma_g^2 &> \gamma_c, & (\text{correlated PN}), \\ H_1 : \sigma_w^2/\sigma_g^2 &\leq \gamma_c, & (\text{uncorrelated PN}). \end{aligned} \quad (22)$$

This is a very similar problem to the one studied in Sec. 3.4.2. The transceiver has to discriminate between H_0 and H_1 to select the modulation. We have investigated this detection problem in [27] where a statistic of the received pilot sequence has been proposed to perform the link adaptation.

3.6 Conclusion

In this Section 3, we have addressed the problem of PN modeling for sub-THz communications. We have first introduced two PN models: one correlated, accurate but complex, and another uncorrelated, analytically simpler. Next, we have evaluated the accuracy of the uncorrelated Gaussian PN model with a χ^2 goodness of fit test. Simulations have been performed considering realistic PN corresponding to a state-of-the-art 200 GHz oscillator. We have demonstrated that the Gaussian PN model is accurate when the oscillator corner



frequency remains small compared to the system bandwidth. This result has been confirmed by deriving the closed-form expression of the LLR between the correlated and uncorrelated PN models. Given the number of samples in a frame and the normalized corner frequency, an analytical condition has been proposed to select the best PN model between correlated and uncorrelated. Simulation results have shown that an uncorrelated Gaussian process is an appropriate PN model for sub-THz communication systems. Finally, a practical application of model selection has been presented. We have investigated a link adaptation scheme where the transceiver selects the most robust modulation between a coherent and a differential one with regard to the PN performance.

In the hereafter section, we will describe how a modulation scheme can be optimized to minimize the error probability over a Gaussian PN channel.



4 Modulation shaping for phase noise channel

4.1 Introduction

As mentioned previously, sub THz communications suffer from strong phase impairments due to the poor performance of high-frequency oscillators [26] [28]. State-of-the-art approaches [26] investigate the use of coherent systems together with channel bonding. This type of architecture needs to be further combined with signal processing optimization to mitigate the effects of phase impairments. Therefore, one challenge to be addressed for sub-THz systems is the design of robust communications impaired by strong PN.

Assuming a PN channel, the performance of sub-THz communication systems can be improved from both receiver and transmitter sides. First, the receiver algorithms may be adapted to PN channels. An appropriate decision rule for symbol detection is to improve the demodulation performance. It has motivated extensive work on the design of optimum decision rules for systems impacted by PN. The optimum receivers for common PN models are listed in [23]. However, detectors of the literature present complex definitions making the practical implementation challenging, particular when soft-decision decoding is considered. Current communication systems are combined with soft-decision decoding known to improve significantly the demodulation performance. Still, the computability of probabilistic bit values, namely log-likelihood ratios (LLR), has rarely been studied in the literature and should be a prime consideration in this problem. Second, the performance of communication systems may also be enhanced through the optimization of the signal constellation for PN. Choosing M points in a two-dimensional space such that a target function is optimized is a widely investigated problem. In particular, there exists an extensive amount of literature on constellation optimization for PN channels. The following articles are representative of prior work. Research on constellation optimization for PN has begun fifty years ago with Foschini in [16] where signal points are selected among a lattice with a heuristic search to minimize the symbol error probability (SEP) for Tikhonov PN. More recent works have exploited powerful numerical optimization algorithms such as simulated annealing [29] or gradient-search [23] to maximize the mutual information (MI) or minimize the SEP. The work in [15] optimizes amplitude-phase-shift keying (APSK) constellations with a simplex algorithm to minimize the SEP for non-linear PN. The state-of-the-art solution on constellation optimization for Gaussian PN is proposed in [2]: The spiral constellation based on a semi-analytical description, *i.e.* the modulation points are defined with a closed-form expression upon an optimized modulation shape parameter. Nevertheless, most of the constellations proposed in the literature are efficient but local solutions. These schemes are optimized for a specific signal-to-noise ratio (SNR) and PN variance, and thus, does not describe a comprehensive solution. Furthermore, existing solutions are often unstructured which leads to difficult practical implementation with complex binary labeling and demodulation. In contrast to prior work, we investigate in this work a joint optimization of communication performance and implementation on practical systems.

4.2 System Model

4.2.1 Channel model

Theoretical expectations that the line-of-sight (LoS) path provides most of the energy contribution in sub-THz propagation channels have been demonstrated by the recent measurement campaigns within sub-THz bands. The indoor radio propagation channel has been characterized through measurements between 126 and 156 GHz in [21]. Complementary results on non-LoS components can be found in [30]. Sub-THz channels have also been characterized in [31] using deterministic ray-tracing tools. We assume subsequently in this work a LoS propagation channel model.

A single-carrier coherent communication system⁶ impaired by PN is considered. We assume that the effects of the propagation channel are perfectly⁷ compensated and that the receiver is synchronized in time and frequency. We therefore study the discrete-time symbol model of a complex additive white Gaussian noise (AWGN) channel impaired by oscillator PN. The received symbol is then given by

$$r = s \cdot e^{j\phi} + n, \quad (23)$$

where s denotes the transmitted symbol and n is a zero-mean circularly symmetric complex Gaussian variable modeling thermal noise, *i.e.* $n \sim \mathcal{CN}(0, \sigma_n^2)$. The oscillator PN to be modeled is described by ϕ . Transmitted symbols are modulated with duration T and belong to constellation \mathcal{C} with modulation order M and average energy E_s . The power spectral density of thermal noise n is denoted $N_0/2$ such that $\sigma_n^2 = N_0/2T$. The considered discrete-time symbol model in Eq. (3) has been further characterized in [22]. Conditions on the sampling rate and on the PN intensity of the system are given to ensure the accuracy of this model. In the following, we adopt the polar representation and use subscripts ρ and θ to respectively denote the amplitude and phase of a symbol.

With regard to the propagation channel, it is worth pointing out the following remarks. The model in Eq. (3) can be easily adapted to include the propagation gain and phase shift of a frequency-flat channel with a single dominant path, the envisaged model for sub-THz scenarios. This is achieved by integrating a complex coefficient h as follows $r = h \cdot s \cdot e^{j\phi} + n$, where h varies slowly. If the receiver estimates and compensates the channel coefficient h with sufficient accuracy, then the channel can be described with Eq. (3) in a more concise way. The unique resulting difference in the system model would be the definition of the spectral density of thermal noise which should be modified from $N_0/2$ to $N_0/2|h|^2$. Besides, single or multi-carrier systems communicating on multipath channels and impaired by PN have to be described differently and with more complex models, see [32]. Optimizing communication schemes for multipath channels in the presence of PN exceeds the scope of this work – readers may refer to [33]. This work targets sub-THz applications and hence focuses on propagation channels with a single dominant path.

4.2.2 Phase noise model

In communication systems, the generation of PN in oscillators results from the integration and amplification by the phase-locked loop (PLL) of noise sources within the circuitry [19].

⁶The presented results can also be exploited in channel bonding architectures.

⁷The propagation gain and phase shift of the channel are perfectly compensated.

As a result, oscillator PN presents a cumulative and correlated nature. Under the assumption that the oscillator is only subject to white noise, the oscillator PN ϕ can be modeled by the superposition of a correlated Wiener (Gaussian random-walk) process and an uncorrelated Gaussian one [19] respectively expressing the integration and amplification of thermal noise in the PLL. The spectrum of oscillator PN is then described by a colored K_2/f^2 characteristic (Wiener PN) and a white noise floor K_0 (Gaussian PN). Nonetheless, it has been shown in [17] that for high-rate systems the influence of Wiener PN on the communication performance is negligible in comparison to the Gaussian one. In other words, for wide-bandwidth systems, the noise floor of the oscillator is the main contribution to the observed PN. These results have been confirmed in [34] and further characterized through the comparison of a correlated PN model to an uncorrelated one. The main result of this study is that the PN is appropriately modeled by an uncorrelated process if

$$N \cdot f_0^2 \cdot T^2 \leq \frac{\ln(2)}{2\pi^2}, \quad (24)$$

where N is the frame length, f_0 is the corner frequency of the oscillator and T is the symbol duration. Namely, N denotes the number of symbols between two channel estimations and phase corrections. With regard to state-of-the-art sub-THz oscillators and contemplated sub-THz systems parameters [26], it follows that Eq. (20) is easily satisfied. For instance, this condition is satisfied when considering the state-of-the-art oscillator in [1] with $f_0 = 1$ MHz, a system bandwidth $1/T = 1$ GHz and $N = 256$ symbols. For these reasons, it is relevant to model the oscillator PN by a Gaussian distribution such that

$$\phi \sim \mathcal{N}(0, \sigma_\phi^2). \quad (25)$$

The PN variance σ_ϕ^2 is expressed in rad² and may be evaluated from the oscillator spectral characterization using $\sigma_\phi^2 = K_0/T$, where K_0 is the value of the spectral density of the oscillator white noise characteristic. By means of illustration, if we consider a channel bandwidth of $1/T = 1$ GHz, a measured spectral density $K_0 = -100$ dB entails a PN variance $\sigma_\phi^2 = 10^{-1}$. Interested readers may refer to [1] for the spectral characterization of a state-of-the-art sub-THz oscillator. For more details on the PN model selection, we refer the reader to [34] or to [17]. The considered channel described by Eq. (3) and (25) is hereafter referred to as the gaussian phase noise (GPN) channel.

4.3 Receiver Algorithms Design

This section investigates the design of receiver algorithms for the GPN channel. First, we derive the *polar metric* and propose a low-complexity and efficient demodulation scheme. The decision rule for symbol detection, minimizing the SEP, and the corresponding soft-output demapper for coded systems are discussed. Second, we present a pilot-based channel estimation scheme in order to perform the optimum demodulation.

4.3.1 Optimum demodulation

Symbol detection

Regarding symbol-by-symbol detection, the SEP is minimized by the maximum likelihood (ML) decision criterion [35] for equiprobable and independent transmitted symbols. The optimum detection decision rule is expressed upon $p(r|s)$ the channel likelihood function. With the considered channel in Eq. (3), it is appropriate to write the likelihood function as follows

$$p(r|s) = p(r_\rho, r_\theta | s_\rho, s_\theta), \quad (26)$$

and further to express (r_ρ, r_θ) from (s_ρ, s_θ) . We denote the shifted noise $n \cdot e^{-j(s_\theta + \phi)}$ by n' . Since the complex noise is circularly symmetric, n and n' are identically distributed. It follows that the amplitude of the received symbol is given by

$$\begin{aligned} r_\rho &= |(s_\rho + n') \cdot e^{j(s_\theta + \phi)}|, \\ &= \sqrt{(s_\rho + \operatorname{Re}(n'))^2 + \operatorname{Im}(n')^2}, \\ &\simeq s_\rho + \operatorname{Re}(n'), \end{aligned} \quad (27)$$

and the phase by

$$\begin{aligned} r_\theta &= \arg((s_\rho + n') \cdot e^{j(s_\theta + \phi)}), \\ &= s_\theta + \phi + \arctan\left(\frac{\operatorname{Im}(n')}{s_\rho + \operatorname{Re}(n')}\right), \\ &\simeq s_\theta + \phi + \frac{\operatorname{Im}(n')}{s_\rho}. \end{aligned} \quad (28)$$

The two latter equations consider the transmission of non-zero symbols. If a zero symbol is sent, the channel in Eq. (3) is only corrupted by Gaussian noise. The first-order approximations in Eq. (27) and (28) are tight at high SNR. Since high data-rate applications are targeted in this work, it is reasonable to assume a high SNR in order to allow the use of high-order modulation schemes. Accordingly, we further pursue under a high SNR assumption. It is then straightforward from the channel and PN models that

$$\begin{aligned} (r_\rho - s_\rho) &\sim \mathcal{N}(0, \sigma_n^2), \\ (r_\theta - s_\theta) &\sim \mathcal{N}(0, \sigma_\phi^2 + \sigma_n^2/s_\rho^2). \end{aligned} \quad (29)$$

We conclude that the channel likelihood function can be expressed as a bivariate Gaussian distribution:

$$p(r|s) = \frac{\exp\left(-\frac{1}{2}\left(\frac{(r_\rho - s_\rho)^2}{\sigma_n^2} + \frac{(r_\theta - s_\theta)^2}{\sigma_\phi^2 + \sigma_n^2/s_\rho^2}\right)\right)}{2\pi\sqrt{\sigma_n^2(\sigma_\phi^2 + \sigma_n^2/s_\rho^2)}}. \quad (30)$$

This expression leads to the *ML premetric* decision rule originally derived in [36] and given by

$$\hat{s} = \arg \min_{s \in \mathcal{C}} \frac{(r_\rho - s_\rho)^2}{\sigma_n^2} + \frac{(r_\theta - s_\theta)^2}{\sigma_\phi^2 + \sigma_n^2/s_\rho^2} + \log\left(\sigma_\phi^2 + \frac{\sigma_n^2}{s_\rho^2}\right) \quad (31)$$

It has been shown in [36] and [24] that using the ML premetric leads to important performance gains in comparison to standard receivers based on the Euclidean distance – optimum for the complex AWGN channel. Due to its non-constant logarithmic term $\log\left(\sigma_\phi^2 + \frac{\sigma_n^2}{s_\rho^2}\right)$,

this decision rule might be complex to evaluate in practical systems. Further, this decision rule is entitled the ML premetric since it does not define a metric – neither symmetric nor sub-additive – and only a premetric. Exploiting a strong PN assumption, we have proposed in [24] the *polar metric* detection criterion. Its decision rule is given by

$$\hat{s} = \arg \min_{s \in \mathcal{C}} d_\gamma(r, s)^2, \quad (32)$$

where d_γ is the *polar metric* defined by

$$d_\gamma(r, s)^2 = (r_\rho - s_\rho)^2 + \frac{(r_\theta - s_\theta)^2}{\gamma^2}, \quad (33)$$

and $\gamma^2 = \sigma_\phi^2/\sigma_n^2 + 1/E_s$. The proposed detection criterion is the minimization of the distance related to the polar metric. The detected symbol is the closest constellation symbol to the received one. The demodulation therefore consists in a nearest neighbor search. It should be noted that this decision rule is a joint amplitude-phase detector. The polar metric is a weighted combination of the amplitude and phase of the received symbols. The decision rule is adapted to thermal and phase noise variances. When PN gets stronger, the detection relies more and more on the amplitude of received symbols rather than on the phase. Numerical simulations have demonstrated that exploiting a joint amplitude-phase detector rather than a Euclidean one yields valuable detection performance gains [36] [24]. In particular, the error floor in symbol detection caused by PN is significantly lowered by using an appropriate detection criterion. Results in [24] also demonstrate that the performance achieved by the polar metric, with a simpler expression, are identical to the one of the ML premetric at high SNR. One of the advantages of using the polar metric rather than the ML premetric is that the evaluation of distances to perform the detection is simpler to implement on practical systems. We will demonstrate in the following the benefits of the polar metric over the ML premetric. In the case of structured constellations, the polar metric greatly simplifies the implementation of the receiver. With the polar metric, the symbol detection can be simplified as threshold comparisons and the evaluation of soft-bit values can be efficiently approximated with piecewise linear functions. These receiver complexity reductions are not possible with the ML premetric. In addition, the map d_γ verifies the algebraic properties of a metric. Subsequently, we pursue the analysis within the scope of complete metric spaces.

Analytical framework

We present here an original theoretical framework related to the polar metric. This framework enables us to draw a parallel between the GPN channel and the complex AWGN one. In particular, the proposed framework provides the analytical tools to design PN robust communication schemes, which will be used in the following section to optimize the signal constellation. It also gives tools to evaluate many literature proposals related to modulation design for PN channels.

Lemma 1. *Let the complex number s be represented by its polar coordinates $(s_\rho, s_\theta) \in \mathbb{P} = [0, \infty) \times [-\pi, \pi]$. Then the space \mathbb{P}^N - of sequences $\mathbf{s} = \{s_{\rho,k}, s_{\theta,k}\}_{1 \leq k \leq N}$ of N numbers in \mathbb{P} - is a complete metric space when equipped with the metric $d_\gamma : \mathbb{P}^N \times \mathbb{P}^N \mapsto \mathbb{R}^+$ defined by*

$$d_\gamma(\mathbf{x}, \mathbf{y})^2 = \sum_{k=1}^N \left((x_{\rho,k} - y_{\rho,k})^2 + \frac{(x_{\theta,k} - y_{\theta,k})^2}{\gamma^2} \right), \quad \gamma^2 \in \mathbb{R}_*^+, \quad (34)$$

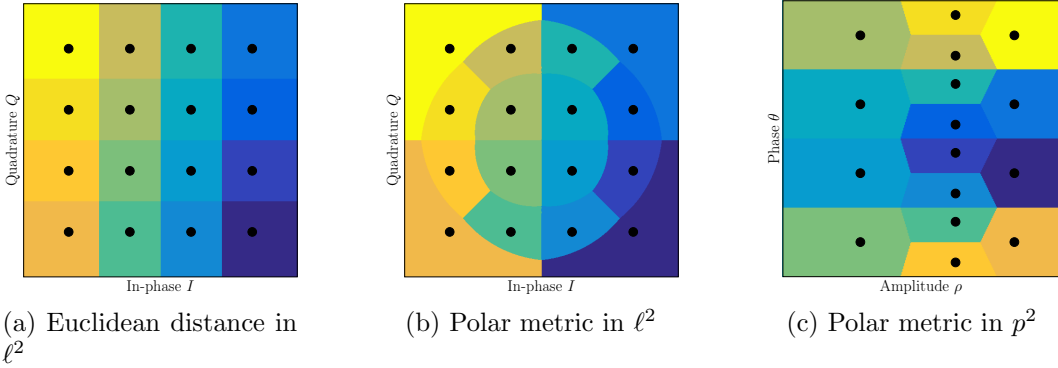


Figure 20: 16-QAM Voronoi regions

for every \mathbf{x}, \mathbf{y} vectors of \mathbb{P}^N .

In the following, p^2 denotes the metric space (\mathbb{P}^N, d_γ) . It results that p^2 is a complete metric space and therefore provides a valuable framework to design efficient algorithms for the GPN channel. For instance, the symbol detection based on nearest neighbor search can be efficiently implemented within p^2 using projections or sphere decoding. Furthermore, it should be noticed that a strong similarity exists between the GPN channel represented in the amplitude-phase domain and the complex AWGN channel in the in-phase quadrature (IQ) plane. This property can be highlighted by approximating, according to Eq. (29), the system model at high SNR as follows

$$(r_\rho, r_\theta) \simeq (s_\rho + n_\rho, s_\theta + n_\theta), \quad (35)$$

where n_ρ and n_θ follow Gaussian distributions. The radial noise n_ρ models the impact of thermal noise on the amplitude. By Eq. (29), we have $n_\rho \sim \mathcal{N}(0, \sigma_n^2)$. The angular noise n_θ models the contributions of both the PN and the thermal noise on the phase. In Eq. (29), the angular noise is given by $n_\theta \sim \mathcal{N}(0, \sigma_\phi^2 + \sigma_n^2/s_\rho^2)$. It should be recalled that the variance of the angular noise n_θ is function of (i) the amplitude of the sent symbol s_ρ (ii) the thermal noise variance σ_n^2 and (iii) the PN variance σ_ϕ^2 . For the GPN channel, the noise on the amplitude and the noise on the phase are Gaussian and independently distributed. This property can also be observed on a complex AWGN channel in the IQ plane where the noise on the real part and the noise on the imaginary part are as well Gaussian and independently distributed. Accordingly, the space p^2 is entitled by analogy to the commonly used discrete signal space ℓ^2 , the space of square-summable complex-valued sequences equipped with the Euclidean inner product.

Fig. 20 depicts the Voronoi regions – the ML decision regions – related to the Euclidean distance and the polar metric for a quadrature amplitude modulation (QAM) with 16 signal points. It illustrates the joint amplitude-phase feature of the polar metric detector. Furthermore, it should be emphasized that the polar metric in the amplitude-phase domain is defined as a weighted Euclidean distance as illustrated on Fig. 20.(c). Altogether, the latter property highlight the strong similarity between GPN and complex AWGN channels which will be used further to optimize the modulation scheme.

Probabilistic demapper

It is of practical interest to consider the integration of a forward error correction (FEC) scheme in order to achieve a channel coding gain. Channel coding is usually combined with soft-decision decoding known to significantly improve the performance of channel decoders. We therefore propose in this paragraph to study the probabilistic demapper based upon the polar metric.

In practical communication systems, computing the exact values of the bit LLRs may be too complex. Therefore, close approximations of the bit LLRs are evaluated to be computed efficiently. We consider a bit-interleaved coded modulation (BICM) architecture. Let the symbol s map the binary word $\mathbf{b} = (b_1, \dots, b_{\log_2(M)})$. Regarding the detection of bit b_i , the decision \hat{b}_i minimizing the error probability is derived from the ML criterion [25]. We have

$$\hat{b}_i(r) = \begin{cases} 1, & \text{if } L_i(r) > 0 \\ 0, & \text{otherwise} \end{cases}, \quad (36)$$

where the LLR L_i of the bit b_i is given by

$$L_i(r) = \log \left(\frac{p(b_i = 1|r)}{p(b_i = 0|r)} \right). \quad (37)$$

The sign of L_i is used to infer the detection decision and its absolute value $|L_i|$ quantifies the reliability of this decision. Since transmitted symbols are equiprobable, we can express with Bayes' theorem the LLR as

$$L_i(r) = \log \left(\frac{\sum_{s_1 \in \mathcal{C}_1^i} p(r|s_1)}{\sum_{s_0 \in \mathcal{C}_0^i} p(r|s_0)} \right). \quad (38)$$

We adopt the notation \mathcal{C}_β^i to describe the subset of the constellation symbols such that $b_i = \beta$. To simplify the computation of soft bit values, we derive sub-optimal LLRs expressions using the *log-sum* approximation: $\log(\sum_k x_k) \simeq \max_k \log(x_k)$. This approximation is tight at high SNR and is commonly used in practical communications systems for conventional modulation schemes such as QAM [37]. It has been shown in [37] and in [38] that the log-sum approximation does not lead to any significant performance loss, even at low SNR. Subsequently, we obtain

$$L_i(r) \simeq \max_{s_1 \in \mathcal{C}_1^i} \log(p(r|s_1)) - \max_{s_0 \in \mathcal{C}_0^i} \log(p(r|s_0)). \quad (39)$$

The channel decoding algorithms implemented in practical systems are not impacted by a normalization factor, for instance the *min-sum* decoder for LDPC codes. For this reason, the approximations of the LLRs are further expressed upon the polar metric introduced in Eq. (33) by

$$L_i(r) \simeq \min_{s_0 \in \mathcal{C}_0^i} d_\gamma(r, s_0)^2 - \min_{s_1 \in \mathcal{C}_1^i} d_\gamma(r, s_1)^2. \quad (40)$$

The proposed bit LLR values in the latter expression can be easily evaluated. The computation of bit LLR values relies on the polar metric d_γ , and therefore, requires only the evaluation

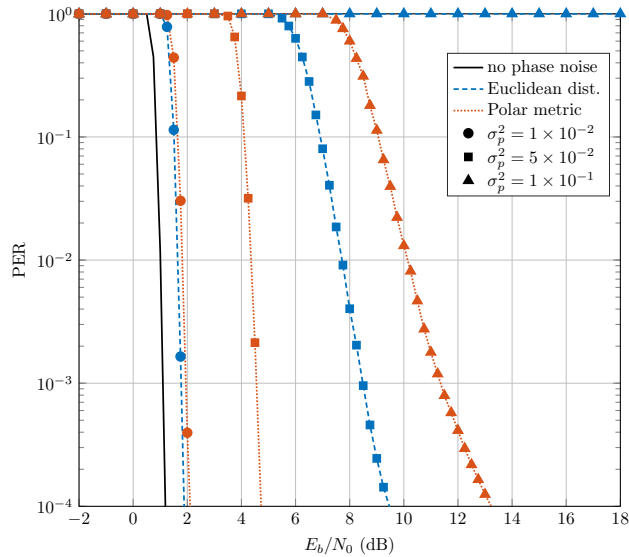


Figure 21: Performance of a LDPC coded 16-QAM with LLR based on the Euclidean distance or on the polar metric for different PN variances σ_ϕ^2

of few weighted Euclidean distances within p^2 . In comparison, if the LLR computation is based on Eq. (38), the receiver is required to evaluate of several logarithmic terms as well as multiple sums of Gaussian functions of the received symbol. It should be further highlighted that such complexity reductions are not possible with the ML premetric as this decision rule implies several non-constant logarithmic terms. For this reason, the new soft-output demapper proposed in Eq. (40) allows significant complexity reductions of the receiver in comparison to state-of-the-art detectors [36]. It is worth mentioning that the expression in Eq. (40) of the bit LLRs remains valid if the propagation channel is considered by integrating a complex coefficient h to Eq. (3). The unique difference is that the variance of the thermal noise should be adapted.

Let us now evaluate the demodulation performance of coded systems over the GPN channel. The implemented FEC scheme is a LDPC code respecting the 5G new radio (5G-NR) specifications [39] with an input packet size of 1500 bytes, a coding rate of 0.8 and a *min-sum* decoder. LDPC codes demonstrate excellent performance with highly parallelizable decoder architectures. Therefore, they are considered as a foremost solution for error-correcting codes in high-rate communication systems. Fig. 21 presents the packet error rate (PER) performance of a coded 16-QAM for different values of PN variance and demodulation schemes. Simulated PER have been obtained by Monte-Carlo simulations. Results show that important demodulation performance gains are achieved by the polar metric in comparison to the Euclidean detector. For low values of SNR and PN variance, the Euclidean detector performs slightly better than the polar metric (< 0.1 dB). This minor performance loss results from the assumptions of a high SNR, and a strong PN used to derive the polar metric decision rule. When the PN variance gets stronger, the performance gain of the polar detector in comparison to the Euclidean one becomes significant – *e.g.* > 4 dB for $\sigma_\phi^2 = 5 \times 10^{-2}$. For strong PN variances, the PER of the receiver using the Euclidean distance is 1 for any SNR as the iterative decoder never converges. In contrast, the receiver based on polar metric demonstrates the waterfall feature of LDPC codes and can achieve low error rate communications.

The presented PN variances: $\sigma_\phi^2 = 1 \times 10^{-2} \text{ rad}^2$, $\sigma_\phi^2 = 5 \times 10^{-2} \text{ rad}^2$ and $\sigma_\phi^2 = 1 \times 10^{-1} \text{ rad}^2$ respectively correspond to an oscillator noise floor spectral density K_0 of -120 dB , -110 dB and -100 dB for a channel bandwidth of 1 GHz . Though more complex to compute, the demodulation algorithm based on ML premetric demonstrates identical performance to the one using polar metric one, and hence, is not presented. The proposed demodulation scheme has been assessed for QAM, yet remains valid for any modulation scheme. Ultimately, these results highlight that the proposed demodulation scheme based on the polar metric achieves important performance gains on the GPN channel with valuable complexity reductions of the receiver. Using channel statistics to properly represent the signal and optimize the communication algorithms is widely used. For instance, this is implemented in the orthogonal time frequency space (OTFS) waveform [40].

4.3.2 Channel estimation

The previous subsection has shown that knowledge of the channel statistics may be used to improve the performance of the receiver. Therefore, estimations of thermal and PN variances: σ_n^2 , σ_ϕ^2 are required. The PN variance σ_ϕ^2 results from the combination of two PN processes issued by the transmitter and the receiver oscillators, hence is not inherent to the receiver only. Estimation of σ_n^2 and σ_ϕ^2 may be realized by inserting N_p pilot symbols and by evaluating the appropriate estimators. The pilot symbols denoted $\mathbf{s} = (s_1, s_2, \dots, s_{N_p})$ are known from the receiver and possibly distributed. The joint likelihood function of the N_p received pilot symbols $\mathbf{r} = (r_1, \dots, r_{N_p})$ is given by

$$p_{N_p}(\mathbf{r} | \mathbf{s}, \sigma_n^2, \sigma_\phi^2) = \prod_{k=1}^{N_p} p(r_k | s_k, \sigma_n^2, \sigma_\phi^2). \quad (41)$$

It should be mentioned that here $k \in \{1, \dots, N_p\}$ is the index of pilots symbols and may refer to non-consecutive received symbols. In the following we set pilot symbols to have a constant amplitude $\sqrt{E_s}$. The average symbol energy E_s is considered perfectly known as it can be estimated blindly through all sent symbols. It follows from the definition of the channel likelihood function in Eq. (30) that the ML estimators of σ_n^2 and σ_ϕ^2 are written as

$$\begin{aligned} \hat{\sigma}_n^2 &= \frac{1}{N_p} \sum_{k=1}^{N_p} (|r_k| - \sqrt{E_s})^2, \\ \hat{\sigma}_\phi^2 &= \frac{1}{N_p} \sum_{k=1}^{N_p} (\underline{r}_k - \underline{s}_k)^2 - \frac{\hat{\sigma}_n^2}{E_s}. \end{aligned} \quad (42)$$

We express these estimators as $\chi_{N_p}^2$ distributions to evaluate their biases and dispersions. That is

$$\begin{cases} E[\hat{\sigma}_n^2] = \sigma_n^2 \\ V[\hat{\sigma}_n^2] = \frac{2\sigma_n^4}{N_p} \end{cases}, \quad \begin{cases} E[\hat{\sigma}_\phi^2] = \sigma_\phi^2 \\ V[\hat{\sigma}_\phi^2] = \frac{2(\sigma_\phi^2 + \sigma_n^2/E_s)^2}{N_p} + \frac{2\sigma_n^4}{N_p E_s} \end{cases}. \quad (43)$$

It is clear that these estimators are unbiased. In addition, it is of practical interest to compare the proposed estimators to their Cramer-Rao lower bounds (CRLB) [41] since the regularity

conditions are satisfied by the likelihood function in Eq. (30). The corresponding CRLBs are given by

$$V[\hat{\sigma}_n^2] \geq \frac{2\sigma_n^4}{N_p}, \quad V[\hat{\sigma}_\phi^2] \geq \frac{2(\sigma_\phi^2 + \sigma_n^2/E_s)^2}{N_p}. \quad (44)$$

It is shown that the thermal noise variance estimator achieves the CRLB. The estimator of the PN variance is tight to the CRLB but does not achieve it. Nevertheless, it is possible to demonstrate that the proposed estimators present the smallest mean square error among any unbiased estimators. It is immediate that the joint probability density function p_{N_p} belongs to the exponential family. Therefore, statistic $S = (\sum_{k=1}^{N_p} (|r_k| - \sqrt{E_s})^2, \sum_{k=1}^{N_p} (\underline{r}_k - \underline{s}_k)^2)$ is complete and sufficient for parameter $(\sigma_n^2, \sigma_\phi^2)$. We can conclude from the Lehman-Scheffé theorem that the proposed unbiased estimators $(\hat{\sigma}_n^2, \hat{\sigma}_\phi^2)$ defined upon S are the unique minimum-variance unbiased estimators of σ_n^2 and σ_ϕ^2 .

The effect of a propagation channel with a single dominant path could be modeled by integrating a complex coefficient h to Eq. (3). Nonetheless, the estimation of the channel coefficient required for equalization is not carried out here. The necessary framework has been proposed such that the estimation of the channel complex coefficient is straightforward to derive.

4.4 Modulation Scheme Design

The previous section has investigated the design of receiver algorithms and thereby has unveiled valuable information on the GPN channel. We have previously considered a fixed modulation scheme to determine the optimum receiver. Nevertheless, it is clear that conventional modulation schemes such as QAM or phase-shift keying (PSK) are not suited to PN channels. This section is dedicated to the design of the modulation scheme for the GPN channel. A theoretical analysis is presented to construct PN robust constellations. Thereupon, we propose the Polar-QAM scheme. The constellation and the binary labeling of the Polar-QAM are jointly designed to improve communication performance on strong PN channels with a simple implementation. The performance analysis of the proposed modulation is pursued analytically and numerically to demonstrate the performance gains over conventional and state-of-the art schemes.

4.4.1 Optimum constellation from sphere packing

Let us investigate the problem of finding the constellation, *i.e.* the set of signal points in the complex plane, that minimizes the SEP for a given channel. The number of points is fixed to M and the constellation average energy is constrained to E_s . For a transmitted symbol, the SEP may be defined upon its complementary event, the probability of correct detection, as follows

$$P(E|s) = 1 - P(\hat{s} = s|s). \quad (45)$$

With regard to a detection rule defined upon the ML criterion, the probability of correct detection is proportional to the integration of the likelihood function over the Voronoi region of the symbol. That is

$$P(\hat{s} = s|s) \propto \int_{\mathcal{V}_s} p(r|s) dr, \quad (46)$$

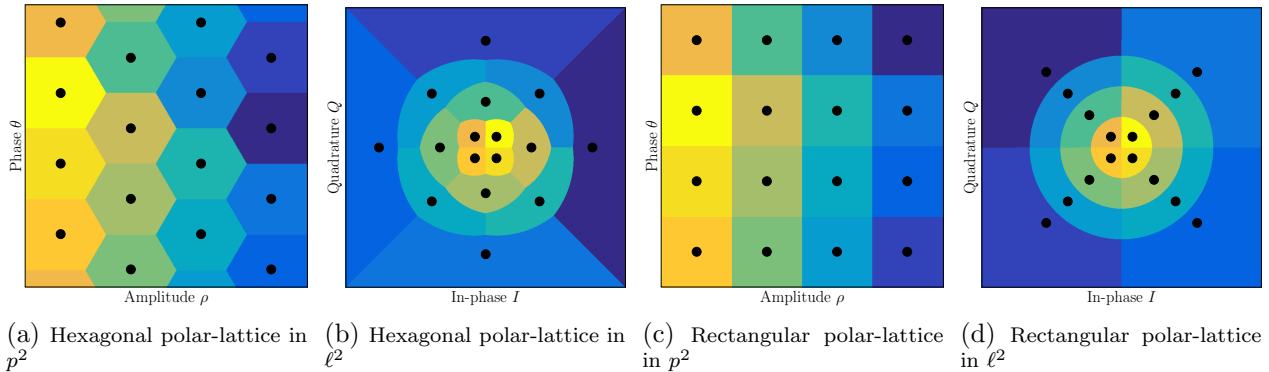


Figure 22: Voronoi regions for the polar metric of polar-lattice based constellations with 16 signal points

where \mathcal{V}_s is the Voronoi region of symbol s and $p(r|s)$ is the channel likelihood function. It follows that the larger the areas of the Voronoi regions, the smaller the error probability. This result is valid for any channel, yet let us consider the GPN channel. We are hence looking for the constellation that maximizes the areas of Voronoi regions defined by the polar metric. By way of illustration, it is clear on Fig. 20 that the QAM constellation does not maximize the areas of the Voronoi regions for the polar metric and is thus not optimal for the GPN channel. As previously stated, the proposed constellation in the literature lead to difficult implementations due to their lack of structure. We therefore investigate constellations defined upon lattices in the amplitude-phase plane. Since the ML detector in Eq. (32) describes a phase-amplitude detector, we study the optimal lattice-based constellation problem within p^2 . It results that the noise distribution is circular⁸ in p^2 for high SNR and strong PN scenarios. The modulation order and the average energy of the constellation being fixed, the problem of finding the lattice that maximizes the areas of the Voronoi regions can be regarded as finding the densest sphere packing in a two dimensional space. The well-known result of this problem gives that the highest density in the plane is achieved by the hexagonal lattice [42]. Subsequently, a constellation based upon a hexagonal structure is to maximize the areas of the Voronoi Regions [43], and thus, minimizes the SEP. Nevertheless, we consider hereafter the use of a rectangular polar-lattice to define a modulation scheme with the intention to ease the demapping implementation. For the purposes of illustration, Fig. 22 presents the IQ and amplitude-phase representations of the hexagonal and rectangular polar-lattice based constellation. Fig. 22 depicts the Voronoi regions, for the polar metric, of the constellations based on polar-lattice. We will show in the following paragraph that though a hexagonal lattice performs better in terms of error probability than a rectangular one, the performance gain is small and the complexity increase is significant. Therefore, the proposed Polar-QAM scheme relies on a rectangular polar-lattice.

We have previously highlighted the similarity between the GPN channel and the complex AWGN one. Thanks to the analytical framework described in this section, it follows that the derivation of the optimum lattice-based constellation for the GPN channel in the polar domain is highly similar to the one for the complex AWGN channel in the IQ plane – see [35].

⁸The noise distribution is actually ellipsoidal in the amplitude-phase plane, yet is circular in p^2 with the axis scaling γ .

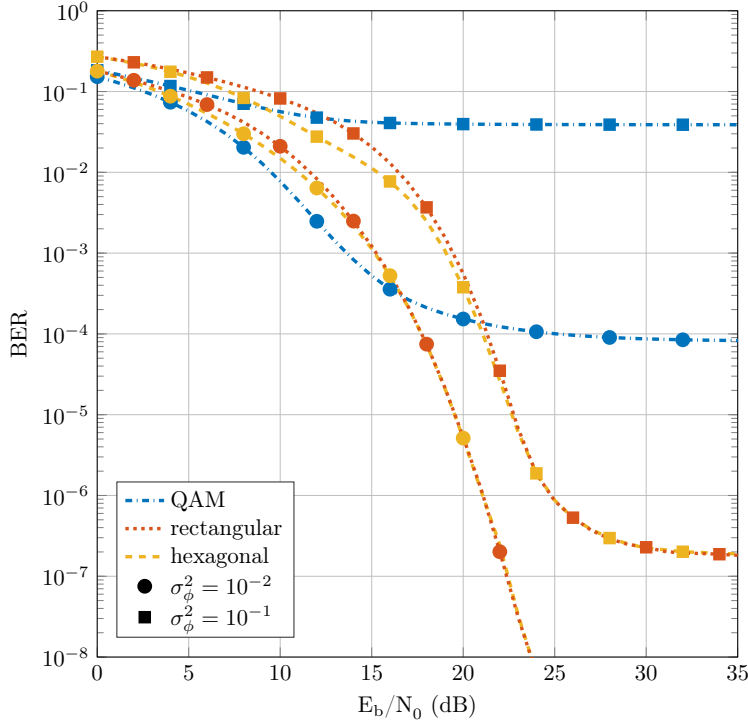


Figure 23: BER performance of different constellations with $M = 16$ on the GPN channel

Likewise, the optimal constellation for the complex AWGN channel relies on a hexagonal lattice in the IQ plane and is referred to as the hexagonal-QAM (HQAM). Though the HQAM demonstrates a performance gain in comparison to the QAM using a rectangular lattice [44], the rectangular QAM remains the most exploited modulation scheme for its simple implementation.

4.4.2 Performance of constellations based on polar-lattices

We discuss here the results of numerical simulation concerning the BER performance of the different constellations based on polar-lattices. The implemented symbol detection rule is the polar metric. The BER performance for different PN variances of the QAM and the polar-lattice based solutions are outlined in Fig. 23 with $M = 16$. First, we can remark that the optimized constellations are sub-optimal at low SNR. The previous analysis on the design of PN robust constellations is correct under a high SNR assumption. In the low SNR regime, the channel is dominated by thermal noise, even in the presence of strong PN, and in this case, conventional modulation schemes should be preferred. However, it is shown that the constellation of the QAM reaches an error floor due to PN which can be high for strong PN scenarios. Conversely constellation based on polar-lattice achieve significant performance gains and enable low error rate communications on strong PN channels. These results exhibit the performance gain of hexagonal lattice over the rectangular one, but at the detriment of a complexity increase of the demodulation algorithm.

The performance analysis can be improved by studying the achievable information rates (IR) related to the constellations. Fig. 24 compares the achievable rates of the different constellations for AWGN and GPN channels. The presented achievable IR have been obtained

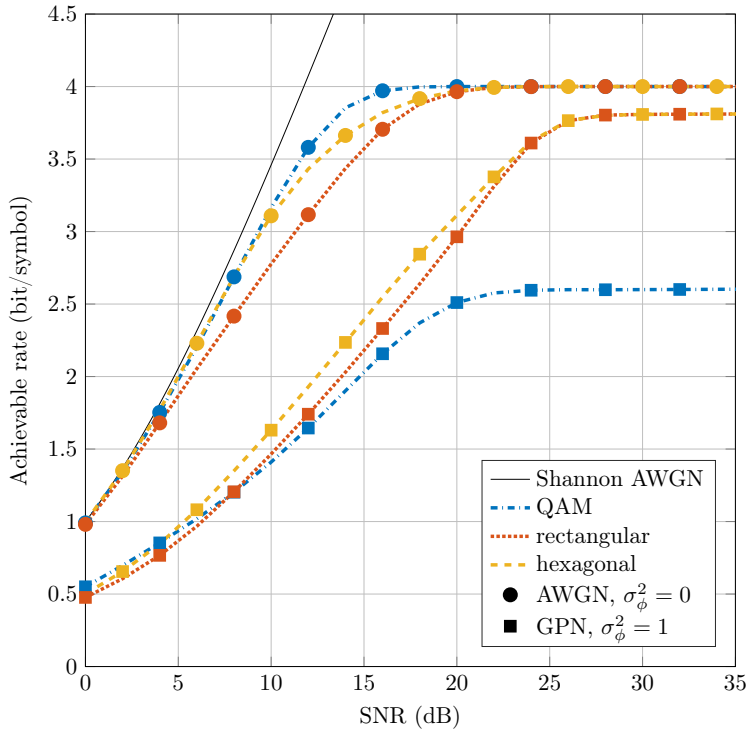


Figure 24: Achievable rates in bit/symbol for different constellations and $M = 16$

through Monte-Carlo simulations as described in [45]. Given a channel and a constellation, the achievable rate is evaluated by computing numerically the mutual information of the transmitted and received symbols. Our results demonstrate that the achievable rate of the QAM scheme is severely limited by PN. Therefore, we conclude that the optimization of the modulation scheme is essential to target high-rate communications on the GPN channel, and moreover, that constellations based on polar-lattices are a relevant solution.

In contrast to constellations obtained through numerical optimization [23], modulation schemes defined upon polar-lattices present an analytical signal points expression, and hence, result in a plain signal generation at the transmitter. Furthermore, the binary labeling regarding BICM architectures is trivial. In this case, the binary labeling in the polar domain is identical to the labeling in the IQ plane of a QAM for a rectangular lattice and respectively to a HQAM for a hexagonal lattice. The difference in implementation between the use of a hexagonal and a rectangular lattice to define the constellation is the following. It has been shown previously that the symbol detection is defined as a nearest neighbor search. As a result, this detection for a rectangular polar-lattice relies on simple threshold comparisons in the polar domain, as it can be observed on Fig. 22c, which entails a simple demodulation algorithm. In addition, the bit LLR values related to a rectangular lattice and necessary to channel decoding can be approximated as piecewise linear functions in the amplitude-phase domain. These two complexity reductions at the receiver are enabled only with the use of a rectangular polar-lattice and not a hexagonal one. In conclusion, a constellation based on a hexagonal polar-lattice, in comparison to a rectangular one, leads to relatively small performance gains – see Fig. 23 and 24 – yet at the detriment of a more complex receiver. Therefore, we propose a modulation scheme based on a rectangular polar-lattice:

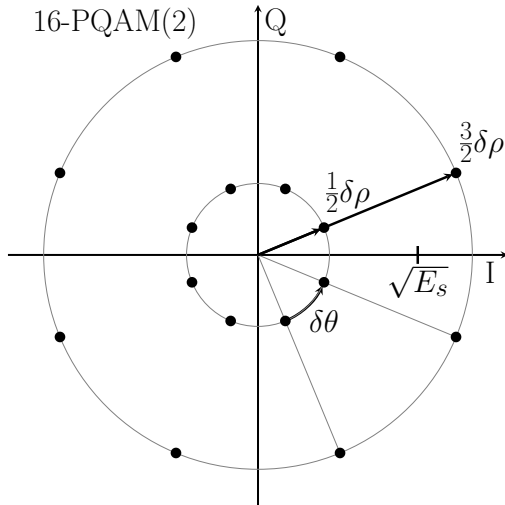


Figure 25: Illustration of a 16-PQAM(2) in the complex plane

the Polar-QAM.

It is interesting to mention that state-of-the-art approaches [23] [2] [46] on PN channels shape the constellations toward hexagonal and rectangular polar-lattices. For instance, the representation of the circular-QAM proposed in [46] in the amplitude-phase domain is close to a hexagonal lattice. Further, it has been shown in [46] that the circular-QAM realizes, in comparison to a conventional QAM, performance gains on PN channels. Similarly, it is worth studying the Gray-APSK proposed in [47] to provide a shaping gain for satellite communications. Signal points of the Gray-APSK represented in the amplitude-phase domain nearly describe a rectangular lattice, the amplitudes of signal points are non-linearly distributed though. Thanks to the presented analysis, we can conclude that such modulation scheme should provide valuable performance gains on PN channels. Eventually, the following remark should be pointed out. We have presented here a theoretical analysis based on the signal decomposition in the amplitude-phase domain to optimize the modulation scheme for the GPN channel. This original analysis provides a valuable theoretical framework to design PN robust communication schemes and also to evaluate many of the literature proposals.

4.4.3 Polar-QAM

The proposed Polar-QAM is defined by the constellation \mathcal{C} illustrated in Fig. 25. With $m, n \in \mathbb{N}$ and $m \geq n$, the constellation \mathcal{C} is a set of $M = 2^m$ complex points placed on $\Gamma = 2^n \in \{1, 2, 4, \dots, M\}$ concentric circles, *i.e.* amplitude levels. The average energy of the constellation is denoted E_s . Each of the Γ circles contains M/Γ signal points. Correspondingly, the *minimum angular distance* $\delta\theta$ between two symbols is

$$\delta\theta = \frac{2\pi\Gamma}{M}. \quad (47)$$

The phase shift θ_p of the p -th symbol on a circle is described by $\theta_p = \frac{\delta\theta}{2}(2p - 1)$. Likewise, the amplitude ρ_q of the q -th circle ρ_q is defined by $\rho_q = \frac{\delta\rho}{2}(2q - 1)$ where $\delta\rho$ is the *minimal radial distance*. It results from this definition of the amplitudes of signal points and from the

average symbol energy E_s that the minimal radial distance $\delta\rho$ is given by

$$\frac{\delta\rho}{\sqrt{E_s}} = \sqrt{\frac{12}{4\Gamma^2 - 1}}. \quad (48)$$

Then, any PQAM constellation can be entirely defined by two parameters M and Γ respectively the modulation order and shape. Therefore, we use the notation $M\text{-PQAM}(\Gamma)$ to described the constellation

$$\mathcal{C} = \left\{ \frac{\delta\rho}{2} (2q - 1) \cdot \exp\left(j \cdot \frac{\delta\theta}{2} (2p - 1)\right) \mid 1 \leq q \leq \Gamma, 1 \leq p \leq M/\Gamma \right\}. \quad (49)$$

One may remark that some particular cases of the PQAM fall into known modulations: a $M\text{-PQAM}(M/2)$ describes an amplitude-shift keying while a $M\text{-PQAM}(1)$ is a PSK. The PQAM is a structured definition of an APSK constellation. For the demodulation of the PQAM on the GPN channel, it is relevant to use the proposed detection scheme based on the polar metric. When this demodulation scheme is used, the symbol detection for the PQAM can be implemented with a simple threshold detection in the amplitude-phase domain.

Nonetheless, the PQAM is not only defined by its constellation but also by its binary labeling. For a given channel, optimizing the symbol mapping in order to minimize the bit error rate (BER) is not trivial and induces a high complexity – *cf.* binary switching algorithm [48]. Thanks to the regular structure of the PQAM, an efficient binary labeling can be proposed in order to achieve robustness and simple demodulation. In a 2^m -ary modulation system, every m bits form a binary word $\mathbf{b} \in \{0, 1\}^m$, which is modulated to a symbol $s \in \mathcal{C}$ under a mapping rule called constellation labeling μ ,

$$\mu : \{0, 1\}^m \rightarrow \mathcal{C}. \quad (50)$$

To minimize the bit error probability, the mapping rule must implement a Gray code. Namely, a Gray code mapping consists in labeling the M points with binary words of length $m = \log_2(M)$ such that the Hamming distance between two nearest points is equal to 1. Subsequently, incorrectly estimating a symbol by one of its nearest neighbors leads to a single bit error. In the case of a $M\text{-PQAM}(\Gamma)$, any binary words $\mathbf{b} \in \{0, 1\}^{\log_2(M)}$ mapped to a symbol s may be expressed as

$$\mathbf{b} = (b_1^\rho, \dots, b_{\log_2(\Gamma)}^\rho, b_{\log_2(\Gamma)+1}^\theta, \dots, b_{\log_2(M)}^\theta) \quad (51)$$

where $\log_2(\Gamma)$ bits are encoded by the amplitude level s_ρ of s , and $\log_2(M/\Gamma)$ bits are encoded by the phase s_θ of s . Therefore, the mapping rule μ may be subdivided into two uni-dimensional rules μ_ρ and μ_θ :

$$\begin{aligned} \mu_\rho : \{0, 1\}^{\log_2(\Gamma)} &\rightarrow s_\rho, \\ \mu_\theta : \{0, 1\}^{\log_2(M/\Gamma)} &\rightarrow s_\theta. \end{aligned} \quad (52)$$

Uni-dimensional mapping of signal points respecting a Gray code is straightforward and a well-known result. It is worth mentioning that the PQAM constellation has been designed to achieve such efficient binary labeling. Fig. 26 depicts the binary labeling for a 16-PQAM(4). Conversely, optimized constellations of the literature present no particular structure and lead

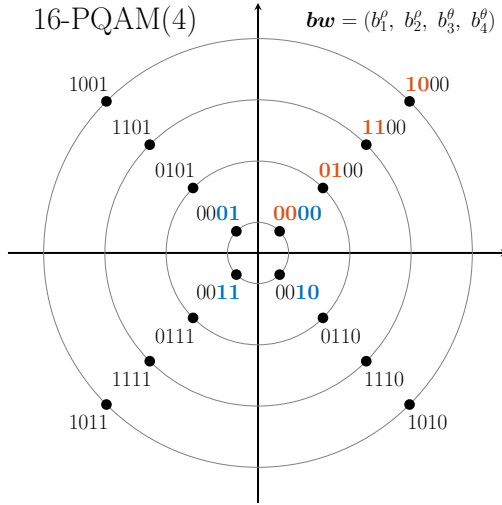


Figure 26: Binary labeling of a 16-PQAM(4)

to complex labeling and poor performance in terms of BER. Besides, the binary labeling of the Polar-QAM allows low-complexity evaluation of the bit LLR. When the PQAM is used with the proposed soft-output demapper based on the polar metric, the soft-bit values can be efficiently approximated with piecewise linear functions. The piecewise linear approximations of the LLR of the $\log_2(\Gamma)$ bits related to the amplitude level present similar expressions to the ones of a QAM constellation, see [49]. While for the $\log_2(M/\Gamma)$ bits encoded on the phase, approximations are similar to a PSK [50]. The evaluation of the bit LLRs based on piecewise linear functions is an important complexity reduction of the receiver. This complexity reduction highlights the benefits of using the PQAM and the proposed demodulation scheme over state-of-the-art solutions, based on numerically optimized constellations. It also emphasizes the relevance of jointly optimizing the modulation and demodulation schemes.

4.4.4 Theoretical performance analysis

By definition of the PQAM and the expression of the likelihood function, we can approximate the detection error probability $P(E)$ by

$$\begin{aligned}
 P(E) &= \frac{1}{M} \sum_{s \in \mathcal{C}} P(\hat{s} \neq s|s) = \frac{1}{M} \sum_{s \in \mathcal{C}} (1 - P(\hat{s} = s|s)), \\
 &\simeq \frac{1}{M} \sum_{s \in \mathcal{C}} \left(1 - p\left(-\frac{\delta\rho}{2} < (s_\rho - r_\rho) < \frac{\delta\rho}{2}\right) \cdot p\left(-\frac{\delta\theta}{2} < (s_\theta - r_\theta) < \frac{\delta\theta}{2}\right) \right), \quad (53) \\
 &\simeq 2Q\left(\frac{\delta\rho}{2\sigma_n}\right) + 2Q\left(\frac{\delta\theta}{2\sqrt{\sigma_\phi^2 + \sigma_n^2/E_s}}\right).
 \end{aligned}$$

The latter approximation holds for high SNR and corresponds to the widely used assumption that errors occur on the nearest neighbors of the sent symbol. To simplify the closed form expression in Eq. (53), it is assumed that the average detection errors on the phase of symbols occur for an amplitude of $\sqrt{E_s}$ which is slightly optimistic. Since the binary labeling

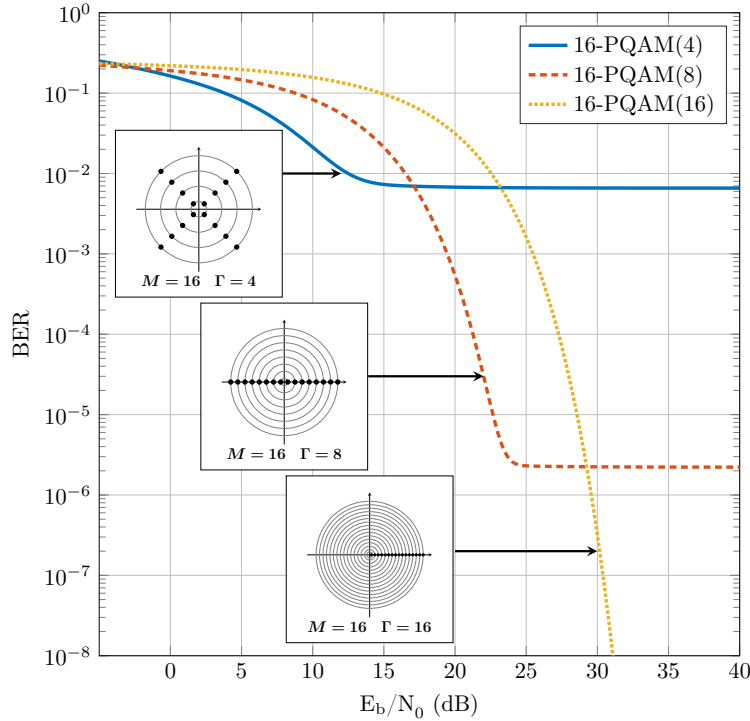


Figure 27: Analytical performance of a 16-PQAM(Γ) for modulation shape $\Gamma \in \{4, 8, 16\}$ with PN variance $\sigma_\phi^2 = 1.25 \times 10^{-1}$

implements a Gray code mapping and under the nearest neighbors error assumption, the bit error probability P_{be} may be derived from the symbol detection error probability as

$$P_{be} = \frac{P(E)}{\log_2(M)}. \quad (54)$$

Let us replace $\delta\rho$ and $\delta\theta$ by their definitions in Eq. (47) and (48) to express the BER as a function of E_b/N_0 , σ_ϕ^2 , M and Γ . Hereafter, it is assumed that $T = 1$ which results in no loss of generality. The average bit energy $E_b = E_s / \log 2(M)$ and the noise power spectral density $N_0 = 2\sigma_n^2$. Eventually, the BER of a M -PQAM(Γ) can be approximated by the following closed-formed expression

$$P_{be} \simeq \frac{2}{\log_2(M)} \left(Q \left(\sqrt{\frac{6 \cdot \log_2(M) \cdot E_b/N_0}{4\Gamma^2 - 1}} \right) + Q \left(\frac{\pi\Gamma}{M \sqrt{\sigma_\phi^2 + \frac{1}{E_b/N_0 \cdot 2 \cdot \log_2(M)}}} \right) \right). \quad (55)$$

In the BER expression, the two terms in the addition should be interpreted differently. The first term expresses the probability of misestimating the amplitude level of the received symbol whereas the second one the phase. Fig. 27 outlines the analytical BER performance of a 16-PQAM(Γ) for $\Gamma \in \{4, 8, 16\}$ and their respective constellations. As depicted in Fig. 27, the BER reaches an error floor when E_b/N_0 tends to infinity due to PN. This error floor is given by

$$\lim_{E_b/N_0 \rightarrow \infty} P_{be} = \frac{2}{\log_2(M)} Q \left(\frac{\pi\Gamma}{M\sigma_\phi} \right). \quad (56)$$

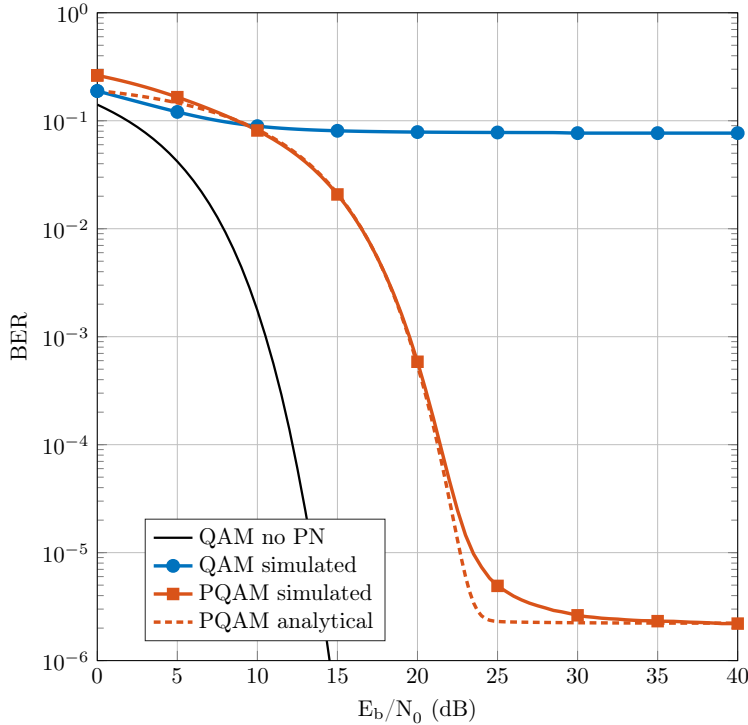


Figure 28: 16-QAM and 16-PQAM(8) performance with PN variance $\sigma_\phi^2 = 1.25 \times 10^{-1}$

It is shown in Fig. 27 and in Eq. (56) that the smaller Γ , the higher the error floor. For a PN channel, the error floor of a constellation is caused by several signal points using the same amplitude level and can be lowered by increasing the minimum angular distance. In brief, a large number of amplitude levels Γ entails a low error floor, yet attained at a higher E_b/N_0 .

With regard to the radio-frequency (RF) power-amplifiers, directly related to the energy consumption of transmitters, the peak-to-average power ratio (PAPR) is a key performance indicator for any communication system. In the context of the Polar-QAM, the PAPR is given by

$$\max_{s \in \mathcal{C}} \frac{|s|^2}{E_s} = 3 \cdot \frac{2\Gamma - 1}{2\Gamma + 1}. \quad (57)$$

It can be noticed that the PAPR is a strictly increasing function of the number of amplitude levels Γ and is not function of the modulation order M . As previously mentioned increasing Γ does improve the PN robustness at the detriment of a higher PAPR. Finally, the closed-form expressions of the BER and the PAPR of the Polar-QAM provide new and valuable results for the specification and analysis of future systems. The theoretical analysis of such important performance metrics is not possible for the numerically optimized constellations of [23] or the state-of-the-art modulation proposed in [2]. This further motivates the use of a structured constellation, and also, the joint optimization of the modulation and demodulation schemes.

4.4.5 Numerical simulations results

The results of numerical simulations for uncoded systems are presented in Fig. 28. The BER performance of the QAM and PQAM are compared for $M = 16$ and $\sigma_\phi^2 = 1.25 \times 10^{-1}$.

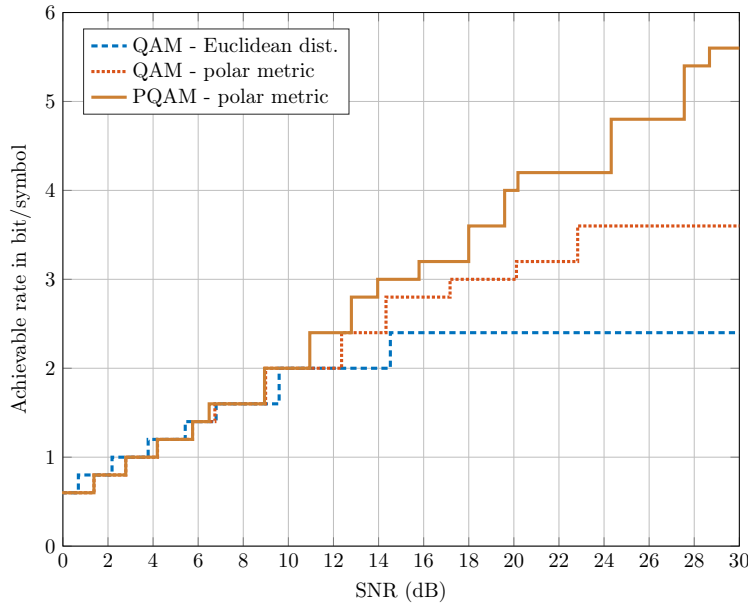


Figure 29: Achievable rate in bit/symbol of the QAM and PQAM schemes with a LDPC code and PN variance $\sigma_\phi^2 = 10^{-1}$

The demodulation with the polar metric detector is implemented. Results demonstrate the performance gain achieved by the PQAM constellation over a conventional QAM on a strong GPN channel. The QAM constellation presents a high error floor which results from the low angular distance between its signal points. Nonetheless, it is worth mentioning that this performance gain is achieved to the detriment of the PAPR. A 16-QAM presents a PAPR of 2.55 dB while the 16-PQAM(8) exhibits a 4.23 dB PAPR. It is also illustrated that the analytical expression of the BER for a PQAM is tight to the simulation results. Nevertheless, the optimistic consideration made in Eq. (53) is to explain the slight difference between the analytical expression and the simulation results.

Fig. 29 presents the results of numerical simulation for coded systems. It outlines the achievable rate in bit/symbol for $\sigma_\phi^2 = 10^{-1}$ and a LDPC code. Three modulation/demodulation schemes are considered: QAM with Euclidean detector, QAM with polar detector and PQAM with polar detector. The FEC scheme is based on the 5G-NR LDPC and is implemented with an input packet size of 1500 bytes and a coding rate ranging from 0.3 to 0.9. The communication performance has been characterized to determine the best set of parameters: coding rate, modulation order M and modulation shape Γ given the SNR, the PN variance while targeting a PER of 10^{-2} . A PER of 10^{-2} is targeted for numerical evaluations. This quality of service gives reliable transmission with low throughput penalty when automatic repeat request scheme is implemented. It avoids the design of low error floor and reliable FEC scheme. This level of PER is widely considered in modern wireless communication standards [39]. The PN variance $\sigma_\phi^2 = 10^{-1} \text{ rad}^2$ corresponds to an oscillator spectral density K_0 of -100 dB for a bandwidth of 1 GHz. These simulation results emphasize the benefits of using optimized modulation and demodulation schemes to implement high-rate communication systems impaired by PN. In the low SNR regime, the optimized schemes exhibit some performance losses on the achievable rate. These losses result from the high-SNR and strong PN assumptions made to derive the polar metric and to construct the PQAM. These results

Table 2: Comparison of error floors for different constellations and $\sigma_\phi^2 = 10^{-2}$

Constellation	$\text{SEP}_{E_b/N_0 \rightarrow +\infty}$
16-PSK	5.0×10^{-2}
16-QAM	3.5×10^{-4}
Foschini <i>et al.</i> [16]	2.2×10^{-4}
16-PQAM(4)	4.0×10^{-15}
16-PQAM(8)	1.3×10^{-55}
Krishnan <i>et al.</i> [23]	0
16-PQAM(16)	0

confirm that at low SNR, and even with strong PN, conventional modulation schemes such as QAM should be used. Furthermore, it should be mentioned that the probabilistic bit values derived for the PQAM upon the polar metric decision rule present non-uniform protections. With regard to the SNR and PN variance, the bits mapped on the phase and on the amplitude experience different levels of protection. A joint optimization of the modulation and the channel coding (*e.g.* similar to multi-level coding techniques) could exploit the latter property to further enhance the demodulation performance and increase the achievable rate.

4.4.6 Comparative studies

Asymptotic performance

Table 2 presents the asymptotic SEP performance of different constellations from prior work for $\sigma_\phi^2 = 10^{-2}$. This table is extracted from [23] and has been completed with our proposition. The error floors of PQAM have been obtained with the closed form expression. It should be remarked that conventional modulation schemes such as PSK or QAM demonstrate high error floors. In contrast, optimized constellations does not exhibit any error floor. As aforementioned in Sec. ??, the larger the minimum angular distance of a constellation, the lower the error floor. It is hence shown that low error floor communications can be achieved by using a large number of amplitude levels to define the constellation.

State-of-the art constellation

The definition of the Polar-QAM is close to the one of the Gray-APSK, proposed in [47] to provide a shaping gain for satellite communications and not to achieve PN robustness. Both modulation schemes use structured APSK and two independent Gray mapping on the phase and on the amplitude, and hence, demonstrate similar performance. The difference between these constellations is that the amplitudes of Gray-APSK signal points are non-linear. We have proposed the Polar-QAM and derived its analytical and numerical performance analysis in the context of PN channels. For this reason, we compare in this paragraph the performance of the proposed solution to the one of the, most recent, state-of-the-art solution proposed in [2] on constellation optimization for the GPN channel: the *spiral* constellation. Nonetheless, interested readers may refer to [2] which evaluates the performance of the Gray-APSK. Fig. 30 compares the SEP performance of the PQAM and the spiral constellation for $M = 64$ and $\sigma_\phi^2 = 10^{-1}$ demodulated with a polar metric receiver. It is shown that the spiral

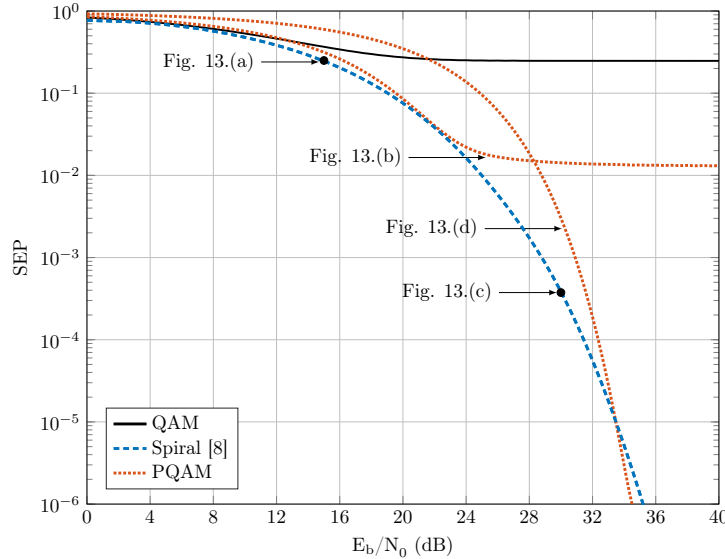


Figure 30: Comparison of PQAM to the spiral constellation [2] with $M = 64$ and $\sigma_\phi^2 = 10^{-1}$

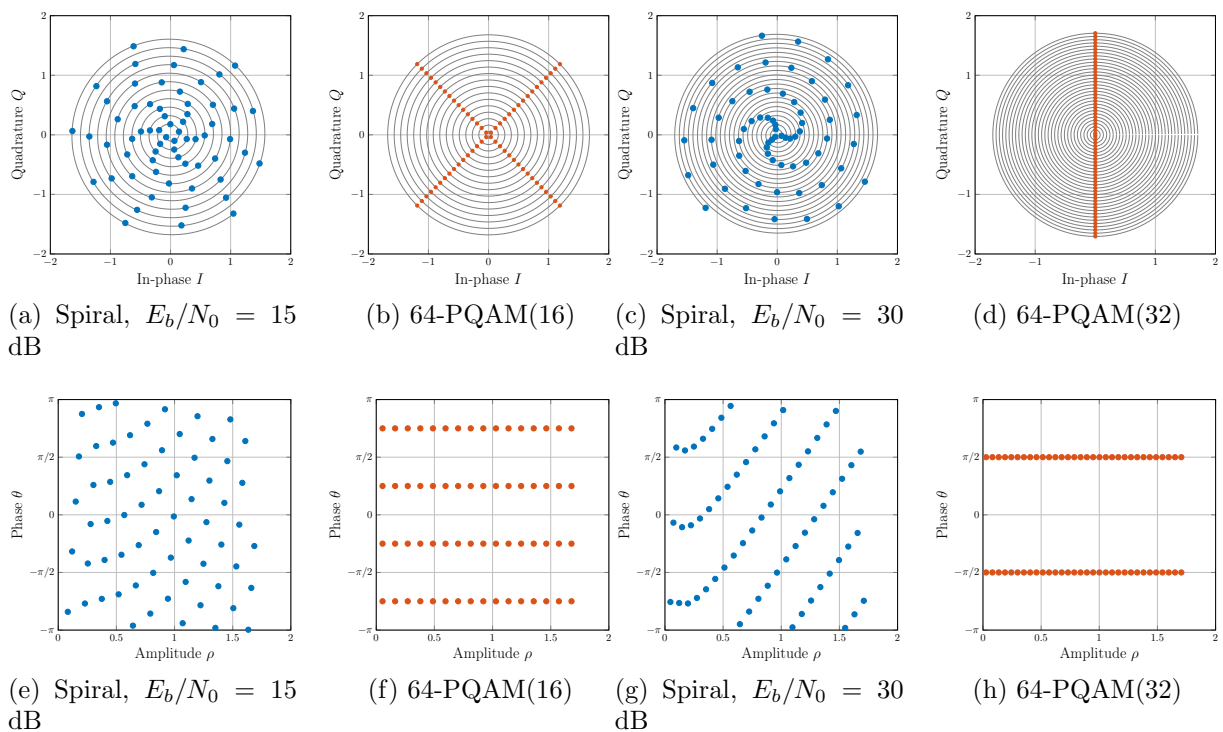


Figure 31: Spiral and PQAM constellations in ℓ^2 (first row) and in p^2 (second row)

constellation demonstrates a performance gain in comparison to the PQAM at the expense of a transceiver complexity increase. The spiral constellation presents a semi-analytical description: the modulation points are defined with a closed-form expression upon an optimized modulation shape parameter $f_s \in \mathbb{R}_{\geq 0}$. For each SNR point, the spiral constellation requires the optimization of the parameter f_s through important Monte-Carlo simulations to maximize the achievable information rate of the modulation. Conversely to this, the modulation shape parameter Γ of the Polar-QAM belongs to a small finite set; and therefore, adapting the modulation scheme to the channel is straightforward. Though a simple and efficient symbol detection rule is proposed in [2], the binary labeling of the spiral constellation entails a complex LLR evaluation which cannot be efficiently approximated. Fig. 30 precisely illustrates the benefits of the proposed solution: near-optimal performance are achieved with a simple implementation. By way of illustration, Fig. 31 presents the Polar-QAM and spiral constellations in the IQ plane and in the amplitude-phase domain. It can be observed on Fig. 31e that the definition of the spiral constellation is actually closed to a hexagonal polar-lattice in the amplitude-phase domain. The Polar-QAM and the spiral constellations demonstrate similar PAPR values. For the spiral constellation optimized for $E_b/N_0 = 30$ dB the PAPR is 4.66 dB while the PAPR of the 64-PQAM(32) is 4.64 dB.

Complexity of implementation

It is clear that numerically optimized constellations, and more generally speaking generalized APSK modulations, are difficult to demodulate due to the complex nature of the Voronoi regions. Conversely, using the proposed Polar-QAM and polar metric detector, the symbol detection can be implemented with a simple Cartesian-to-polar transform followed by an independent component processing with threshold detection. Considering a soft-decision decoding, with a soft-output demapper, the Polar-QAM is even more beneficial. On one hand, non-structured constellations leads to multi-dimensional processing involving all signal points. This leads to a wide literature to reduce decoder complexity, see [51] or [52]. On the other hand, with the Polar-QAM, the commonly used log-sum approximation – *e.g.* widely considered for QAM demapping – can be implemented after the Cartesian-to-polar transform. In addition, the binary labeling and linear structure of the Polar-QAM enables efficient approximations of the bit LLR values with piecewise linear functions, similar to the ones presented in [49] and in [50], and therefore leads to a significant complexity reduction of the decoder. This is a important benefit of using the PQAM and the polar metric. In comparison to state-of-the-art techniques, it offers significant complexity reductions of the receiver.

4.5 Applications & Perspectives

The aim of this Section 4 is to highlight potential applications and perspectives the proposed schemes. First, sub-THz applications based on channel bonding may use non-contiguous bands in a wide frequency range leading to significant differences in the performance of oscillators [26]. Accordingly, we propose a new link adaptation scheme to maintain robustness by setting the Polar-QAM parameters with regard to the SNR and PN variance. Second, the memoryless model of PN may be considered as an optimistic assumption. Therefore, we present a differential version of the PQAM which is more robust to the cumulative PN.

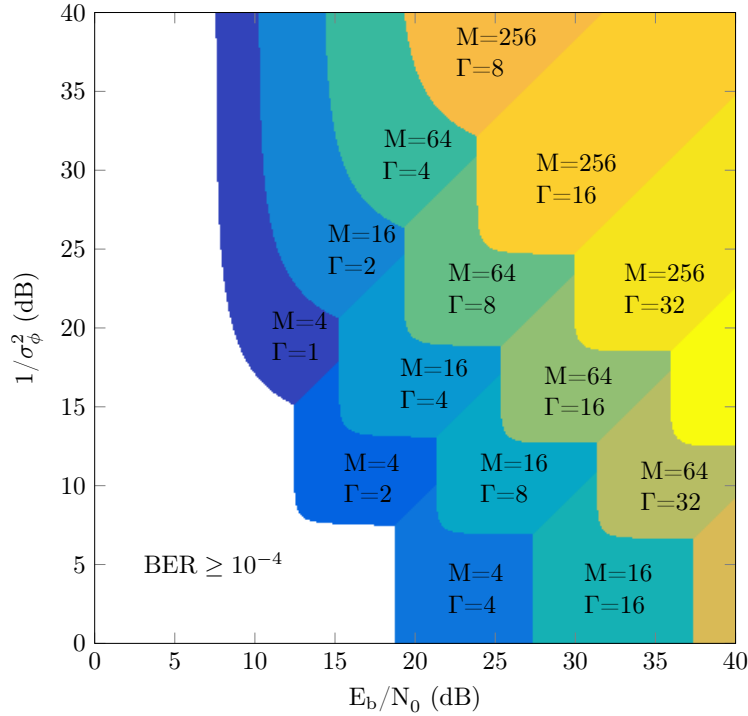


Figure 32: PQAM parameters M and Γ with the highest spectral efficiency such that $\text{BER} < 10^{-4}$

4.5.1 Link adaptation

In order to maximize the spectral efficiency, practical communication systems implement adaptive modulation schemes. Namely, the modulation order is set with regard to the quality of the channel. In particular, a link adaptation scheme is highly valuable for sub-THz communications. Regarding contemplated applications for terrestrial and vehicular networks [53], a base station is to address several users' equipment with different qualities, and thus, different SNR and PN levels. Moreover, for channel bonding systems, the aggregated spectrum may be wide enough to exhibit significant differences between oscillators performance in higher and lower frequencies. In the case of the Polar-QAM, we propose a new link adaptation strategy which is developed beyond adjusting the modulation order M of conventional techniques, by also adapting the modulation shape with parameter Γ . In particular, the introduced theoretical analysis of the performance of the Polar-QAM is valuable for the link adaptation. We can use the analytical expression of the BER in Eq. (55) to determine the best set of parameters (M, Γ) to achieve the highest spectral efficiency while maintaining the BER below a fixed threshold. Fig. 32 presents the PQAM parameters M and Γ for a given PN variance σ_ϕ^2 and E_b/N_0 such that the spectral efficiency is maximized and the BER remains inferior to 10^{-4} . This link adaptation strategy requires a channel estimation scheme which has been previously introduced. It should be emphasized that the Polar-QAM enables a simple link adaption strategy. In contrast to state-of-the-art solutions, the modulation order and shape parameters (M, Γ) belong to small finite sets, and therefore, adapting the modulation scheme to the channel conditions is straightforward.

4.5.2 Beyond memoryless phase noise

The phase shift induced by the propagation channel must be estimated and then corrected. Generally speaking, pilot-based estimation schemes are considered and lead to a spectral efficiency loss. Moreover, the oscillator at the receiver may not be synchronized to the carrier frequency of the transmitter resulting in a carrier frequency offset (CFO). If the CFO is not perfectly estimated and compensated, then a residual frequency synchronization error corrupts received symbols with a cumulative phase error. This phase error is increasing between reference pilots and phase corrections, and thus, can be modeled as cumulative PN. Besides, it has been stated that oscillator PN also demonstrates a cumulative nature. For these reasons, the cumulative PN in certain systems might not be negligible or not perfectly compensated using reference signals. These impairments affecting practical systems lead to performance degradation and motivate the use of a differential modulation. It should be mentioned that the use of differential M -QAM with $M > 4$ is not simple and remains challenging to design. In contrast to conventional solutions or state-of-the-art constellations, the proposed modulation scheme has the advantage of being straightforwardly compatible with a differential scheme. We denote DPQAM the Differential implementation of the PQAM. The information encoded upon the amplitude of symbols remains identical whereas the phase information is encoded in the relative phase difference between two symbols. Subsequently, the DPQAM is not subject to the initial phase shift of the channel. We propose the DPQAM to provide a high-order modulation scheme with an improved robustness to the cumulative PN and residual CFO. The performance analysis of the DPQAM has been pursued but exceeds the scope of this study and is to be released in a further work. Nevertheless, one may refer to our previous work [27] which assessed analytically and numerically the performance degradation due to cumulative PN for phase modulated signals.

4.5.3 Perspectives

We have presented in this section the main transmission schemes to realize robust communications impaired by PN. However, many algorithms regarding practical communications are yet to be addressed. In particular, the synchronization between the transmitter and the receiver in the presence of strong PN is challenging. Time and frequency synchronization errors lead respectively to inter-symbols interference and CFO. Synchronization errors need to be compensated in order to limit the resulting performance degradation. For this reason, dedicated synchronization techniques should be designed for systems impaired by strong PN. This topic is of important practical interest and remains to be investigated. The design of dedicated RF architectures is also interesting to investigate. Since symbols of the Polar-QAM constellation is entirely defined by their phase and amplitude, a conventional IQ transmitter RF architecture may not be relevant and could be replaced by a *polar RF transmitter* – a widely known technique, see [54]. In this Section 4, we have considered an IQ receiver RF chain and have shown that the optimal demodulation uses polar coordinates. It is hence legitimate to contemplate the benefit of a *polar RF receiver* [55] which outputs directly the phase and amplitude of received symbols. Furthermore, it is of practical interest to study the impact of quantization. Contrary to usual IQ schemes in which the quantization strategy is the same on the two signal paths, the use of asymmetric strategies could be relevant for polar RF receivers, especially in the context of a GPN channel. In Section 4, different signal

processing techniques have been discussed to mitigate the performance degradation due to PN. It should also be mentioned that on-going research works are dedicated to the design of sub-THz oscillators with low PN characteristics [1].

4.6 Conclusion

We have investigated the design of robust communications impaired by strong PN for future sub-THz applications. We have developed a pragmatic approach supported by a theoretical framework. This problem has been addressed in three steps: the characterization of the PN channel, the design of receiver algorithms, and the optimization of the modulation scheme. First, we have introduced the system model for sub-THz communication systems. A LoS propagation channel has been considered and the oscillator PN has been described by a Gaussian process. Second, we have addressed the design of the optimum demodulation scheme for the GPN channel. The polar metric has been derived as a symbol detection scheme minimizing the error probability. We have also proposed a low-complexity implementation of the soft-output demapper using the polar metric for probabilistic channel decoding. In contrast to state-of-the-art detectors, the proposed soft-output demapper allows a simple evaluation of soft bit values. Simulation results show that significant demodulation performance gains are achieved by using the polar metric in comparison to standard detectors. Third, we have studied the optimization of the modulation scheme for the GPN channel. A mathematical framework, based on a signal decomposition in polar coordinates, has been presented to design robust constellations and also to evaluate state-of-the-art solutions. It has been shown that a constellation defined upon a lattice in the amplitude-phase domain is robust to PN and leads to a low-complexity implementation. Thereupon, we have proposed the Polar-QAM scheme. The constellation and the binary labeling of the Polar-QAM are jointly designed to enhance the system performance with a low-complexity implementation. We have compared the proposed modulation to conventional and state-of-the-art solutions on different performance metrics such as the PAPR, the BER, or the achievable rate. Our results highlight the important performance gains realized by the Polar-QAM in comparison to conventional schemes. In contrast to state-of-the-art optimized constellations, the advantage of the proposed solution is that near-optimal performance is achieved with significant complexity reductions of the transceiver. To conclude, we have shown in this work that optimizing the communication schemes is essential to realize high rate communications on practical systems impaired by strong PN. Accordingly, the proposed schemes offer valuable low-complexity solutions for future sub-THz systems.

5 MIMO Schemes and waveform design

5.1 Introduction

The wireless data rates have doubled every 18 months over the last three decades. In addition, the wireless data traffic is projected to increase by 1000-fold by the year 2020 [56] and is likely to grow by more than 10 000-fold by the year 2030. Similarly, the required data rates are increasing continuously towards Tb/s.

In addition, the ultra-high data rate wireless communication is an emerging requirements for several scenarios and applications that include transmission distances ranging from the very short (few centimeters or less) to relatively long distances of several kilometers. Some of these use cases such as the Close Proximity P2P applications (Kiosk downloading), Intra-Device Communication, Wireless Fronthaul/Backhaul and Data Centers (described by the IEEE Standards Association of IEEE 802.15 WPAN [57] in the band between 250-325GHz, the IEEE 802.11ad [58], and IEEE 802.15.3e [59] in the 60GHz). Moreover, several researchers tried to reach a high data rate but the maximum achieved, to the best of our knowledge, was below 70Gb/s due to hardware and technology limitation in the D-band [60]. Thus, additional breakthrough technologies are necessary to reach the Beyond 5G throughput requirements.

Dense small-cell deployments, centralized Radio Access Network (RAN), advanced MIMO schemes and new mm-Wave bands are key enablers to achieve the expected increase in spectral efficiency and capacity [61]. For this reason, our research in BRAVE project is focused on the mm-Wave and sub-THz band within the range 90GHz-200GHz where a huge bandwidth can be allocated (up to 50GHz aggregated bandwidth) to reach 1Tb/s (100x peak data rate defined in IMT-2020 for 5G) [26]. Also, other researchers are investigating the feasibility of wireless communication at higher frequencies on the true THz band (0.1-10 THz) where a huge contiguous bandwidth is available [62], [63].

In the last decade, the methodology used to enhance the rate was based on increasing the order of M -ary QAM and the size of antenna array for MIMO spatial multiplexing. However, designing similar systems for Tb/s requires an extremely large signal to noise ratio to ensure good performance. In addition, it suffers from large power consumption by power amplifiers (PAs) due to high peak to average power ratio (PAPR) of larger M -ary QAM.

In order to reach this ultra-high data rate, it is important to develop a new wireless communication methodology that achieve a high spectral efficiency with a given power expenditure. For this reason, our methodology investigates the Single-Carrier (SC) waveform which is enabled by [64]:

- The high power efficiency due to lower PAPR compared to multi-carrier (MC) waveform. MC suffers in nature from high PAPR which leads to intensive energy consumption by the PAs and hence negatively influence out-of-band emissions.
- The availability of frequency-flat channels and especially when the large occupied bandwidth is achieved by aggregation of small channels. Note that the propagation above-90 GHz is often characterized by a dominant path [65], obtained either from LoS situation or antenna beam alignment.

Moreover, we propose to benefit from index modulation (IM) and advanced MIMO schemes to enhance the spectral efficiency of the power efficient SC modulation. Note that

IM has attracted tremendous attention and it is explored separately and jointly in the spatial, frequency, and temporal domain in the last decades [66]. In addition, these IM techniques convey additional information bits contained implicitly in the index of the selected element among several possible combinations. As example, the element could be the antenna set as generalized spatial modulation [67] [68], sub-carrier group in MC waveform as OFDM-IM [69], or frequency bands and dispersion matrix in space-time domain as Space-Time-Frequency Shift Keying (STFSK) [70].

In this document, we propose a new methodology based on constant or near-constant envelope single modulation modulation with IM (SC-IM) to reach Tb/s with a low power consumption. In addition, its feasibility is evaluated depending on error performance, power consumption, complexity and cost. The performance analysis of the proposed SC-IM is addressed over spatially correlated/uncorrelated Rician and Rayleigh channels. Moreover, the link budget is calculated and the power consumption is estimated to emphasize the importance of SC-IM for Tb/s. Finally, the advantage of SC-IM in mm-Wave and sub-THz bands is presented. The notations adopted are as follows. We use capital bold \mathbf{X} for matrices. $(\cdot)^T$ and $(\cdot)^H$ are used to denote respectively the transpose and the Hermitian transpose of a matrix. $(\cdot)^\dagger$ denotes the pseudo inverse of a matrix. $\mathbf{X}_{m,n}$ denotes a matrix with row index m and column index n . \mathbf{I}_N denotes the $N \times N$ identity matrix. \otimes stands for the Kronecker product. $\binom{n}{k}$ denotes the binomial coefficient. $\mathcal{CN}(\mu, \sigma^2)$ denotes the complex normal distribution of a random variable having mean μ and variance σ^2 . $\lfloor \cdot \rfloor$ denotes the floor function. $\|\cdot\|$ stands for the Frobenius norm.

5.2 Generalized Spatial Modulation (GSM) MIMO System

5.2.1 System and Channel Models

The proposed system model is based on the Generalized Spatial Modulation (GSM) MIMO system with N_t transmit antennas and N_r receive antennas. In this system, the source binary information sequence b is divided into two streams b_1 and b_2 as shown in Fig. 33. The bit-stream b_1 is mapped by the N_a M -ary Amplitude-Phase Modulators (APM) such as QAM, PSK, CPM, etc. The bit-stream b_2 is encapsulated in the index of the selected Transmit Antenna Set (TAS) at each symbol period, where each TAS is formed of N_a activated transmit antenna (TA) out of N_t .

The possible number of TAS with N_a activated antennas is the combination $\Omega = \binom{N_t}{N_a}$.

However, only $\mathcal{L} = 2^{\lfloor \log_2(\Omega) \rfloor}$ are used to keep the bits length of b_2 an integer number and the other possibility are marked as illegal combinations. Note that the appropriate TASs should be carefully selected from the Ω possibilities to minimize the interference and the effect of spatial correlation between antennas. Accordingly, the number of bits per GSM symbol can be expressed as:

$$b = \lfloor \log_2(\Omega) \rfloor + N_a \cdot \log_2(M) \quad (58)$$

The GSM transmitted symbol vector $x = [x_1, \dots, x_{N_t}]^T$ contains only ' N_a ' APM symbols at the positions in the selected TAS according to b_2 . Note that the inter-antenna synchronization at the transmitter is required to make sure that the receiver can detect the activated

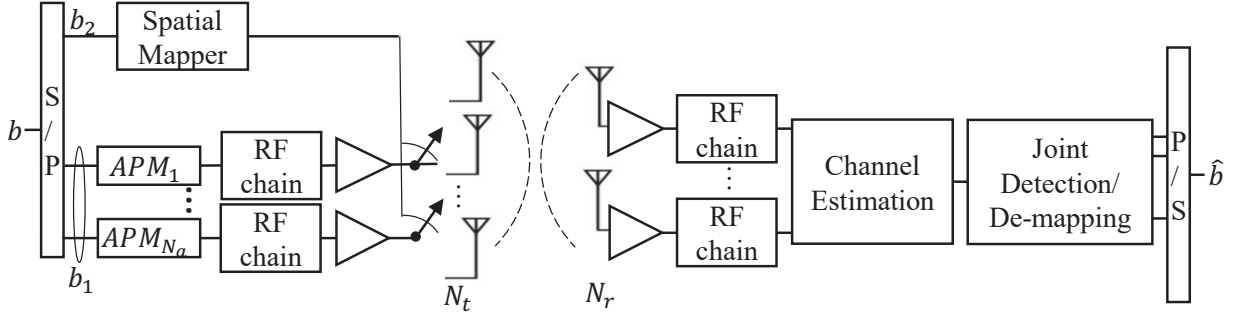


Figure 33: System Model

antenna from each received vector y . The received signal y is expressed as:

$$y = \mathbf{H}x + v \quad (59)$$

where \mathbf{H} is the $N_r \times N_t$ channel matrix, the power of transmit symbols is normalized, v is $N_r \times 1$ channel noise vector and its elements v_r obeys the independent and identically distributed (i.i.d.) additive white Gaussian noise (AWGN) with the variance of σ_v^2 , i.e., $\mathcal{CN}(0, \sigma_v^2)$ for $r = 1, \dots, N_r$.

At the receiver side, the index of selected TAS and the modulated symbols on all activated transmit antennas can be detected jointly by the ML detector that perform exhaustive search over all the possible transmit vector described as

$$\hat{x} = \arg \min_{x \in \chi} \|y - \mathbf{H}x\|^2 \quad (60)$$

where χ denotes the set of all possible transmit vectors in both the spatial and signal constellation domains and \hat{x} is the estimated transmit vector with N_a non zero elements in the position of the activated transmit antennas.

However, a GSM symbol detection with lower complexity is possible by ordered block minimum mean-squared error (OB-MMSE) that achieves near-ML performance [71]. The OB-MMSE detector reduces the iterations of search algorithm by ordering the appropriate TAS and stop the search when $\|y - \mathbf{H}\hat{s}\|^2$ becomes less than a predefined threshold $V_{th} = 2N_r\sigma^2$, where \hat{s} is the MMSE equalized symbol and quantized to an APM symbol. For instance, the sorted TASs are denoted by $\{I_1, I_2, \dots, I_{\mathcal{L}}\}$ where each I_i represents a vector with the indices of the N_a possible activated TA. Their descending order sorting is based on their weighting factor w_i that measures the reliability of each TAS I_i defined as

$$z_t = (h_t)^\dagger y \quad (61)$$

$$w_i = \sum_{n=1}^{N_a} z_{i_n}^2 \quad (62)$$

where $(h_t)^\dagger = \frac{h_t^H}{h_t^H h_t}$ is the pseudo inverse of the t^{th} column of channel matrix \mathbf{H} with $t = 1, \dots, N_t$. Thus z_{i_n} represents the element from $z = [z_1, z_2, \dots, z_{N_t}]$ at the n^{th} activated TA according to TAS I_i where $i = 1, \dots, \mathcal{L}$.

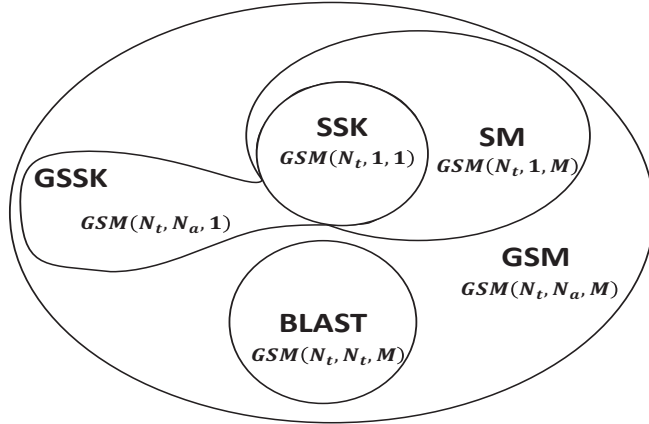


Figure 34: GSM Derivatives

Then, the symbol vector is estimated by a simplified block based MMSE equalizer

$$\hat{s}_i = \mathcal{Q} \left(\left((\mathbf{H}_{I_i})^H (\mathbf{H}_{I_i}) + \sigma_v^2 \mathbf{I}_{N_a} \right)^{-1} (\mathbf{H}_{I_i})^H y \right) \quad (63)$$

where \mathcal{Q} represents the quantization operation that restricts \hat{s}_i to be a value from the APM constellation set \mathcal{S} and the $N_r \times N_a$ matrix \mathbf{H}_{I_i} is a sub-matrix with all columns of \mathbf{H} corresponding to the antenna indices in TAS I_i . Thus, the reduced computational complexity of OB-MMSE detector can be expressed in terms of real floating point operations according to [71] as following

$$\begin{aligned} Complexity_{OB-MMSE} &= (14N_rN_t + 3N_t + N.N_a)/\mathcal{L} \\ &+ (12N_rN_a^2 + 11N_rN_a + 6N_r - 6N_a^2)p_{avg}/\mathcal{L} \end{aligned} \quad (64)$$

where p_{avg} represents the average number of the block MMSE detections in Eq. (63).

The adopted notation for this system is $GSM(N_t, N_a, M)$ where the parameter M is the APM M -ary size, $M = 2^p$ with $p \geq 0$. Note that $p = 0$ means that the transmitted symbols are just a constant power value to simplify the receiver detection at the expense of lower data rate. Furthermore, it worth mentioning that GSM includes other spatial modulation techniques such as the Spatial Modulation (SM) $GSM(N_t, 1, M)$ [72], Space-Shift Keying (SSK) $GSM(N_t, 1, 1)$ [73], Generalized SSK (GSSK) $GSM(N_t, N_a, 1)$ [74] and conventional MIMO spatial multiplexing defined by Bell Laboratories Layered Space-Time (BLAST scheme) $GSM(N_t, N_t, M)$ as shown in Fig. 34. This feature can be utilized to have a reconfigurable architecture with different data rates and receiver complexity.

5.2.2 Channel Model

In this Section, we consider a slow fading MIMO channel matrix \mathbf{H} as a Rayleigh or Rician multipath fading channel with/without spatial correlation defined as

$$\mathbf{H} = \sqrt{\frac{K}{K+1}} \mathbf{H}_{LoS} + \sqrt{\frac{1}{K+1}} \boldsymbol{\Sigma}_r^{\frac{1}{2}} \mathbf{H}_{NLoS} \boldsymbol{\Sigma}_t^{\frac{1}{2}T} \quad (65)$$

where K is the Rician factor, \mathbf{H}_{LoS} and \mathbf{H}_{NLoS} are the $N_r \times N_t$ line of sight (LoS) and the non-LoS channel matrix respectively. The \mathbf{H}_{NLoS} can be considered as a Rayleigh channel whose elements satisfies $\mathcal{CN}(0, 1)$. In addition, the NLoS part exhibits a spatial correlation described by Kronecker model that assumes the spatial correlations at the transmit and receive sides are separable. This model approximates the correlation matrix Σ as the Kronecker product of the correlation matrices at transmitter and receiver, denoted as Σ_t , and Σ_r , respectively:

$$\Sigma = \Sigma_t \otimes \Sigma_r \quad (66)$$

Thus, Eq. (85) includes the uncorrelated/correlated Rayleigh and Rician fading channel as special case depending on the value of K and the correlation matrices.

5.2.3 Performance analysis

In this section, firstly we compare MIMO spatial multiplexing (BLAST) with GSM to prove that the latter is able to reduce the number of required RF chains as depicted in Fig. 35 for a given system spectral efficiency. For fair comparison, the target system spectral efficiency for BLAST and GSM systems in Fig. 35 is maintained in the order of 25 b/s/Hz with $N_t \leq 32$. In other words, the system spectral efficiency for both systems (BLAST and GSM) with any APM spectral efficiency (0.8 – 10 b/s/Hz) is in the order of 25 b/s/Hz. It is clear that the number of RF chains with BLAST is always the largest and it is more than the double of that of GSM when the APM spectral efficiency is low (up to 3b/s/Hz). This reduction leads to a lower detector complexity for GSM compared to BLAST. However, these advantages of GSM are at the price of higher number of transmit antennas which is feasible for example for downlink scenario as Kiosk downloading at mm-Wave and sub-THz bands.

In the following, we present the numerical comparison between several APM-GSM systems that employs different APM schemes:PSK, DPSK, CPM and QAM. The bit error rate (BER) of these systems in function of the average SNR was evaluated using Monte Carlo Simulations. In order to conduct a fair comparison, same transmission rate has been used without restriction on the constellation size and the number of antennas.

In fact, the $\text{GSM}(N_t, N_a, M)$ parameters for Tb/s are chosen such that the required number of RF chains is minimized to reduce the cost with a maximum allowed $N_t \leq 22$ and a given M -ary APM. In addition, the adopted GSM detector in these systems is OB-MMSE that is able to jointly detect the TAS and the APM constellations with a balanced trade-off between system performance and complexity. The simulations are performed over correlated/uncorrelated Rayleigh and Rician channels with different correlation levels. The correlation matrices in the Kronecker model are formed according to the exponential model of [75] where the elements of transmit Σ_t and receive Σ_r correlation matrices are affected by fixed correlation factor β : $[\Sigma_t]_{m,n} = \beta_t^{|m-n|}$. We used $\Sigma_r = I_{N_r}$ to concentrate on the impact of correlation at the transmitter side where a larger antenna array is used to convey the data in the spatial domain of index modulation.

The simulation parameters for the different systems that can achieve Tb/s are summarized in Table 3. The CPM parameters used with CPM-GSM system are: modulation index $h = \frac{1}{3}$, raised cosine as frequency pulse with length $L = 3$ symbol intervals.

Fig. 36 shows the performance of different systems over uncorrelated Rayleigh channel. As we remark, systems with more data conveyed by IM with small M -ary size as (D)QPSK-GSM and CPM-GSM have better performance than those with a lower number of antennas

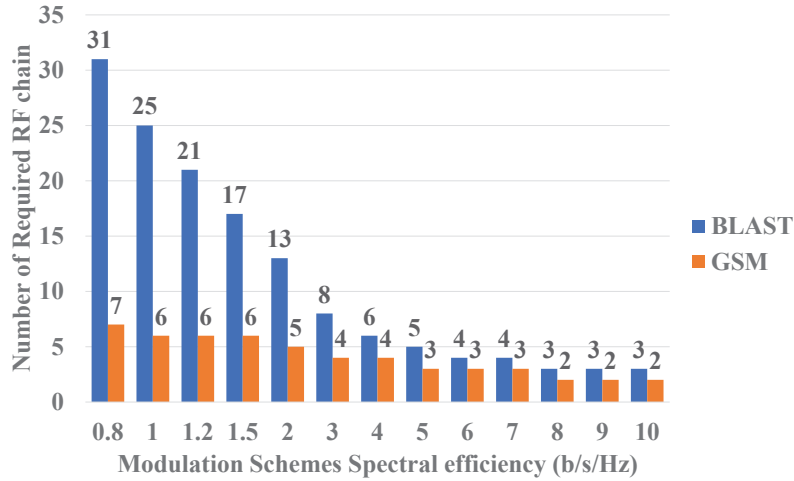


Figure 35: Minimum number of required RF chains for GSM and BLAST systems as function of APM spectral efficiency. The system spectral efficiency for both systems (BLAST and GSM) with any APM spectral efficiency (0.8 – 10 b/s/Hz) is in the order of 25 b/s/Hz.

Table 3: Simulation parameters

Parameters	Value
CPM-GSM	GSM(22, 6, 4)
QPSK-GSM	GSM(17, 6, 4)
DQPSK-GSM	GSM(17, 6, 4)
16QAM-GSM	GSM(13, 4, 16)
64QAM-GSM	GSM(11, 3, 64)
256QAM-GSM	GSM(24, 2, 256)
N_r	$2N_a$
Rician factor K	[0, 3]
Oversampling factor	2
Raised Cosine Rolloff α	0.2
Correlation factor β_t	[0, 0.2, 0.5, 0.8]
Number of GSM symbols	10^4

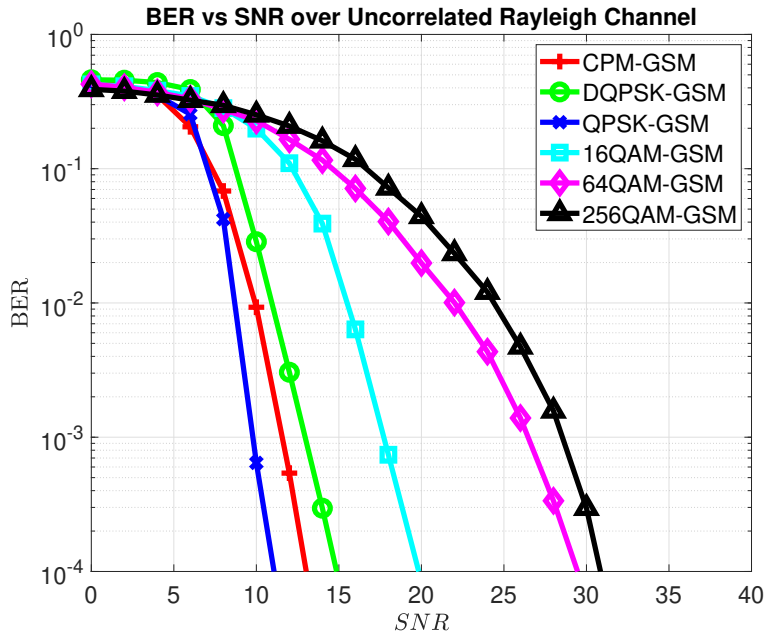


Figure 36: BER vs SNR for various systems over uncorrelated Rayleigh channel

but with higher M -ary size $M \geq 16$. Therefore, the total BER is affected by the order of APM being used more than the order of index modulation. In other words, the larger N_t and lower M -ary APM are, the better the performance is. But increasing N_t increases the computational complexity of the detector.

The same systems are evaluated over uncorrelated Rician channel and the simulation results are shown in Fig. 37. However, the required SNR in this channel is higher than that in Rayleigh channel for same BER. It is worth mentioning that CPM-GSM have a notable degradation in the Rician channel about 10 dB and this system requires additional 2 dB compared to DQPSK-GSM while it was completely the inverse in Rayleigh channel.

CPM-GSM and (D)QPSK-GSM are compared in Fig. 38 and 39 with different correlation levels $\beta_t = [0.2, 0.5, 0.8]$ over Rayleigh and Rician channels respectively. These results show that these systems conserve their good performance with low spatial correlation while they start to degrade at high correlation levels. In particular, (D)QPSK-GSM performance is reduced by less than 1 dB at un-coded $\text{BER} = 10^{-4}$ when the correlation increases to $\beta_t = 0.5$ as shown in Fig. 38 and 39. Also, their performance degrades by approximately 5 dB at high correlation level $\beta_t = 0.8$, while CPM-GSM is more sensitive to correlation and degrades by 6 – 8 dB.

Furthermore, the spatial correlation that is larger at high frequencies with uniform planar array [76] affects the performance of any spatial modulation with multiple active transmit antennas. However, its effect can be reduced by carefully choosing the appropriate TAS and their elements.

In reality, a perfect channel estimation can not be guaranteed and the results in [77] show that the channel estimation error degrades rapidly the performance of large M -ary QAM ($M = 16$) and creates an error floor at $\text{BER} = 10^{-5}$ or higher while its effect on low M -ary as QPSK is less important and the error floor is as low as $\text{BER} = 10^{-7}$. Thus, these low M -ary APM which have near-constant or constant envelope are more robust to channel estimation

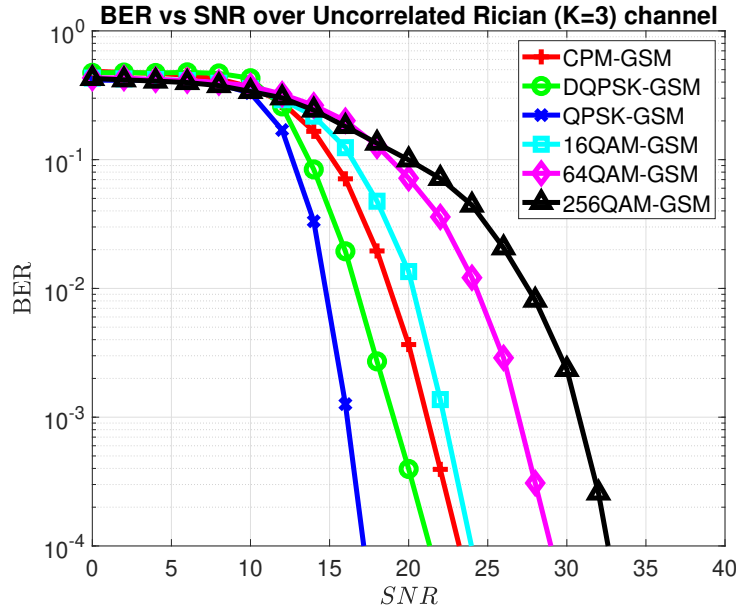


Figure 37: BER vs SNR for various systems over uncorrelated Ricain channel

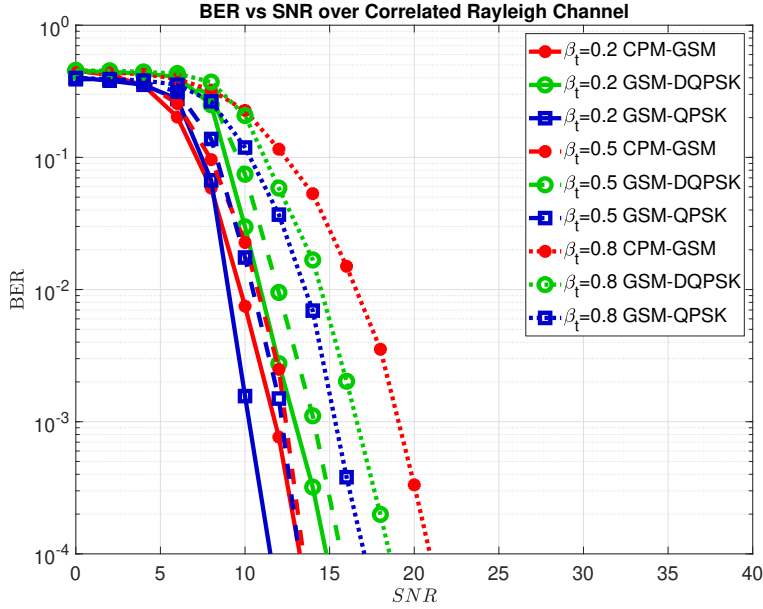


Figure 38: BER vs SNR for (D)QPSK-GSM and CPM-GSM over correlated Rayleigh channel

errors.

5.2.4 Link budget and discussion

In this section, the link budget is calculated for all systems for same un-coded BER 10^{-4} with correlated/uncorrelated Rayleigh and Rician channels. Then, their power consumption for an ultra-high data rate is deduced. For a fair comparison, these systems are configured

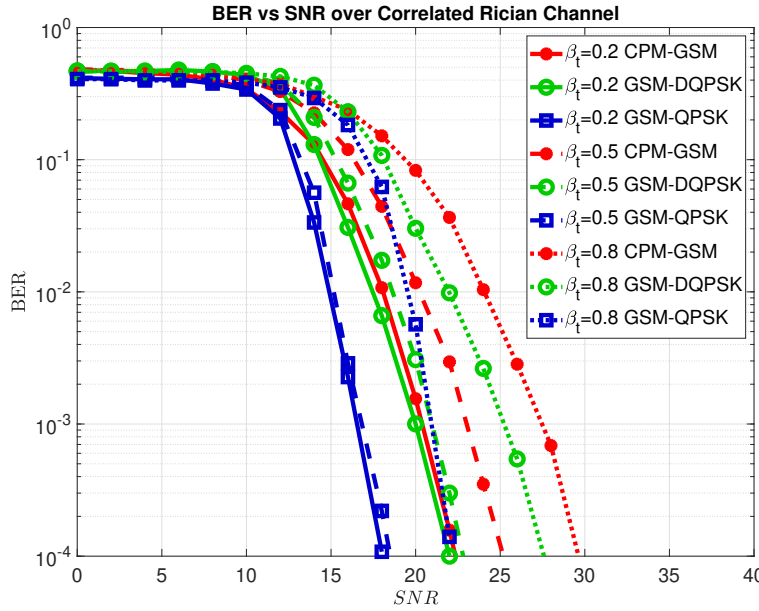


Figure 39: BER vs SNR for (D)QPSK-GSM and CPM-GSM over correlated Rician channel

for same spectral efficiency that is defined as:

$$SE_{GSM} = \frac{BitRate_{(bits/s)}}{W(Hz)} = \frac{R_{(Symbol/s)} * b_{(bits/symbol)}}{W(Hz)} \quad (67)$$

where R is the symbol rate and W is the allocated bandwidth. Since the non-linear modulation as CPM requires a larger bandwidth, its symbol rate is adjusted accordingly to keep the same occupied bandwidth among all systems. Thus, the number of bits per GSM symbol must be higher with CPM as shown in Table 4.

Henceforth, we consider a close proximity scenarios (as Downlink kiosk) with distance $d=5m$ and channel bandwidth $W=1GHz$ with channel aggregation/bounding. Note that the available spectrum is 49.65GHz in the frequency range between 92 GHz and 175 GHz according to [26] and 50GHz contiguous spectrum between 275-325 GHz [78].

Note that the receivers in this scenario are low cost mobile devices that have small antenna gain. However, this gain is higher when considering longer distances with other scenario as Wireless Backhaul.

In Table 4, the required transmit power P_t with small distance communication is calculated from the required SNR according to the following parameters:

$N_{Thermal}$	$= 10 \log_{10}(k.T.W) + 30$	dBm
N_{Floor}	$= N_{Figure} + N_{Thermal}$	dBm
Rx_{Level}	$= SNR + N_{Floor}$	dBm
$fspl$	$= 20 \log_{10}\left(\frac{4\pi d f_c}{c}\right)$	dB
$T_{PathLoss}$	$= fspl + Attenuation$	dB
$EIRP$	$= T_{PathLoss} - G_r + L_{crx} + Rx_{Level}$	dBm
P_t	$= EIRP - G_t + L_{ctx}$	dBm

where k , T , N_{Figure} , $fspl$, f_c , c , G_r/G_t , L_{crx}/L_{ctx} and $EIRP$ are Boltzmann constant, the temperature in kelvin, the noise figure, the free space path loss, the carrier frequency, the

speed of light in vacuum ($c = 3 \times 10^8 \text{ m/s}$), receive/transmit antenna gain, receiver/transmitter cable loss, the effective isotropic radiated power respectively.

Furthermore, the power consumption is deduced based on the power amplifier efficiency which is affected by the APM PAPR. Consequently, the constant and near-constant envelope modulations combined with GSM prove their ability to reach a high throughput of 1 Tb/s. Also, they conserve their low power consumption as shown in Table 4 that is limited to few Watts while large M -ary APM-GSM requires more 15 – 20 dB. In addition, it is worth mentioning that CPM-GSM have the lowest power consumption in Rayleigh channel but this behavior changes with the spatial correlation effect or in Rician channel due to its performance degradation. Therefore, QPSK-GSM system becomes the least power consuming system. Whereas the DPQSK-GSM system requires more power compared to CPM-GSM and QPSK-GSM, but it is more robust to phase noise that is an important impairment in the sub-THz bands.

The high M -ary APM-GSM systems exceeds the maximum allowed EIRP limitations 40 dBm, even the 16QAM requires 11 dBm as transmit power which is greater than the actual transmit power ($P_t < 10 \text{ dBm}$) at the THz frequencies with current technologies. For this reason, the power consumption for large M -ary schemes ($M \geq 16$) are omitted with correlated Rayleigh and Rician channel.

Moreover, a high M -ary schemes also require a power-hungry analog to digital and digital to analog converters (ADC/DAC) with a large resolution. While the low order modulation schemes allow the usage of few bits (1 – 3 bits ADC) that is a critical requirements to allow higher speed ADC for a larger bandwidth with a low cost. Therefore, the high M -ary APM-GSM systems are not suitable for high data rate in the order of Tb/s with power constraint.

However, the advantages of the CPM-GSM and (D)QPSK-GSM systems come with an increase of the detector complexity and the number of transmit antennas compared to high order modulation with GSM. Note that these computational complexities and the required number of antennas with GSM are less than those with MIMO spatial multiplexing (BLAST) combined with same APM for similar system spectral efficiency. Another advantage of QPSK system is the ability to perform the demodulation in the analog domain that reduces the required converters resolution [79], where they implement a multi-Gb/s analog synchronous QPSK demodulator with phase-noise suppression.

Finally, any system requires a higher SNR in a more severe channels but the analog or hybrid beam-forming gain can keep the systems shown in Fig. 40 feasible in terms of energy consumption. This feature is enabled by massive MIMO where the number of transmit antennas can be increased by replacing each antenna element in TAS by a small antenna array that performs analog beam-forming as proposed in [80] without increasing the number of RF chains at transmitter nor at the receiver side. Therefore, these constant and near-constant envelope with beamforming aided GSM are very appealing for an ultra-high data rates especially for a Tb/s downlink Kiosk sceanrio, where the power consumption and cost of the receiver of the mobile devices are the most critical constraints.

In brief, the comparison of these APM-GSM systems from different point of view is illustrated in Fig. 40 and it shows that the power efficient (D)QPSK-GSM systems are a balanced trade-off between system performance/power efficiency and hardware cost/detector computational complexity.

Table 4: Link Budget and Power Consumption for different GSM parameters achieving Tb/s

Parameters	Temperature (degree C)	20	Carrier Frequency (GHz)	150	Distance (m)		5
	99% of Channel Bandwidth (GHz)	1	Number of Channel Aggregation/bounding		44	Total Bandwidth (GHz) [8]	44
	Modulation	CPM	$\pi/4\text{-QPSK}$	$\pi/4\text{-DQPSK}$	16-QAM	64-QAM	256-QAM
	GSM (Nt,Na)	(22,6)	(17,6)	(17,6)	(13,6)	(11,3)	(4,3)
	Bits per GSM symbol	28.00	25.00	25.00	25.00	25.00	26.00
	Symbol Rate (R)	0.80	0.92	0.91	0.91	0.92	0.91
	Rate	APM Spectral Efficiency	1.59	1.83	1.82	3.65	5.49
Receiver	GSM Spectral Efficiency	22.26	22.90	22.80	22.83	22.88	23.71
	Total Throughput	979.4	1007.6	1003.2	1004.3	1006.5	1043.328
	SNR with Rayleigh	13.00	12.00	15.00	20.00	29.00	31.00
	RX Noise Figure (NF)	10.00					dB
	Thermal Noise (Nthermal)	-83.93					dBm
	Noise floor	-73.93					dBm
	Rx Signal Level	-60.93	-61.93	-58.93	-53.93	-44.93	-42.93
Channel	RX Cable Loss (Lcrx)	1					dB
	RX Antenna Gain (Gr)	3					dBi
	Free space path loss (fspl)	89.94					dB
	Vapour attenuation	1.28					dB/Km
Transmitter	O2 attenuation	0.01					dB/Km
	Rain attenuaton	11.78					dB/Km
	Total Path loss	90.01					dB
	Required Tx EIRP	27.08	26.08	29.08	34.08	43.08	45.08
PAPR	Cable Loss (Lctx)	1					dB
	TX Antenna Gain (Gt)	24					dBi
	Required Pt	4.08	3.08	6.08	11.08	20.08	22.08
Uncorrelated	PAPR for ($\alpha=0.2$)	0	3.8	4.86	7.5	8.2	8.35
	Theoretical PA Efficiency	0.8	0.52	0.44	0.34	0.3	0.28
	Power per Channel	3.20	3.91	9.21	37.70	339.40	576.34
	Total Power Consumption	0.14	0.17	0.41	1.66	14.93	25.36
Correlated	SNR with Rician K=3	23.00	17.00	21.00	24.00	29.00	31.00
	Total Power Consumption	31.48	27.35	32.08	36.20	41.74	44.04
	SNR with Rayleigh $\beta=0.8$	21.00	17.00	18.00	dB		
	Total Power Consumption	29.48	27.35	29.08			
	SNR with Rician $\beta=0.8$	29.00	22.00	27.00	dB		
	Total Power Consumption	37.48	32.35	38.08			

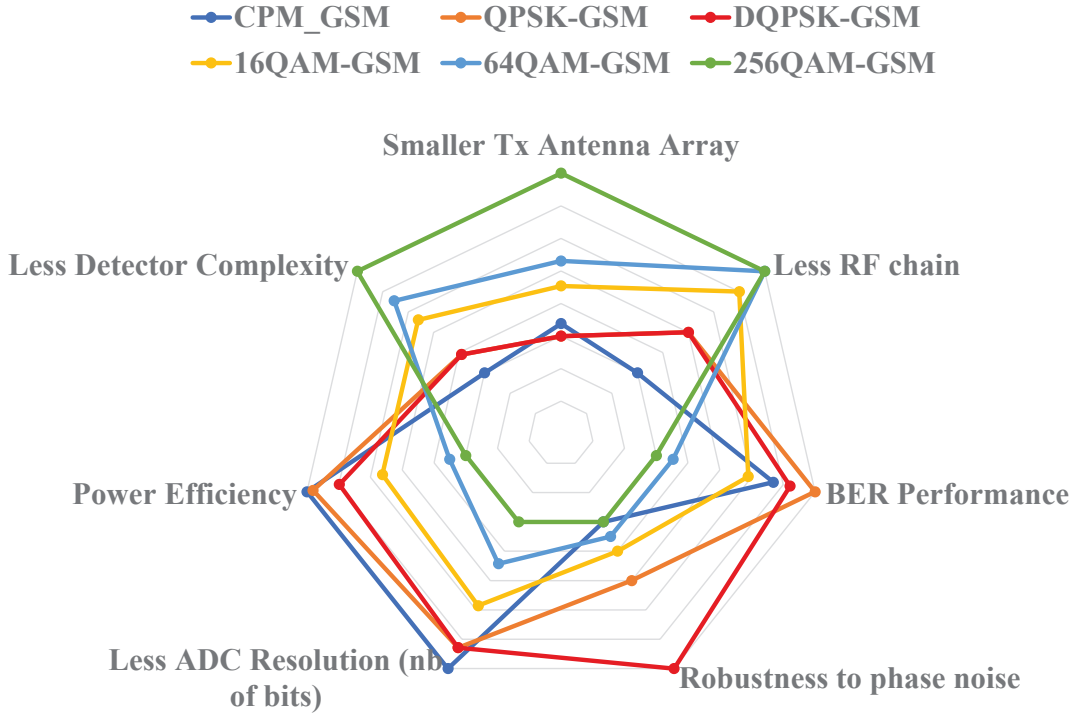


Figure 40: System comparison between different SC modulations with GSM for achieving a Tb/s (see Table 4)

5.2.5 General conclusions

The current methodology for high data rate wireless communication as used in 5GNR is based on increasing the MIMO spatial multiplexing order and M -ary schemes, but it requires a great effort to reduce the PAPR for limiting the power consumption. This methodology is not a convenient solution for ultra high data rate in the order of Tb/s in the 90GHz-200GHz band especially for low cost implementation where the efficiency and the achievable output power decreases at higher frequencies with current technology. Thus, this Section 5 proposes a novel methodology to reach the ultra-high data rates in the order of Tb/s with low power consumption. It is based on using power efficient modulation like constant or near-constant envelope modulation (CPM and (D)QPSK) with GSM or any index modulation that can increase the system spectral efficiency and conserve the power efficiency. The results show that QPSK-GSM(17,6,4) requires 19dB less than 256QAM-GSM(4,3,256) for same spectral efficiency in Rayleigh channel. Therefore, conveying more data by index modulation have a better performance than reducing the number of antennas and increasing the constellation size to attain same system spectral efficiency. Moreover, the link budget and power consumption is estimated for short distance communication e.g. Downlink Kiosk with Tb/s data rate and a 44GHz bandwidth (available at 90GHz-175GHz band [26]). These estimations prove that with the proposed methodology for Tb/s throughput, less than 1 Watt (21 – 26 dBm) is sufficient for (D)QPSK-GSM and CPM-GSM in Rayleigh channel and few Watts (32 – 38 dBm) are more than enough even in highly correlated Rician channel ($\beta_t = 0.8$). Note that QPSK-GSM have the lowest power consumption (27 – 32 dBm) in highly correlated channel

due to its better performance while DQPSK-GSM consumes slightly more power and provides a robustness to phase noise which is an important impairments at sub-THz bands.

In conclusion, the proposed scheme proves that the constant or near-constant envelope modulation CPM-GSM and (D)QPSK-GSM systems with limited number of RF chains, feasible antenna array size and acceptable complexity are able to reach a high system spectral efficiency $\approx 25\text{b/s/Hz}$ and hence ultra-high data rates while maintaining a low power consumption. Furthermore, this methodology allows the usage of low resolution ADC with low power and cost as required for sub-THz communication. Finally, the work presented in this Section 5 prove the feasibility of the proposed methodology from different point of view as performance, spectral/power efficiency, complexity and cost.

5.3 Generalized Spatial Modulation in Highly Correlated Channels

In conventional GSM, the cardinality of the legitimate TAC set is a power of 2 ($2^{\lfloor \log_2(C_{N_t}^{N_a}) \rfloor}$), where the TACs are randomly selected among the possible TACs, whose number is equal to $C_{N_t}^{N_a}$, where N_t and N_a are the number of transmit antenna (TA) and active TA respectively. In addition, the spatial bits mapping was just a binary coding for the index of activated TAC.

Unlike the redesigned spatial modulation in [81] where they try to enhance the performance of Spatial Modulation (SM) in correlated channel by activating a second antenna to benefit from transmit diversity when the most correlated TA is selected. In this Subsection 5.3, we focus on the performance enhancement of GSM systems in highly correlated channels by proposing a general methods for efficient TAC selection and Index-to-Bit mapping. In this context, we designed a TAC selection method based only on the transmit spatial correlation, which is quasi-constant for a specific transmitter (Tx), and does not require the instantaneous CSI estimation at the Tx side or its feedback. The aim of the TAC selection is to reduce the errors in TAC detection because this error will propagate to M-ary symbols. In such a case, the erroneous detection of M -ary symbols is due to the fact that the receiver (Rx) is trying to detect the symbols on the non-activated TAs since the TAC is wrongly detected. Moreover, we proposed a spatial bit mapping based on Gray coding in order to reduce the spatial BER. This mapping is trying to reduce the number of different bits between the neighbor TACs that are most susceptible to be interchanged in highly correlated channels.

5.3.1 Channel Model

In subsection, the Kronecker channel model is used to represent the spatial correlation between antennas. Thus, the Rayleigh and Rician MIMO channels with/without spatial correlation are represented as in (85). The \mathbf{H}_{NLoS} can be considered as a Rayleigh channel matrix whose elements satisfies $\mathcal{CN}(0, 1)$. In addition, the Kronecker model assumes that the spatial correlations at the Tx side Σ_t and the Rx side Σ_r are separable.

5.3.2 Transmit Antenna Combination Selection

The GSM system has N_a TAs activated out of N_t TAs, and only $N = 2^{\lfloor \log_2 N_{all} \rfloor}$ TACs among N_{all} possible TACs will be used to encode the spatial bits. Firstly, the conventional GSM system was used with random selection of N TACs out of N_{all} , then TAC selections

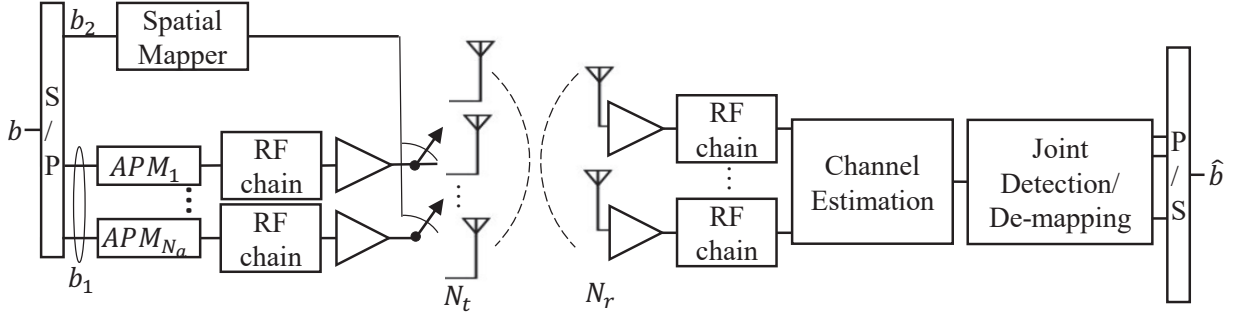


Figure 41: System model of GSM with TAC selection

with/without CSI were introduced in [82]. The objective of TAC selection is to select the optimal legitimate TAC set that permits to reduce the TAC detection errors.

In this section, we will propose a TAC selection method without instantaneous CSI for highly correlated channels, and a comparative study with the existing methods will be provided.

5.3.3 GSM System Relying on Channel State Information (EGSM)

The Enhanced GSM system (EGSM) is an adaptive technique proposed in [82] where it uses the instantaneous channel side information as shown in Fig. 41 to select the optimal legitimate TAC set instead of random TAC selection.

This selection is updated continuously on real time to take into consideration the channel variation, then the transceiver share between them the legitimate TAC set through a feedback channel. This method is based on computing the Euclidian Distance (ED) matrix w between the N_{all} TACs (I_1, \dots, I_N) with all possible M -ary APM symbols according to Eq. 68, then eliminating $N_{re} = N_{all} - N$ TACs having the minimum ED.

$$w_{m,n} = \sqrt{\|\mathbf{H}_{I_m}\mathbf{s}_m - \mathbf{H}_{I_n}\mathbf{s}_n\|_F^2}, \quad (68)$$

where I_m and I_n are the TACs of index m and n respectively and they contain the indices of the activated TAs within a TAC, \mathbf{H}_{I_m} is the $N_r \times N_a$ sub-matrix of \mathbf{H} that contains N_a columns of \mathbf{H} at the indices of activated TAs, and \mathbf{s} represents the M -ary symbol vector of N_a elements with M^{N_a} possibilities.

The number of ED estimations to generate the matrix \mathbf{W} can be reduced from $N_{all}^2(M^{N_a})^2$ to $N_{all} \frac{(N_{all}+1)}{2} \cdot (M^{N_a} \frac{(M^{N_a}+1)}{2})$ by removing the repeated estimations due to symmetry in each $w_{m,n}$ and \mathbf{W} .

Despite the optimal TAC selection of this method, it still have a large complexity for real time estimation of these EDs especially with large values M -ary and N_{all} . In addition, the useful data rate will be highly reduced in fast time variant channel due to the overhead of the feedback channel.

5.3.4 Simplified GSM System (S-EGSM)

In this method, we are targeting the mmWave and sub-THz bands where the antenna size and separation are very small which leads to a high spatial correlation. Thus, the spatial correlation matrices in (85) are the dominant terms that will highly affect the detection of the activated TAC. For this reason, we propose a simplified EGSM (S-EGSM) that considers only the Tx spatial correlation matrix instead of the complete channel matrix \mathbf{H} , where there is a larger number of antennas compared to the Rx side. In addition, the Tx spatial correlation matrix has very low variations (quasi-constant) for a specific Tx because it depends mainly on the antenna characteristics, separation and array geometry. Therefore, S-EGSM is a TAC selection method without instantaneous CSI, where the feedback channel is no more required as in EGSM because the transceivers agree on the TAC set only once at the setup phase and they can update them accordingly when the transmit spatial correlation is changed. The S-EGSM system can be described as shown in Fig. 41 but without using the CSI feedback (\mathbf{H}).

The algorithm can be summarized as follows:

1. Generate all possible TACs according to N_t and N_a .
2. Using only the transmit spatial correlation, compute the lower or upper part of ED matrix \mathbf{W}' since by symmetry $w'_{m,n} = w'_{n,m}$:

$$w'_{m,n} = \underset{\forall \mathbf{s}_m, \mathbf{s}_n}{\left\| \hat{\mathbf{H}}_{Im} \mathbf{s}_m - \hat{\mathbf{H}}_{In} \mathbf{s}_n \right\|_F^2}, \quad (69)$$

where $\hat{\mathbf{H}}$ is calculated according to Eq.85 with $\mathbf{H}_{LoS} = \mathbf{0}_{Nr \times Nt}$, $\mathbf{H}_{NLoS} = \mathbf{I}_{Nr \times Nt}$, and $\Sigma_r = \mathbf{I}_{Nr \times Nr}$ and any values of the K factor since it will not affect the results of this method.

3. Sort the ED values in ascending order

$$[v_1, v_2, \dots] = \text{sort}(w', \text{'ascend'}) \quad (70)$$

4. Obtain the TAC set by removing N_{re} TAC starting with those that generate the smallest EDs (v_1, v_2, \dots).

Note that another TAC selection method without CSI was proposed in [82]. In the following, we will compare our proposed method (S-EGSM) to the methods proposed in [82].

5.3.5 Index-to-Bit Mapping: Spatial Mapping

After reducing the TAC error probabilities in the TAC selection methods, an efficient spatial mapping (Index-to-Bit Mapping) is proposed to further reduce the spatial BER and thus the total BER. In conventional GSM, the spatial mapping was simply the normal binary representation of the index ($m - 1$) of the TAC I_m , i.e the spatial bits for I_1 to I_4 were coded as 00, 01, 10, 11 respectively.

In this subsection, we propose a spatial mapping method that takes into consideration the effect of spatial correlation. Note that the spatial correlation will lead to high similarity

between the channels of neighbor TACs, so when the Rx mis-detects the activated TAC, it will most probably be confusing by one of its neighbors.

Therefore, a Gray coding for spatial bits among each group of neighbor TACs can reduce the total BER. The spatial correlation is the highest between the adjacent antennas, so the order of correlation between any pair of TACs can be deduced from the Hamming distance between their antenna indices. The algorithm for the proposed mapping is summarized in the following: **Step 1:Step 1:**

1. Compute the Hamming Distance (HD) matrix using the indices of activated antennas between the N possible legitimate TACs according to the following equation:

$$\mathbf{HD}_{m,n} = \sum_{i=1}^{N_a} |m_i - n_i|, \quad (71)$$

where $I_m = \{m_1, \dots, m_{N_a}\}$ and $I_n = \{n_1, \dots, n_{N_a}\}$ and the activated antennas indices m_i and n_i on each TAC are sorted in ascending order. In addition, the number of $\mathbf{HD}_{m,n}$ can be reduced from N^2 to $(N-1)\frac{N}{2}$ by benefiting from the symmetry ($\mathbf{HD}_{m,n} = \mathbf{HD}_{n,m}$) and skipping the distance calculation between the same TACs.

2. Compute the frequency of $\text{HD} = 1$ for all TACs $\lambda_m^{HD=1} : \lambda_1^1, \dots, \lambda_N^1$ that represents the number of nearest neighbors for each TAC.
3. Sort the N TACs in descending order according to their λ_m^1 :

$$[p_1, p_2, \dots, p_N] = \text{sort}(\lambda_m^1, \text{'descend'}). \quad (72)$$

4. Start the Gray coding by assigning an unused bit mapping for the TAC that have the highest number of nearest neighbors (p_1, p_2, \dots). If this TAC has a previously assigned bit mapping skip this step.
5. Generate the Gray code set for this TAC where any bit mapping in the set differs only by a single bit.
6. Get the allowed Gray set for this TAC by removing the used bit mapping.
7. Assign a bit mapping from its allowed Gray set to its neighbor TACs ($\text{HD} = 1$) if it is not previously assigned.
8. Repeat from Step 4 until a bit mapping is assigned for all TACs.

In the following, we will illustrate an example for Gray coded spatial mapping with $N_t = 5$ and $N_a = 2$. Thus, the legitimate TACs (I_1, \dots, I_8) shown in Table 5 are obtained from the TAC selection, and each TAC index will be mapped to $\log_2(8) = 3$ spatial bits.

Consider a uniform linear antenna array, the HDs between indices of activated antennas are generated using Eq. 71, i.e. $\text{HD}_{1,2} = |1 - 1| + |4 - 5| = 1$. Note that the HD matrix for these TACs and the λ_m^1 are represented in Table 5 (Step 1, 2). Firstly, the Gray coding algorithm starts with the TAC I_3 that has the highest number ($\lambda_3^1 = 4$) of nearest neighbors (I_1, I_4, I_5, I_7) as shown in Table 5. Then according to Step 3 to 6, I_3 is initialized with '000',

Table 5: HD matrix for Spatial Mapping example with $N_t = 5$ and $N_a = 2$

$I_m \setminus I_n$	I_1	I_2	I_3	I_4	I_5	I_6	I_7	I_8
$I_1 = \{1, 4\}$	0	1	1	2	2	1	2	3
$I_2 = \{1, 5\}$	1	0	2	1	3	2	3	2
$I_3 = \{2, 4\}$	1	2	0	1	1	2	1	2
$I_4 = \{2, 5\}$	2	1	1	0	2	3	2	1
$I_5 = \{2, 3\}$	2	3	1	2	0	1	2	3
$I_6 = \{1, 3\}$	1	2	2	3	1	0	3	4
$I_7 = \{3, 4\}$	2	3	1	2	2	3	0	1
$I_8 = \{3, 5\}$	3	2	2	1	3	4	1	0
λ_m^1	3	2	4	3	2	2	2	2

then its Gray Set is generated $\{001, 100, 010\}$ and nothing is removed because not all bit mappings have yet been used. Then, the bit mapping for I_1, I_4, I_5 are assigned respectively from its Gray set and I_7 is left for future assignment by another TAC. Next, the neighbors for $I_1 = 001$ (previously assigned) with $\lambda_3^1 = 3$ will be assigned from its allowed Gray set $\{101, 011, 000\}$. Finally, these steps are continuously repeated until a bit mapping is assigned for all TACs.

This best effort Gray coding for spatial bits is trying to reduce the effect of spatial correlation that causes a confusion in the detector at Rx between neighbor TACs. Therefore, this method should enhance the spatial BER because it limits the number of different bits between neighbors TAC to minimum possible.

5.3.6 Simulations results and discussions

In this section, firstly we compare our proposed technique for TAC selection S-EGSM to the existing methods EGSM and No CSI method in [82]. Note that both methods without instantaneous CSI (S-EGSM and No CSI from [82]) estimate offline the best legitimate TAC set once in the setup phase and they will keep using this set all the time while the Tx configuration (N_t and N_a) and antenna array characteristics are unchanged. However, the EGSM method is an adaptive TAC selection that keeps tracking the channel variation and updates the TAC set accordingly. Hence, this method requires a feedback channel to share the selected TAC set between the transceiver. For a fair comparison, we set the same GSM configuration with the same channels and transmitted bit-stream for all TAC selection methods. These TAC selection methods are compared under different transmit correlation factors to highlight the importance of the proposed method S-EGSM in highly correlated channel.

The correlation matrices in the Kronecker model are formed according to the exponential model of [75] where the elements of the transmit Σ_t and the receive Σ_r correlation matrices are affected by a correlation factor β : $[\Sigma_t]_{i,j} = \beta_t^{|i-j|}$. We used $\Sigma_r = I_{N_r}$ to concentrate on the impact of correlation at the Tx side where a larger antenna array is used to convey the data in the spatial domain of index modulation.

The following parameters are adopted with all TAC selection methods: $GSM(N_t, N_a, M) =$

$GSM(6, 2, 2)$, $Nr = 4$, $\beta_t = \{0, 0.4, 0.8\}$, the number of GSM symbols is 10^4 simulated under 100 channel realizations. In addition, S-EGSM takes into consideration only the transmit spatial correlation matrix which is the dominant term in highly correlated channels. For this reason, Rician channel is used with $K = 5$ to prove that the S-EGSM will not be affected by the LoS component even when neglecting the Rician K factor in Step 2 of the S-EGSM algorithm. Moreover, the adopted GSM detector in these systems is OB-MMSE that is able to detect the TAC and the APM constellations with a balanced trade-off between system performance and complexity.

The results in Fig. 42 to Fig. 44 show that adaptive method EGSM with CSI has the best performance in all correlation levels because it keeps updating the legitimate TAC set instantaneously according to channel variations. However, we notice in Fig. 42 to Fig. 44 that the No CSI method from [82] has a slightly better performance at low SNR compared to S-EGSM, but as transmit correlation level increases the S-EGSM performance at high SNR becomes the best TAC selection without instantaneous CSI. Moreover, the advantage of No CSI method [82] at low SNR disappears in highly correlated channel $\beta_t = 0.8$ and the performance of proposed S-EGSM becomes better by 1.4 dB at $BER=10^{-4}$ compared to the other method without CSI.

Therefore, the S-EGSM is an efficient TAC selection method without instantaneous CSI in highly correlated channel which is the case in mmWave and THz bands where the correlation factor is in the order of $\beta_t = 0.8$ according to [76]. However, the TAC selection with CSI EGSM can be used in slow time variant channel (small Doppler) to achieve the optimal performance, while in fast variant channels TAC selection methods without instantaneous CSI is preferred to avoid the increased complexity due to real time TAC selection and to limit the overhead of the feedback channel. Finally, the usage of S-EGSM technique in fast variant channel environment depends on the correlation level where it will be highly recommended for highly correlated channels.

In the following, the spatial mapping with binary and gray coding is compared under the same conditions with different correlation levels. For this comparison, we used $GSM(7, 4, 2)$ where we have $\lfloor \log_2(C_7^4) \rfloor = 5$ spatial bits. As shown in Fig. 45, as the correlation factor increases, the Gray coding gain increases from 0.15 dB to 0.4 dB. Note that the gray coding gain is higher when TAC selection is not used because it reduces the number of neighbor TACs.

Consequently, the gray coding gain appears when the detector at the Rx is confused between the activated TAC and one of its neighbor TACs ($HD=1$). This mis-detection of the activated TAC can cause a single bit error only if this TAC and its neighbors are Gray coded. Thus, the gray coding advantages appear more in highly correlated channel as shown in Fig. 45 where the neighbor TACs cannot be distinguishable at the Rx side in order to correctly detect the activated TAC.

Moreover, this gain does not appear always because the gray coding for spatial bits is a best effort algorithm where we try to reduce the number of bits difference between neighbor TACs. However, the gray coding for all neighbor TACs is not always guaranteed, so this gain in some cases might vanish and the performances for both the gray and normal binary coding become similar. Note that the Gray coding for spatial bits is prepared offline once for a given GSM configuration. Therefore, the gray coding should be used in spatial mapping

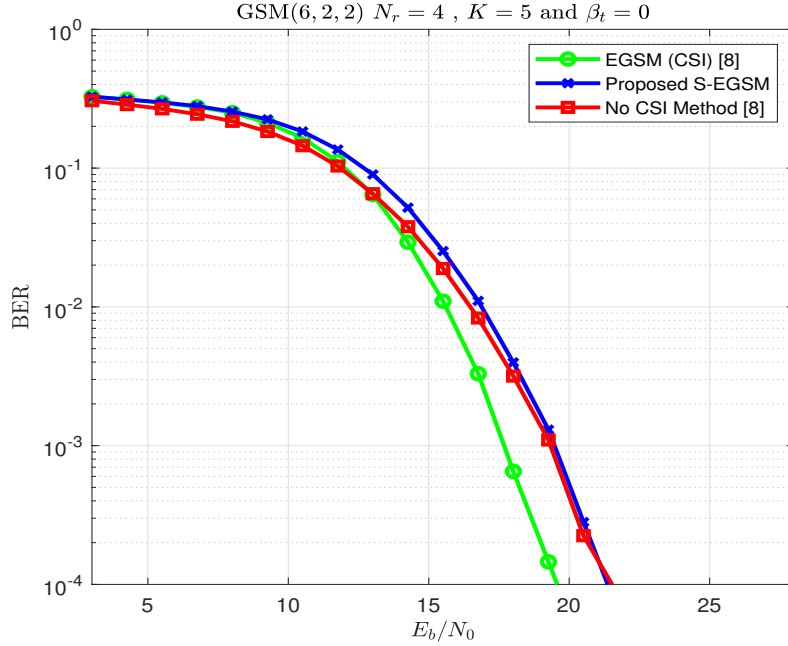


Figure 42: BER vs E_b/N_0 for various TAC selection with $\beta_t = 0$

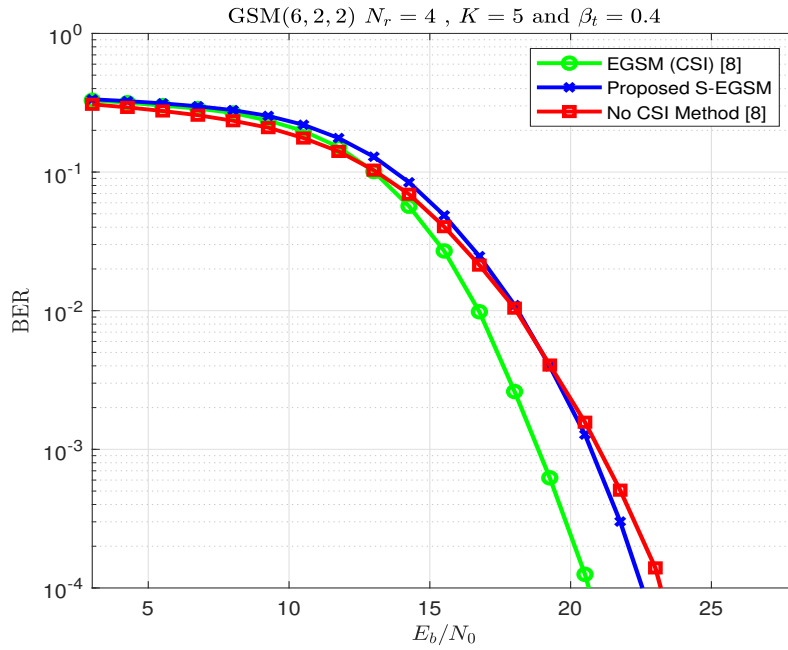


Figure 43: BER vs E_b/N_0 for various TAC selection with $\beta_t = 0.4$

because in all cases it will have some gain or nothing but it will never have a loss compared to normal binary coding for spatial bits.

In the following, we show that the gray coding gain is larger when all the neighbor TACs are gray coded. For example, the gray coding for all neighbors can be satisfied when SM is taken into consideration because it has a single active antenna instead of N_a ($SM(N_t, M) =$

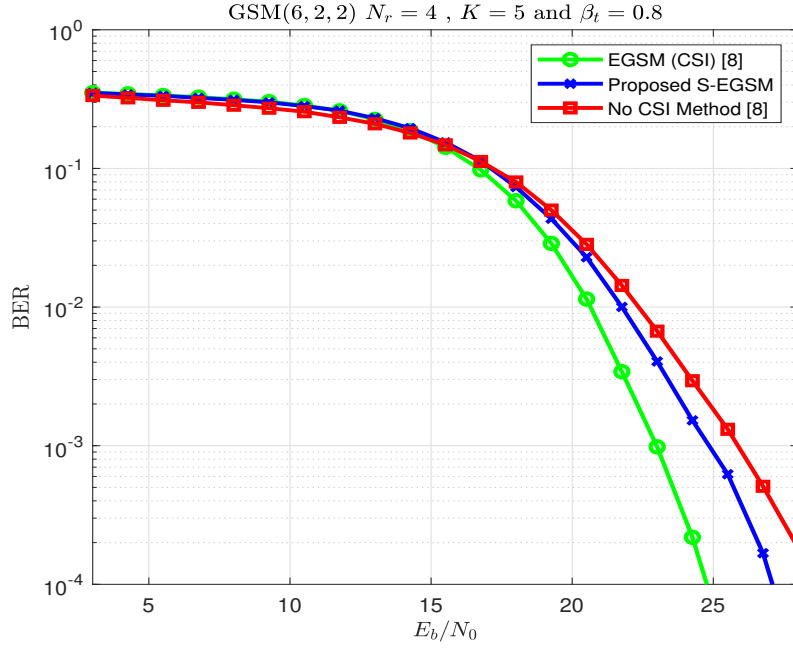


Figure 44: BER vs E_b/N_0 for various TAC selection with $\beta_t = 0.8$

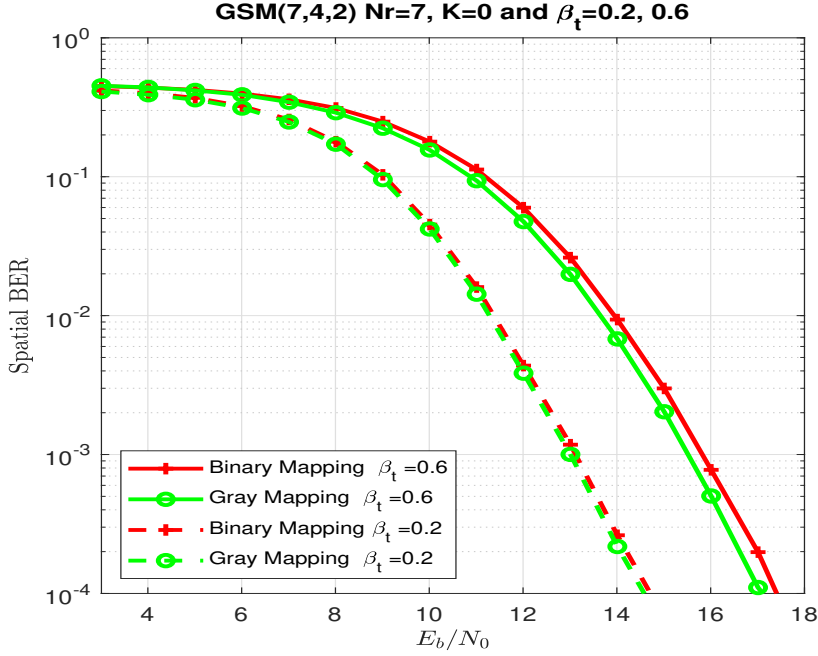


Figure 45: BER vs E_b/N_0 for different TAC spatial mapping with $\beta_t = \{0.2, 0.6\}$

$GSM(N_t, 1, M)$). The gray coding gain increases with SNR for $SM(16, 2)$ and $N_r = 2$ in a highly correlated Rician channel ($K = 5$) as shown in Fig. 46 where it reaches 1.5 dB at $BER=5.10^{-4}$.

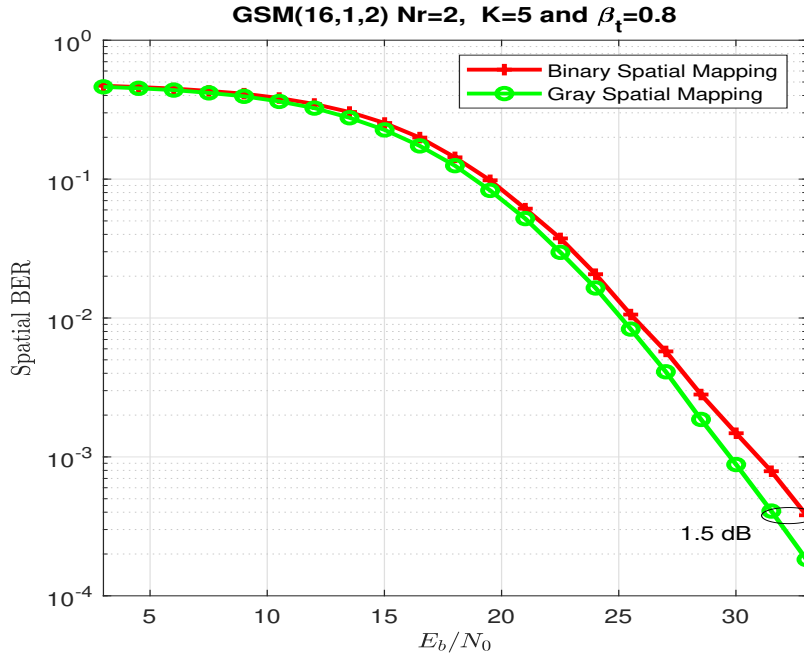


Figure 46: Spatial BER vs E_b/N_0 for binary and gray coding for spatial bits

5.3.7 General conclusions

GSM is a promising technique for ultra-high data rate systems but its performance degrades in highly correlated channels. In order to enhance the BER performance of GSM in these channels, we focused on two aspects: the legitimate TAC selection and the spatial bit mapping that was ignored in conventional GSM.

Firstly, we proposed a TAC selection method without instantaneous CSI (S-EGSM) for highly correlated channels, where we consider only the transmit spatial correlation which is the dominant term in the channel. The simulation results show that S-EGSM outperforms the other no CSI-based methods [82] in highly correlated channel by 1.4 dB. This gain is less significant when the correlation factor becomes low. Note that the TAC selection without instantaneous CSI is suitable for fast time varying channels since it permits to avoid the overhead of the feedback channel and the increased complexity in real time TAC selection. However, the adaptive TAC selection with CSI (EGSM) can be adopted in slow-time varying channels to get the optimal performance.

Next, we proposed the Gray coding for spatial bits in GSM that permits to limit the number of different bits between neighbor TACs to one bit. However, the gray coding between all neighbors TACs is not always guaranteed. Simulation results showed that the Gray-based mapping method outperforms the normal binary spatial mapping by 1.5 dB in highly correlated channels.

5.4 Dual Polarized Generalized Spatial Modulation Scheme

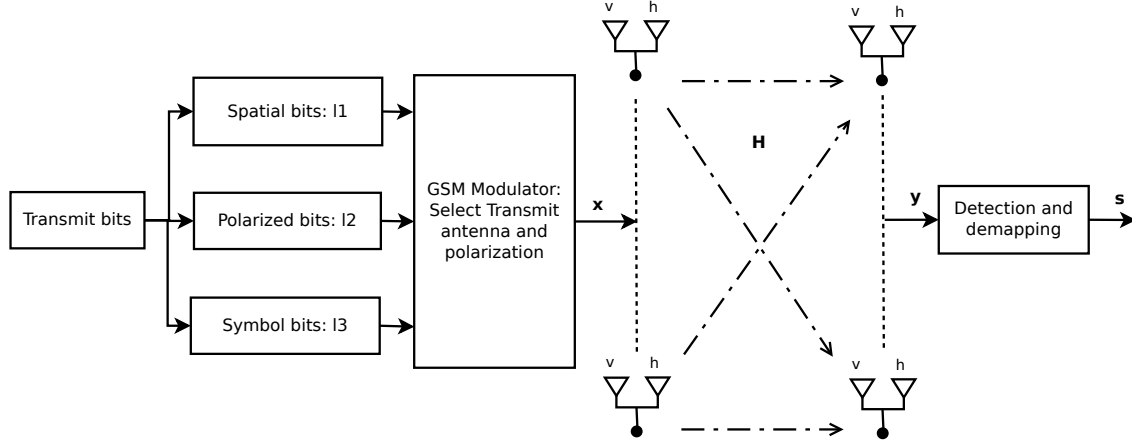
5.4.1 Introduction

In the context of BRAVE project [83], we explore new techniques for wireless terabit communication system. Thus, Index Modulation (IM) with advanced MIMO schemes and a huge bandwidth (around 50 GHz) that can be allocated in the sub-THz bands (mainly between 90 GHz-200 GHz) [26], are the key enablers to increase the SE and data rates. Spatial modulation (SM) has been recognized as a low-complexity MIMO scheme [84], where a single antenna at each time slot is activated to convey information by its index. The main advantage of SM is that the interference at the receiver and the inter-antenna synchronization at transmitter are avoided. However, the SE of the SM-MIMO technique increases logarithmically with number of transmit antennas (TAs).

To further increase the SE, the Uni-Polarized Generalized Spatial Modulation (UP-GSM) technique was developed in [85]. It uses the space dimension of antenna array to conveys information by the index of the activated transmit antenna combination (TAC) and by the M-ary symbols [86]. In [87], it was shown that using the UP-GSM with power efficient single carrier modulations can successfully achieve a low power Terabits system.

Despite the multiple advantages of UP-GSM system, the latter suffers from an important performance degradation with Rician channel and in spatially correlated channels. Note that the degradation due to spatial correlation is reduced in [88] but cannot be completely eliminated. In addition, the space occupancy of uni-polarized (UP) antenna arrays in MIMO systems can limit the number of antennas due to physical space limitation especially at low frequency bands. To deal with the space limitation, an efficient solution has been proposed for the SM-MIMO system, by adding a polarization dimension to the transmitter and receiver using dual-polarized (DP) antennas that can transmit simultaneously through two orthogonal polarization directions. But in DP-SM [89] only one polarization is used to allow better separation between channels and thus better performance in highly correlated channel. At the receiver, the detection algorithm for UP-GSM involves the estimation of both the transmitted M-ary symbols and the index of the activated TAC that can be performed jointly using maximum-likelihood (ML) detector or using sub-optimal detectors as the ordered blocked minimum mean-squared error (OB-MMSE) [90].

In this subsection, we propose a DP-GSM scheme where we incorporate DP antennas with GSM to reduce the spatial correlation impact and also to enhance the system SE by exploring the polarization dimension. In addition, DP-GSM allows to reduce the space occupancy of antenna arrays by half without any performance degradation compared to UP-GSM. In contrast to UP-GSM, DP-GSM should detect the polarization bits conveyed by the activated polarization of each active antenna, in addition to the estimation of the spatial and the symbol bits. For this reason, the joint maximum-likelihood (ML) detector for DP-GSM that achieves optimal performance is proposed, and a sub-optimal detector of lower complexity, named Modified OB-MMSE (MOB-MMSE), is presented to additionally estimate the polarization bits compared to OB-MMSE. Moreover, the performance analysis of the proposed DP-GSM system is addressed over spatially correlated/uncorrelated Rayleigh Rician channels with different cross-polarization correlation, and also over sub-THz channels. To further illustrate the potential of the DP-GSM system, the UP-GSM and the dual polarized multiple-input multiple-output systems with Spatial Multiplexing (DP-SMX) are compared against our system.


 Figure 47: $N_r \times N_t$ DP-GSM system model.

5.4.2 System model: Dual-Polarized GSM system

The proposed system model is a MIMO system with N_t and N_r DP antennas at transmitter and receiver, respectively, and based on the GSM, in which N_a ($N_a < N_t$) antennas are activated in each time slot. Therefore, the number of TAC combinations is $C_{N_t}^{N_a}$ that represents the binomial coefficient. However, only $2^{\lfloor \log_2(C_{N_t}^{N_a}) \rfloor}$ antenna combinations are permitted to keep the bits length an integer number, where $\lfloor x \rfloor$ is the greatest integer smaller than x .

The $N_r \times N_t$ DP-GSM system leads to $2N_r \times 2N_t$ dimensional channel between transmitter and receiver due to the implemented dual polarization. The DP-GSM system is shown in Fig. 47.

At each transmission instant, a block of $L = L_1 + L_2 + L_3$ incoming data bits are selected and constituted of three parts named: $L_1 = \lfloor \log_2(C_{N_t}^{N_a}) \rfloor$ bits are used to select the N_a activated antennas at the transmitter, $L_2 = N_a \log_2 N_p$ bits used to select the polarizations of the selected antennas. Here $N_p = 2$ stands the polarization dimension. Note that the polarization directions can be vertical, denoted by 'v' or horizontal denoted 'h'. The remaining $L_3 = N_a \log_2 M$ represent the bits mapped into N_a M -ary symbol of the transmitted constellation symbol vector $\mathbf{s} = [s_1, s_2, \dots, s_{N_a}]^T$ where $[.]^T$ is the transpose operator. Thus, the total achieved SE in bit per channel use (bpcu) can be expressed as

$$L = \lfloor \log_2 (C_{N_t}^{N_a}) \rfloor + N_a \log_2 M + N_a \quad (73)$$

By doing so, the number of possible TACs is $N_1 = 2^{\lfloor \log_2(C_{N_t}^{N_a}) \rfloor}$ and the number of possible transmit polarization combinations (TPCs) is $N_2 = 2^{N_a}$. Thus the total number of possible combinations using TACs and TPCs is $N = N_1 N_2$.

The transmitted signal is denoted by \mathbf{x} and represented by a $2N_t \times 1$ vector whose entries have N_a non-zero elements. The position of the non-zero elements in \mathbf{x} allows the identification of the selected TAs as well as their polarizations and the transmitted symbols. We denote in this work i_1, i_2, \dots, i_{N_a} as the indices of N_a active antenna in the i -th TAC, where $i \in \{1, 2, \dots, N_1\}$ and we denote $\ell_1, \ell_2, \dots, \ell_{N_a}$ as the corresponding polarization of the activated antennas at the ℓ -th TPC where $\ell \in \{1, 2, \dots, N_2\}$. The TA with index $i_q \in \{1, 2, \dots, N_t\}$ and polarization $\ell_q \in \{v, h\}$ sends out symbols s_q where $q \in \{1, 2, \dots, N_a\}$. The transmit signal

vector \mathbf{x} is given by

$$\mathbf{x} = [..., [0, 0], [0, \underset{\substack{i_1 \\ \downarrow \\ \ell_1=h}}{s_1}], ..., [\underset{\substack{i_2 \\ \downarrow \\ \ell_2=v}}{s_2}, 0], ..., [0, \underset{\substack{i_{N_a} \\ \downarrow \\ \ell_{N_a}=h}}{s_{N_a}}], ...]^T \quad (74)$$

At receiver, N_r DP antennas receive the modulated signal transmitted over a slow fading and frequency-flat MIMO channel. The channel matrix \mathbf{H} is equivalent to a $2N_r \times 2N_t$ matrix represented as

$$\mathbf{H} = \begin{bmatrix} h_{1v,1v} & h_{1v,1h} & h_{1v,2v} & \cdots & h_{1v,N_t h} \\ h_{1h,1v} & h_{1h,1h} & h_{1h,2v} & \cdots & h_{1h,N_t h} \\ h_{2v,1v} & h_{2v,1h} & h_{2v,2v} & \cdots & h_{2v,N_t h} \\ \vdots & \vdots & \vdots & \vdots & \vdots \\ h_{Nr,h,1v} & h_{Nr,h,1h} & h_{Nr,h,2v} & \cdots & h_{Nr,h,N_t h} \end{bmatrix}, \quad (75)$$

where each $h_{i'u,j'u'}$ and $u, u' \in \{v, h\}$, represents the fading coefficient between polarization u of i' -th receive antenna and the polarization u' of j' -th TA. If $u' = u$, $h_{i'u,j'u'}$ represents the co-polar channel coefficient; otherwise, it represents the cross-polar channel coefficient. We can reformulate (75) as $\mathbf{H} = [\mathbf{H}_1, \mathbf{H}_2, \dots, \mathbf{H}_{N_t}]$ where $\mathbf{H}_{j'} = [\mathbf{h}_{j'v}, \mathbf{h}_{j'h}] \in \mathbb{C}^{2N_r \times 2}$ and $\mathbf{h}_{j'v} = [h_{1v,j'v}, h_{1h,j'v}, h_{2v,j'v}, \dots, h_{Nr,h,j'v}]^T$ is the a $2N_r \times 1$ channel matrix for polarization v of j' -th TA. Similarly, $\mathbf{h}_{j'h} = [h_{1v,j'h}, h_{1h,j'h}, h_{2v,j'h}, \dots, h_{Nr,h,j'h}]^T$ is the a $2N_r \times 1$ channel matrix for polarization h of the j' -th TA.

To be able to model correctly the channel \mathbf{H} , two kind of polarizations are investigated in our Subsection 5.4. Correlations induced by polarization effects within each antenna, and the limited spacing between antennas [89]. These effects will be studied in the next subsection. The received signal $\mathbf{y} \in \mathbb{C}^{2N_r \times 1}$ can be formulated as

$$\mathbf{y} = \mathbf{H}\mathbf{x} + \mathbf{n} = \sum_{q=1}^{N_a} \mathbf{h}_{i_q \ell_q} s_q + \mathbf{n} = \mathbf{H}_{I,P} \mathbf{s} + \mathbf{n} \quad (76)$$

where $\mathbf{n} \in \mathbb{C}^{2N_r \times 1}$ is additive white complex Gaussian noise with zero mean and variance σ^2 , $\mathbf{H}_{I,P} = [\mathbf{h}_{i_1 \ell_1}, \mathbf{h}_{i_2 \ell_2}, \dots, \mathbf{h}_{i_{N_a} \ell_{N_a}}]$ is the sub-matrix with N_a columns of \mathbf{H} , corresponding to the TAC set I and TPC set P .

5.4.3 Joint-ML Detector

5.4.4 Modified OB-MMSE Detector

In order to reduce complexity by avoiding the use of the joint ML detector, we propose a modified version of OB-MMSE detector which has been successfully used for UP-GSM where polarization dimension is not used [90]. Therefore, in addition to the estimation of the indices of the N_a possible activated TAs, we propose to estimate their polarizations. Concretely, the pseudo-inverse of channel column $z_{i_q \ell_q}$ is computed and then weighting factors $w^{i,\ell}$ are calculated to measure the joint reliability of (TAC, TPC) as follows:

$$w^{i,\ell} = \sum_{q=1}^{N_a} z_{i_q \ell_q}^2 \quad \text{with } z_{i_q \ell_q} = \frac{\mathbf{h}_{i_q \ell_q}^H \mathbf{y}}{\mathbf{h}_{i_q \ell_q}^H \mathbf{h}_{i_q \ell_q}} \quad (77)$$

We recall the reader that the total number of TA and polarization combination (i, ℓ) corresponds to N . Sorting the weighing factor values of the vector $\mathbf{w} = [w^{i,\ell}; i \in \{1, 2, \dots, N_1\}, \ell \in \{1, 2, \dots, N_2\}]^T$ in descending order, we obtain the ordered activated TA and polarization combination (TAPC) as follows

$$[k_1, k_2, \dots, k_N] = \text{arg sort}(\mathbf{w}) \quad (78)$$

Note that the TAPC index k_n contains implicitly the TAC and TPC indices (i, ℓ) and it is represented by $I_{i \leftarrow k_n} P_{\ell \leftarrow k_n}$. Consequently, a block MMSE detector with dimension of $2N_r \times N_a$ is used for each possible TAPC to detect the vector symbol $\tilde{\mathbf{s}}_n$ with $n \in \{1, 2, \dots, N\}$

$$\tilde{\mathbf{s}}_n = D \left((\mathbf{H}_{I_{i \leftarrow k_n} P_{\ell \leftarrow k_n}}^H \mathbf{H}_{I_{i \leftarrow k_n} P_{\ell \leftarrow k_n}} + \sigma^2 \mathbf{I})^{-1} \mathbf{H}_{I_{i \leftarrow k_n} P_{\ell \leftarrow k_n}}^H \mathbf{y} \right) \quad (79)$$

where \mathbf{I} is the $N_a \times N_a$ identity matrix and $D(\cdot)$ is the digital demodulator function. For the reduction of the detection complexity of all N possible TAPC, the MOB-MMSE will end once the output $(i, \ell, \tilde{\mathbf{s}}_n)$ satisfies the following relation (see the process to line 10 - Algorithm 1)

$$\|\mathbf{y} - \mathbf{H}_{I_{i \leftarrow k_n} P_{\ell \leftarrow k_n}} \tilde{\mathbf{s}}_n\|^2 \leq V_{th} \quad (80)$$

where $V_{th} = 2N_r\sigma^2$ is a threshold to be set to produce the detected signal vector. If the n -th output satisfies the condition (80), the detector will provide the optimal TAC \hat{I} and TPC \hat{P} , and the estimated symbol vector $\tilde{\mathbf{s}}_n$. Otherwise, the detector will continue the same procedure with $n = n + 1$ until $n > N$. In this case, the detector becomes equivalent to the optimal ML algorithm as follows (See steps (14-17) in the Algorithm 1)

$$\begin{cases} u = \arg \min_n d_n, n \in \{1, 2, \dots, N\} \\ \hat{I} = I_{i \leftarrow k_u}, \hat{P} = P_{\ell \leftarrow k_u}, \hat{\mathbf{s}} = \tilde{\mathbf{s}}_u. \end{cases} \quad (81)$$

The MOB-MMSE detection algorithm is summarized in Algorithm 1.

Algorithm 1: Proposed MOB-MMSE detection algorithm

- 1: **Input:** \mathbf{y} , \mathbf{H} , N_t , N_a , \dots , $V_{th} = 2N_r\sigma^2$.
- 2: $\mathbf{z} = [z_{1v}, z_{1h}, \dots, z_{N_t v}, z_{N_t h}]^T$, with $z_{i_q \ell_q} = \frac{\mathbf{h}_{i_q \ell_q}^H \mathbf{y}}{\mathbf{h}_{i_q \ell_q}^H \mathbf{h}_{i_q \ell_q}}$;
- 3: $\mathbf{w} = [w^{1,1}, w^{1,2}, \dots, w^{N_1, N_2}]^T$, $w^{i,\ell} = \sum_{q=1}^{N_a} z_{i_q \ell_q}^2$, $i \in \{1, 2, \dots, N_1\}$ and $\ell \in \{1, 2, \dots, N_2\}$;
- 4: $[k_1, k_2, \dots, k_N] = \text{arg sort}(\mathbf{w})$;
- 5: **Initial:** $n = 1$,
- 6: **Main:**
- 7: **while** $n \leq N$ **do**
- 8: $\tilde{\mathbf{s}}_n = D \left((\mathbf{H}_{I_{i \leftarrow k_n} P_{\ell \leftarrow k_n}}^H \mathbf{H}_{I_{i \leftarrow k_n} P_{\ell \leftarrow k_n}} + \sigma^2 \mathbf{I})^{-1} \mathbf{H}_{I_{i \leftarrow k_n} P_{\ell \leftarrow k_n}}^H \mathbf{y} \right)$
- 9: $d_n = \|\mathbf{y} - \mathbf{H}_{I_{i \leftarrow k_n} P_{\ell \leftarrow k_n}} \tilde{\mathbf{s}}_n\|^2$

```

10:  If  $d_n < V_{th}$ 
11:   $\hat{I} = I_{i \leftarrow k_n}$ ,  $\hat{P} = P_{\ell \leftarrow k_n}$ ,  $\hat{\mathbf{s}} = \tilde{\mathbf{s}}_n$ , break
12:  Else  $n = n + 1$  end if
13:  end while
14:  if  $n > N$ 
15:   $u = \arg \min_n d_n$ ,  $n \in \{1, 2, \dots, N\}$ 
16:   $\hat{I} = I_{i \leftarrow k_u}$ ,  $\hat{P} = P_{\ell \leftarrow k_u}$ ,  $\hat{\mathbf{s}} = \tilde{\mathbf{s}}_u$ ,
17:  end if
18: Return  $\hat{I}, \hat{P}, \hat{\mathbf{s}}$ 

```

5.4.5 Channel model

The DP-GSM system may experience spatial correlation at transmitter and receiver due to the insufficient spacing among antennas and can be modeled as a matrix form, Σ_t and Σ_r , respectively. Various models are used to describe the spatial correlations, and the exponential correlation model is used in this study [91]. Therefore, the correlation among i' -th and j' -th antenna is affected by the correlation factor $|\beta| < 1$: $|\Sigma_t|_{i',j'} = \beta^{|i'-j'|}$.

The DP-GSM system may suffer also from the cross polarization correlation (XPC) between orthogonal polarization directions as shown in [92]. The polarization correlation at the transmitter and the receiver can be expressed as follows

$$\Pi_t = \begin{bmatrix} 1 & \gamma_t \\ \gamma_t^* & 1 \end{bmatrix}, \quad \Pi_r = \begin{bmatrix} 1 & \gamma_r \\ \gamma_r^* & 1 \end{bmatrix}, \quad (82)$$

respectively, with

$$\gamma_t = \frac{E\{h_{i'v,i'v}h_{i'v,i'h}^*\}}{\sqrt{\mu(1-\mu)}} = \frac{E\{h_{i'h,i'v}h_{i'h,i'h}^*\}}{\sqrt{\mu(1-\mu)}} \quad (83)$$

$$\gamma_r = \frac{E\{h_{j'v,j'v}h_{j'h,j'h}^*\}}{\sqrt{\mu(1-\mu)}} = \frac{E\{h_{j'h,j'v}h_{j'h,j'h}^*\}}{\sqrt{\mu(1-\mu)}} \quad (84)$$

where the parameter $0 < \mu \leq 1$ is the amount of power leakage from one polarization to the other [93]. Assuming the symmetry condition between different polarization, the leakage parameter is given as follows $\mu = E\{|h_{i'v,i'h}|^2\} = E\{|h_{i'h,i'v}|^2\}$ and $1 - \mu = E\{|h_{i'v,i'v}|^2\} = E\{|h_{i'h,i'h}|^2\}$. In the literature, the cross-polarization discrimination (XPD) is defined as the ratio between $1 - \mu$ and μ . For larger XPD values, the two polarization directions are easier to be discriminated. In [94], it has been demonstrated that the impact of the cross-polarization is relatively small and $0 \leq |\gamma_r|, |\gamma_t| \leq 0.2$.

In our study, we consider a slow fading MIMO channel matrix as Rayleigh or Rician multipath fading channel with/without spatial correlation and with polarization correlation. Therefore, the $2N_r \times 2N_t$ DP-polarized channel matrix is expressed in the Kronecker form given by

$$\mathbf{H} = \sqrt{\frac{K}{1+K}}(\mathbf{1}_{N_r \times N_t} \otimes \boldsymbol{\Gamma}) \odot \mathbf{H}_{\text{LOS}} + \sqrt{\frac{1}{1+K}}(\mathbf{1}_{N_r \times N_t} \otimes \boldsymbol{\Gamma}) \odot (\boldsymbol{\Psi}_r^{\frac{1}{2}} \mathbf{H}_{\text{NLOS}} \boldsymbol{\Psi}_t^{\frac{1}{2}}) \quad (85)$$

where $\boldsymbol{\Gamma}$ is the leakage matrix

$$\boldsymbol{\Gamma} = \begin{bmatrix} \sqrt{1-\mu} & \sqrt{\mu} \\ \sqrt{\mu} & \sqrt{1-\mu} \end{bmatrix} \quad (86)$$

The operator \odot denotes the element-by-element Hadamard multiplication, \otimes denotes the Kronecker product, $\mathbf{1}_{N_r \times N_t}$ is an all one $N_r \times N_t$ matrix, K is the Rician factor, \mathbf{H}_{LoS} and \mathbf{H}_{NLoS} are the $2N_r \times 2N_t$ line of sight (LoS) and the non LoS channel matrix respectively. The elements of \mathbf{H}_{LoS} are deterministic and we will assume that the elements are all one, and \mathbf{H}_{NLoS} is considered as Rayleigh channel whose elements are independent and identically distributed (*iid*) circularly symmetric zero mean complex Gaussian variables with unit variance denoted $\mathcal{CN}(0, 1)$. Finally, the matrices $\boldsymbol{\Psi}_r = \boldsymbol{\Sigma}_r \otimes \boldsymbol{\Pi}_r$ and $\boldsymbol{\Psi}_t = \boldsymbol{\Sigma}_t \otimes \boldsymbol{\Pi}_t$ are the $2N_r \times 2N_r$ and $2N_t \times 2N_t$ composite transmit and receive correlation matrices, combining spatial and polarization correlations.

5.4.6 Performance analysis

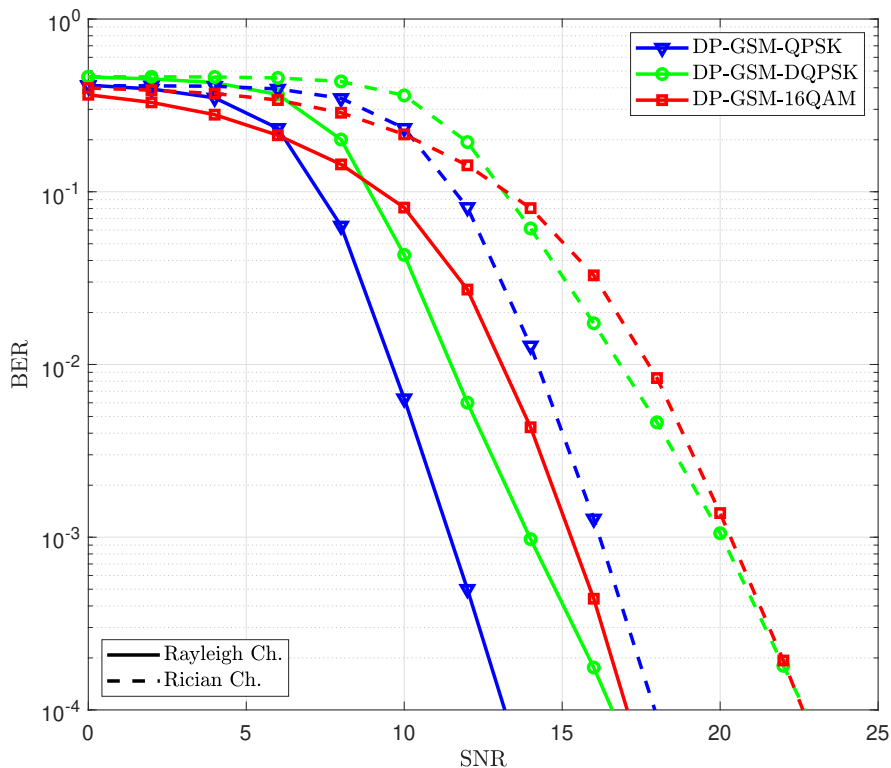
In this section, we evaluate the proposed DP-GSM system in terms of BER (bit-error-rate) and different values of signal-to-noise ratio (SNR) using Monte Carlo simulations over correlated/uncorrelated Rayleigh and Rician channel with different values of β , μ and different amplitude and phase modulation (APM): QPSK, DPSK and 16QAM. For QPSK and DPSK modulations, we choose the configuration ($N_t = 8$, $N_a = 4$, $N_r = 4$). For 16QAM, it is ($N_t = 5$, $N_a = 3$, $N_r = 4$). The SE for all these systems with QPSK, DPSK and 16QAM is in the order of 18 bpcu. Moreover, the corresponding data rate is estimated with a total system bandwidths of 50 GHz which is available in the band between 90 GHz and 200 GHz. The current configuration for DP-GSM systems can reach up to 750 Gbps (~ 0.75 Tbps) for (D)QPSK and 16QAM when the considered total system bandwidth, after channel aggregation and bounding is 50 GHz with 0.2 rolloff factor for the pulse shaping. The simulation parameters, the data rates estimation using DP-GSM is summarized in table 6. In all our simulations, the Rician factor K is set to 3 and the polarization correlation for the transmit and the receive components are chosen identical $|\gamma_t| = |\gamma_r| = 0.1$.

In figure 48, the performance of different APMs are evaluated over uncorrelated Rayleigh and uncorrelated Rician channel. As it can be shown, the QPSK outperforms the other modulations followed by DQPSK for both cases Rayleigh and Rician channel. It is worth noticing that uncorrelated Rayleigh fading channel gives better performance than in the uncorrelated Rician fading channel. So, for the same BER (10^{-4}) the required SNR in Rician channel is higher (about 4-5 dB) than that in Rayleigh channel. The performance of different APMs are evaluated over correlated Rayleigh channel (see Fig 49) and correlated Rician channel (see Fig 50) with different correlation levels $\beta = \{0.2, 0.5, 0.8\}$. The parameter μ is fixed to 0.2. The results show that we have a good performance with low spatial correlation level and the performance degrades as β value increases. With Rayleigh channel, the performances are much better than in Rician channel. For both channels, we have the same behavior as Fig. 48 which is that QPSK performance with DP-GSM system outperform all the others simulated modulations similar to the conclusion drawn with UP-GSM systems in sub-THz environment [95].

To further illustrate the potential of DP-GSM with the MOB-MMSE detector, the ML detector is compared with our approach. Figure 53 shows the simulation results of the DP-

Table 6: Simulation parameters and a sub-THz system example.

APM	DP-GSM configuration
QPSK	$N_t = 8, N_a = 4, N_r = 4$
DQPSK	$N_t = 8, N_a = 4, N_r = 4$
16QAM	$N_t = 5, N_a = 3, N_r = 4$
Parameters for sub-THz System example	Value
Carrier frequency (GHz)	150
Channel bandwidth (GHz)	0.50
Spectral Efficiency (bpcu)	18
Pulse Shaping: Rolloff	Root Raise cosine:0.2
Spectral efficiency (b/s/Hz)	15
Data Rates per Channel (Gbps)	7.5
Data Rates with 50 GHz (Gbps)	750

Figure 48: BER performance of $N_r \times N_t$ DP-GSM system with power leakage parameter $\mu = 0.2$ and different APMs (QPSK, DPSK, 16QAM) over uncorrelated Rayleigh channel (Solid line) and uncorrelated Rician channel (Dashed line). The spectral efficiency is 18bpcu.

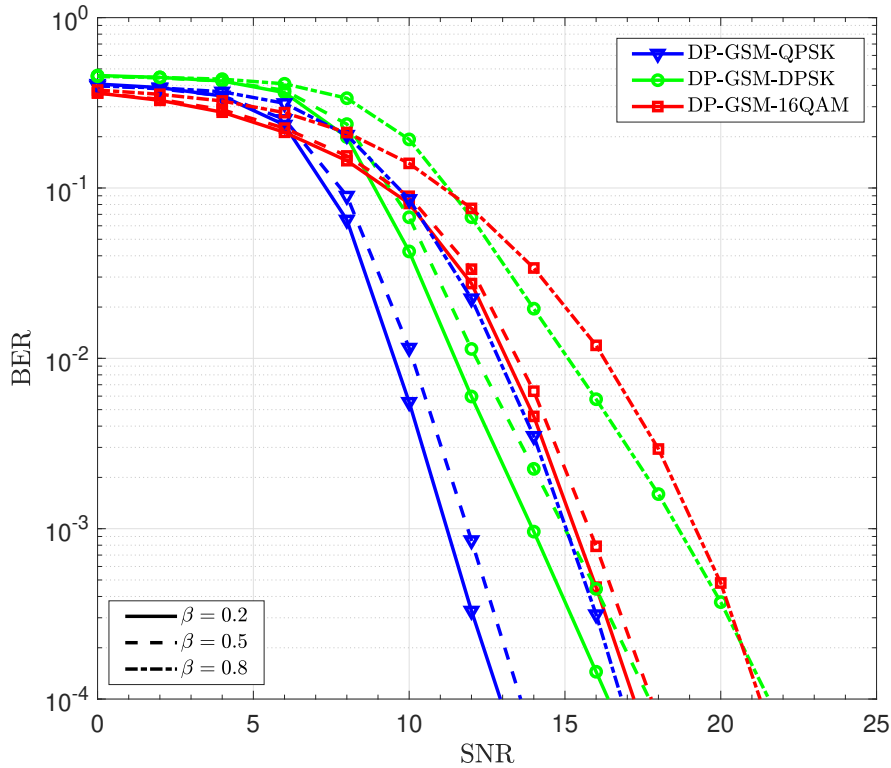


Figure 49: BER performance of $N_r \times N_t$ DP-GSM system with spatial correlation $\beta \in \{0.2, 0.5, 0.8\}$, power leakage parameter $\mu = 0.2$ and different APMs (QPSK, DPSK, 16QAM) over a correlated Rayleigh channel. The spectral efficiency is 18bpcu.

GSM system over correlated Rayleigh channel (solid lines) and correlated Rician channel (dashed lines) for QPSK with MOB-MMSE and ML detectors. The spatial correlation is chosen $\beta = \{0.2, 0.8\}$ and $\mu = 0.2$. As it is shown in Fig. 53 there is quite acceptable difference of (1 – 2.5) dB between ML and MOB-MMSE at the BER of 10^{-4} . Thus, the MOB-MMSE for DP-GSM system can achieve near-ML performance with low complexity.

Finally, the DP-SMX and the UP-GSM are compared with the DP-GSM system. We recall the reader that the SMX is a particular case of the GSM technique where symbols are transmitted simultaneously from N_t TAs to N_r receive antennas and all the TAs are activated (here $N_a=N_t$). Note that DP-GSM is compared to the best uni-polarized candidate mainly UP-GSM with QPSK and not to SMX, because it was shown in [96] that UP-GSM with QPSK in sub-THz channels has better performance, lower power consumption and detection complexity, and smaller transmitter/receiver antenna array to attain same SE compared to SMX with QPSK. In the DP-SMX system, all transmit and receive antennas use dual polarization to convey simultaneously different symbols on each polarization. The comparison is made using different spatial correlation configurations, $\beta \in \{0.2, 0.8\}$, and under different fading channels, Rayleigh and Rician channel. The first comparison is made between the DP-GSM and the UP-GSM. The number of antennas for UP-GSM and DP-GSM are $N_t^{UP} = 16$, $N_a = 4$, $N_r^{UP} = 8$ and $N_t = 8$, $N_a = 4$, $N_r = 4$, respectively, to have same SE given by 18bpcu and same number of RF chains. It can be seen in Fig. 54 that the performance of UP-GSM and DP-GSM are close with a small SNR gain for DP-GSM. In all cases, the DP-GSM allows to have a more compact antenna array physical size compared to UP-GSM, which is

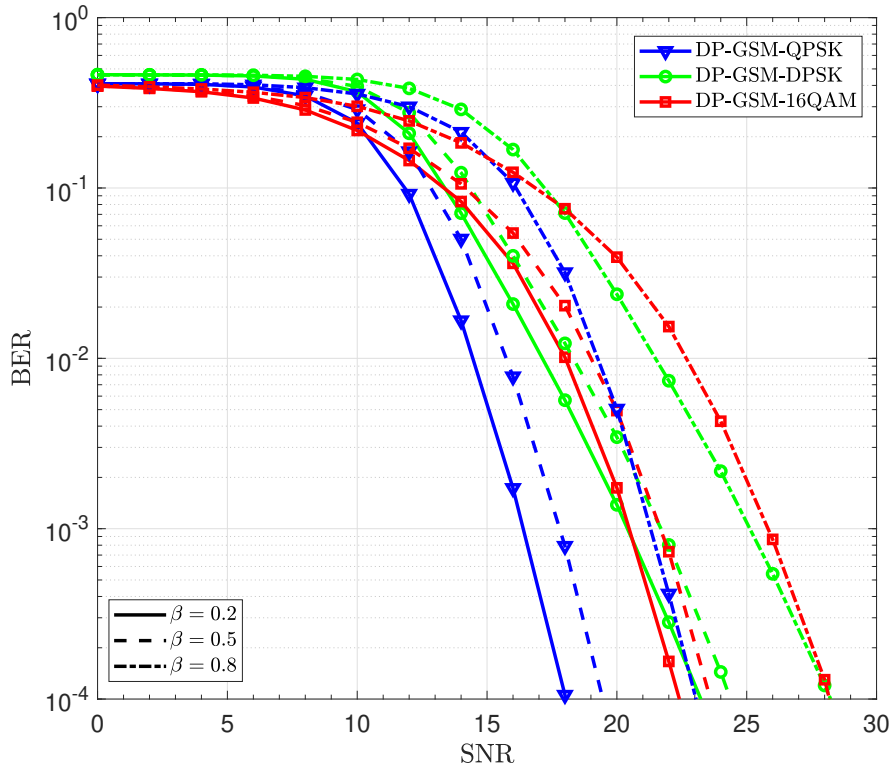


Figure 50: BER performance of $N_r \times N_t$ DP-GSM system with spatial correlation $\beta \in \{0.2, 0.5, 0.8\}$, power leakage parameter $\mu = 0.2$ and different APMs (QPSK, DPSK, 16QAM) over correlated Rician channel ($K = 3$). The spectral efficiency is 18bpcu.

crucial for UE. The second comparison is made between the DP-GSM and DP-SMX using the optimal ML detector where the number of antennas for both systems are respectively, $N_t = 5, N_a = 3, N_r = 3$ and $N_t = 3, N_r = 3$, to have same SE given by 12bpcu and same number of activated TAs for a fair comparison. Figure 55 shows clearly

that the DP-GSM and the DP-SMX have the same performance with the ML detector in low spatial correlation and for both fading channels. In the context of high spatial correlation, the DP-GSM outperforms the DP-SMX in both channels and the SNR difference between them is about $1 - 1.5$ dB at a BER of 10^{-4} .

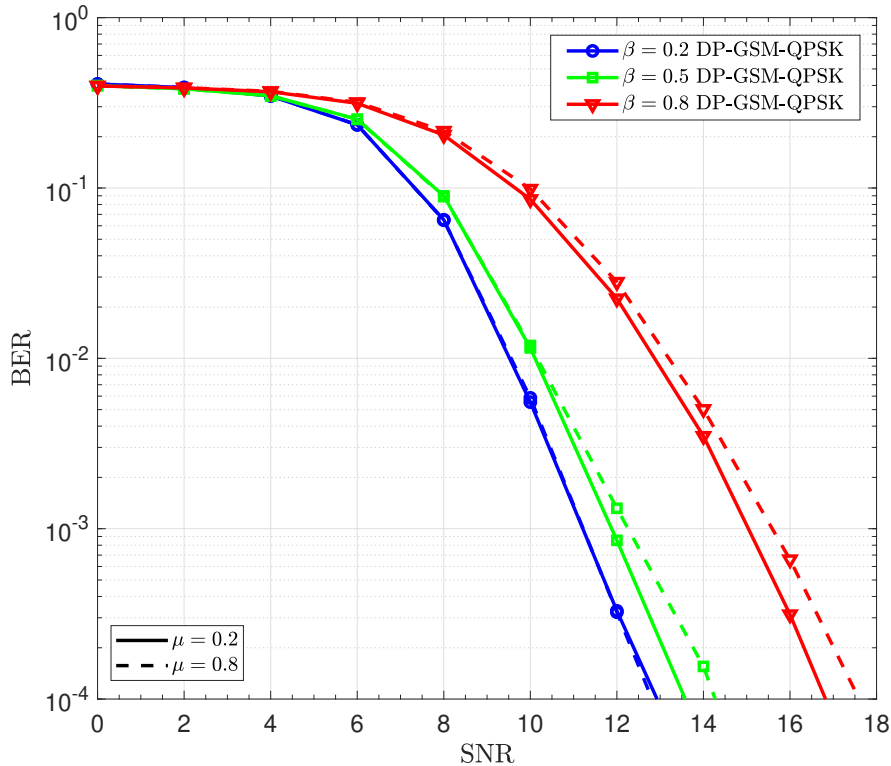


Figure 51: BER performance of $N_r \times N_t$ DP-GSM system with spatial correlation $\beta \in \{0.2, 0.5, 0.8\}$ and power leakage parameter $\mu = \{0.2, 0.8\}$ for QPSK over correlated Rayleigh channel. The spectral efficiency is 18bpcu for $N_t = 8$, $N_a = 4$ and $N_r = 4$.

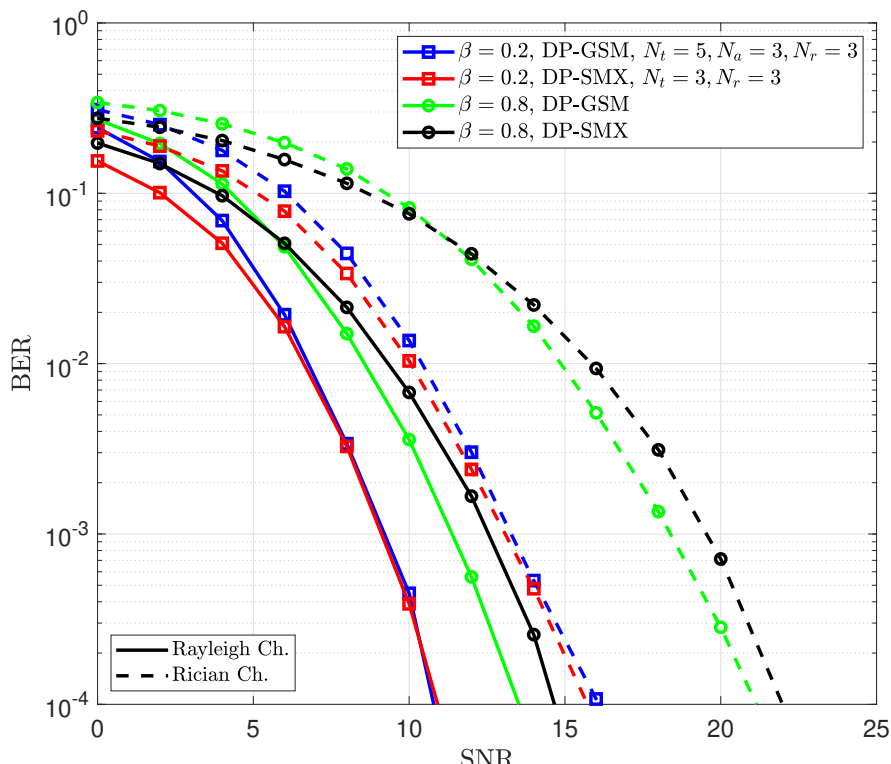


Figure 55: BER performance comparison of DP-GSM and DP-SMX systems with spatial correlation $\beta \in \{0.2, 0.8\}$ and power leakage $\mu = 0.2$ over correlated Rayleigh channel (Solid line) and correlated Rician channel (Dashed line) for QPSK using ML detector. The spectral efficiency is 12bpcu.

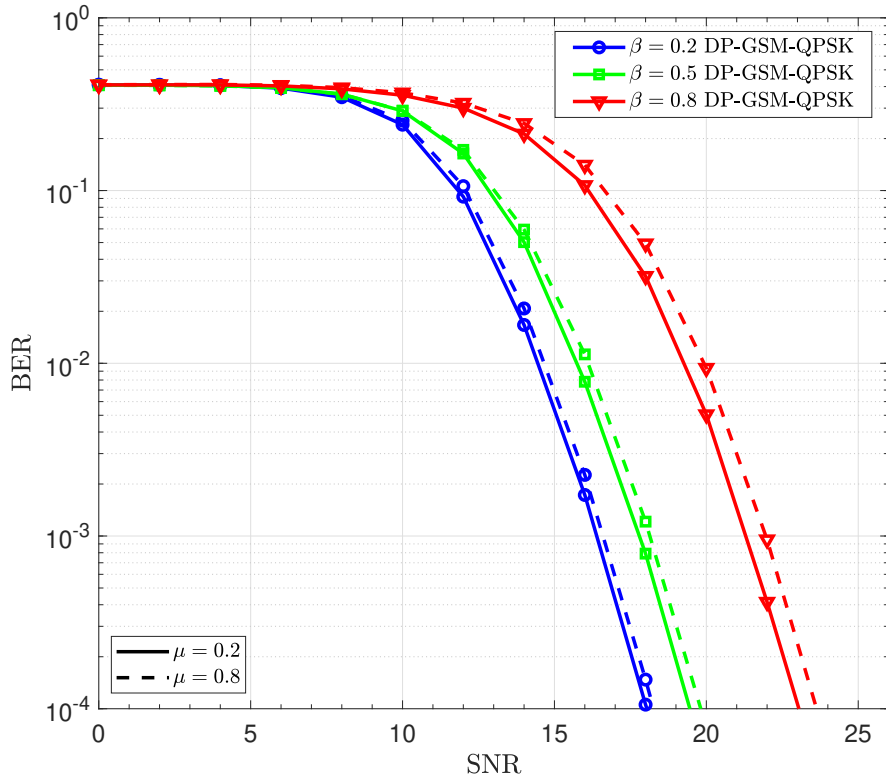


Figure 52: BER performance of $N_r \times N_t$ DP-GSM system with spatial correlation $\beta \in \{0.2, 0.5, 0.8\}$ and power leakage parameter $\mu = \{0.2, 0.8\}$ for QPSK over correlated Rician channel ($K = 3$). The spectral efficiency is 18bpcu for $N_t = 8$, $N_a = 4$ and $N_r = 4$.

5.4.7 Performance with real sub-THz MIMO Channel

In this work we extended our analysis using a more realistic channel different from that presented in (85). In hereafter we compare the performance of the DP-SMX and the UP-GSM systems using a ray-based deterministic channel modelling for sub-THz band (90-200 GHz) developed in [3]. In this channel model, the propagation takes into account several elements such as: material properties, gas attenuation, more propagation paths and new scattered paths. In addition, it characterizes the main channel properties such as path loss and delay spread for LOS, NLOS with vegetation and NLOS cases for indoor in-office and outdoor in-street scenarios. In this subsection, we adopt the downlink hotspot (or kiosk) indoor scenario where the Base Stations (BS), acting as transmitters, and the User Equipment (UE), acting as receivers, are equipped with N_t and N_r DP antennas. Figure 56 provides a description of a scenario where the 10 BSs are marked in red and distributed throughout the room, and the 50 UEs are highlighted with yellow circles.

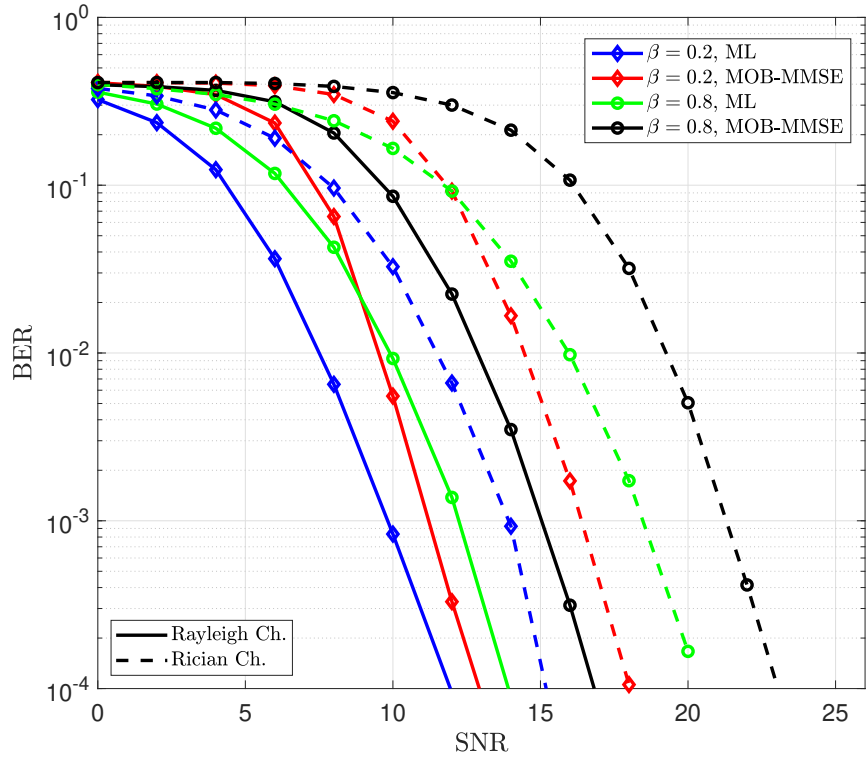


Figure 53: BER performance comparison of $N_r \times N_t$ DP-GSM system with spatial correlation $\beta \in \{0.2, 0.5, 0.8\}$ and power leakage parameter $\mu = 0.2$ for QPSK over correlated Rayleigh channel (Solid line) and correlated Rician channel (Dashed line) using for both channels MOB-MMSE and ML detectors. The spectral efficiency is 18bpcu.

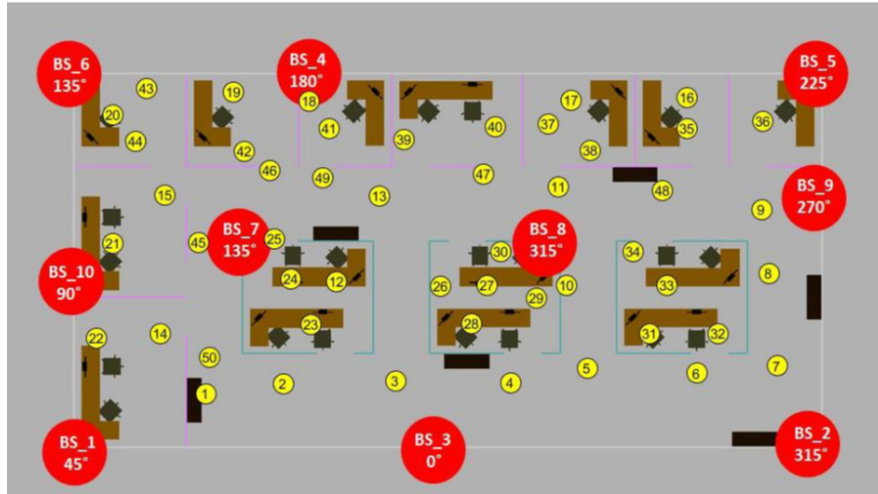


Figure 56: In-door MIMO channel measurements [3].

The corresponding MIMO channels are obtained using the ray-based deterministic channel modeling simulator. Here, Uniform-Linear-Array (ULA) is considered with antenna element separation of 4λ for a lower spatial correlation, where λ is the wavelength. The considered range for UE is going from 2m to 8m, i.e., we use in average a 5m separation distance between UE and BS.

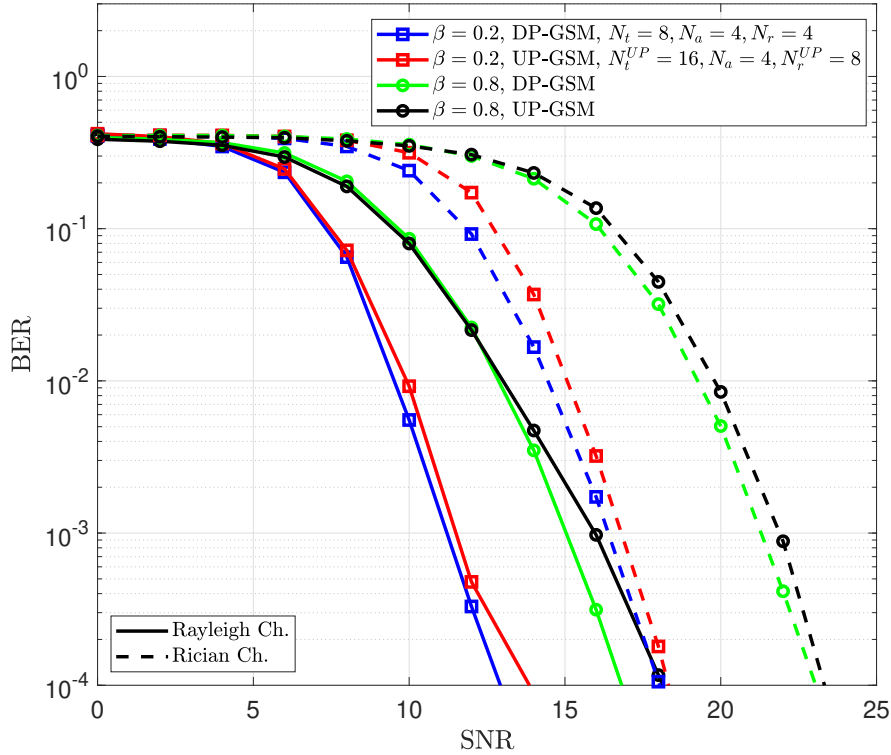


Figure 54: BER performance comparison of $N_r \times N_t$ DP-GSM and $2N_r \times 2N_t$ UP-GSM system with spatial correlation $\beta \in \{0.2, 0.8\}$ and power leakage $\mu = 0.2$ over correlated Rayleigh channel (Solid line) and correlated Rician channel (Dashed line) for QPSK using MOB-MMSE detector. The spectral efficiency is 18bpcu.

For a fair comparison, the DP-SMX and the UP-GSM are compared with the DP-GSM system under the same SE which is 12bpcu using same detector, same number of activated TA and number of RF chains. The following configurations are adopted: for DP-GSM ($N_t = 5, N_a = 3, N_r = 3$), for DP-SMX ($N_t = 3, N_r = 3$) and UP-GSM ($N_t^{UP} = 10, N_a = 3, N_r^{UP} = 6$). Figure 57, shows such a comparison using the ML detector for the three systems. It can be seen that the DP-GSM and DP-SMX have nearly the same performance and they outperform the UP-GSM with a difference of 1.25 dB at the BER of 10^{-4} (see solid lines). Moreover, when the number of DP receive antennas increases: $N_r = 5$ for both DP-GSM and DP-SMX, and $N_r^{UP} = 10$ for UP-GSM, the performances of the three systems improve and the DP-GSM and DP-SMX systems always keep their superiority compared to UP-GSM.

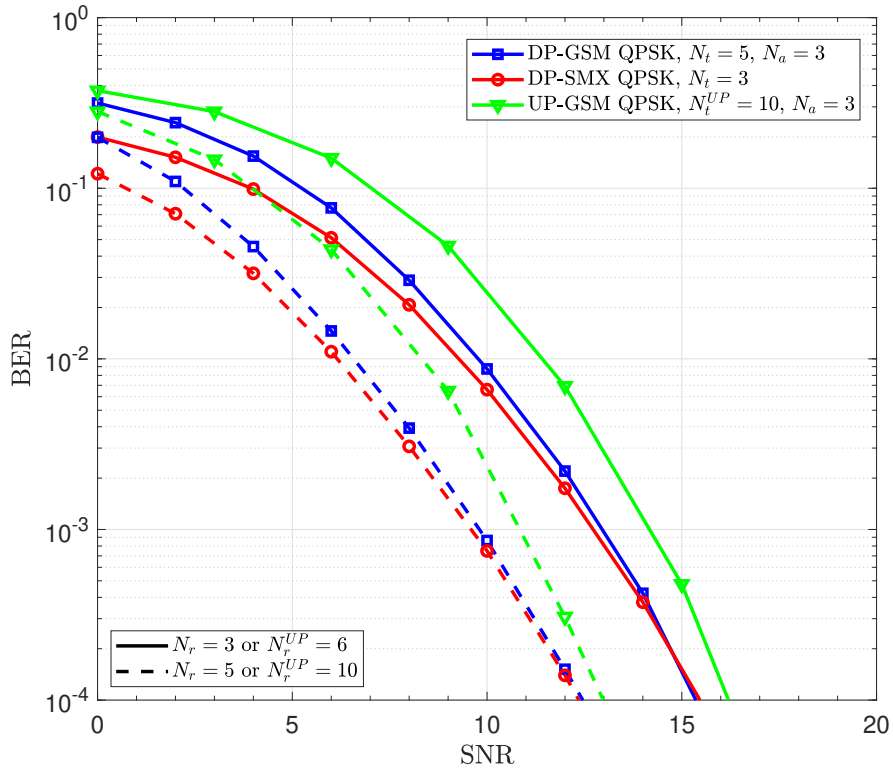


Figure 57: BER performance of DP-GSM, DP-SMX and UP-GSM systems from sub-THz measurements for QPSK using ML detector. The concerned sub-THz indoor MIMO channels are generated using ULA array geometry with 4λ antenna separation. The spectral efficiency is 12bpcu.

5.5 General conclusions

In this Subsection, the deployment of the dual polarized antennas leads to the increase of the SE. Therefore, a new polarization dimension is added in the form of $N_a \log_2(N_p)$. For the detection of the activated antennas indices, their polarization and the transmitted complex symbols for DP-GSM system, a modified OB-MMSE is proposed and applied for the signal detection. In addition, the combination of GSM with DP antennas is evaluated over uncorrelated/correlated Rayleigh and Rician channels. The DP-GSM system offer the opportunities to be more robust against channel deficiency such as Rician fading and inter-antenna correlation, and to be beneficial for improving the space and the SE. The results of comparison with the DP-SMX and UP-GSM systems using both theoretical and sub-THz deterministic fading channel model reveal that DP-GSM has a performance close to the other systems for low spatial correlation. However, it outperforms them at high spatial correlations. The DP-GSM is a promising candidate for ultra-high wireless data rates communication in sub-THz band.

6 Deliverable final conclusions

A first and very important result from the work undertaken in WP2 and included in deliverable D2.1 is the achievement in developing tools validated with measurements at 28 GHz and 60 GHz that have been used to analyze propagation channels at 150 GHz. Both back-haul and access links, have been considered at 4 different heights. Various scenarios like urban canyon, residential and main street with different link distances have been explored and analysed. As a main observation, the channel at 150 GHz does not necessarily benefit from better conditions at higher node heights (as usually observed at lower frequencies). It can behave significantly different depending on the height of the nodes, power and angular sensitivity of the receiver and the considered transmit power.

Beside the very significant influence of the vegetation on the in-street signal blockage, it's highly important to notice that the foliage scattering is likely not a dominant or strong component in the sub-THz channel, but it leads to some delay and angular diversity that may not be negligible when the LoS path is obstructed. However this has not been modeled yet, the wind and foliage diffusion surely introduces some time-variant fading and Doppler into the propagation channel. Therefore, accurate vegetation representations using for instance LiDAR data must be considered for physical-layer evaluations. As future focus this last must be validated later by launching future measurements.

The second important achieved result in this technical deliverable D2.1, is that we have been able (see results in Section 3 and in Section 4) to address the critical problem of phase noise (PN) modeling for sub-THz communications. We have first introduced two PN models: one correlated, accurate but complex, and another uncorrelated analytically simpler. We have been able to demonstrate that the Gaussian PN model is accurate when the oscillator corner frequency remains small compared to the system bandwidth. Achieved results in Section 3, have shown that an uncorrelated Gaussian process is an appropriate PN model for sub-THz communication systems. A practical application of model selection has been presented with a link adaptation scheme where the transceiver selects the most robust modulation between a coherent and a differential one with regard to the PN performance.

Following the previously analysed points related to PN, we introduced in Section 4 the system model for sub-THz communication systems. A LoS propagation channel has been considered and the oscillator PN has been described by a Gaussian process.

We have investigated the design of robust communications impaired by strong PN for future sub-THz applications. We have developed a pragmatic approach supported by a theoretical framework. This problem has been addressed in three steps: the characterization of the PN channel, the design of receiver algorithms, and the optimization of the modulation scheme. we also addressed the design of the optimum demodulation scheme for the GPN channel. The polar metric has been derived as a symbol detection scheme minimizing the error probability. A low-complexity implementation of the soft-output demapper using the polar metric for probabilistic channel decoding provided very encouraging results.

In addition to this last achievement, a mathematical framework based on a signal decomposition in polar coordinates, has been presented to design robust constellations and also to evaluate state-of-the-art solutions. We have compared the proposed Polar-QAM modulation to conventional solutions in the scientific literature on different performance metrics such

as the PAPR, the BER, or the achievable rate. Provided results highlight the important performance gains realized by the Polar-QAM in comparison to conventional schemes. In contrast to state-of-the-art optimized constellations, the advantage of the proposed solution is that near-optimal performance is achieved with significant complexity reductions of the transceiver. Designed schemes offer "avant garde" results and valuable low-complexity solutions for the future development of sub-THz systems.

Last important achievements are related with the development of the Generalized Spatial Modulation (GSM) MIMO System scheme for Sub-THz communications. In Section 5.2, we proposed a novel scheme to reach the ultra-high data rates in the order of Tb/s with low power consumption. It is based on using power efficient modulation like constant or near-constant envelope modulation (CPM and (D)QPSK) with GSM or any index modulation that can increase the system spectral efficiency and conserve the power efficiency. Proposed scheme proves that the constant or near-constant envelope modulation CPM-GSM and (D)QPSK-GSM systems with limited number of RF chains, feasible antenna array size, and acceptable complexity are able to reach a high system spectral efficiency $\approx 25\text{b/s/Hz}$, and hence ultra-high data rates while maintaining a low power consumption.

In order to enhance the BER performance of GSM in these channels, we focused in Section 5.3 on two aspects: the legitimate TAC selection and the spatial bit mapping that was ignored in conventional GSM. Firstly, we proposed a TAC selection method without instantaneous CSI (S-EGSM) for highly correlated channels, where we consider only the transmit spatial correlation which is the dominant term in the channel. The simulation results show that S-EGSM outperforms the other no CSI-based methods in highly correlated channel by 1.4 dB. This gain is less significant when the correlation factor becomes low. Next, we proposed the Gray coding for spatial bits in GSM that permits to limit the number of different bits between neighbor TACs to one bit. Achieved results showed that the Gray-based mapping method outperforms the normal binary spatial mapping by 1.5 dB in highly correlated channels. Last but not least, the deployment of the dual polarized antennas in GSM (DP-GSM) allows to add an additional level of indexation and leads to the increase of the SE. The DP-GSM system offers the opportunities to be more robust against channel deficiencies such as Rician fading and inter-antenna correlation and to be beneficial for the SE (see main results in Section 5.4). Obtained results of comparing the DP-SMX and UP-GSM systems in sub-THz deterministic fading channel model reveal that DP-GSM has a performance close to the other systems for low spatial correlation.

References

- [1] S. Li, D. Fritzsche, C. Carta, and F. Ellinger, “A 200-GHz Sub-Harmonic Injection-Locked Oscillator with 0-dBm Output Power and 3.5DC-to-RF-Efficiency,” in *2018 IEEE Radio Frequency Integrated Circuits Symposium (RFIC)*, June 2018, pp. 212–215.
- [2] A. Ugolini, A. Piemontese, and T. Eriksson, “Spiral Constellations for Phase Noise Channels,” *IEEE Transactions on Communications*, pp. 1–1, 2019.
- [3] M. G. Gougeon, Y. Corre, and M. Z. Aslam, in *IEEE 30th International Symposium on Personal, Indoor and Mobile Radio Communications (PIMRC Workshops), Istanbul, Turkey*.
- [4] BRAVE, “Deliverable D2.0, Propagation channel model and RF impairments definition,” Tech. Rep., February 2019.
- [5] Telecom Infra Project, “Study of mmWave Signal Propagation in Non-line-of-sight Environment,” Tech. Rep., 2019.
- [6] M. Z. Aslam, Y. Corre, J. Belschner, G. S. Arockiaraj, and M. Jäger, “Analysis of 60-ghz in-street backhaul channel measurements and lidar ray-based simulations,” in *14th European Conference on Antennas and Propagation (EuCAP), Copenhagen, Denmark*, March 2020.
- [7] Telecom Infra Project, “mmWave Measurement Campaign using Terragraph Channel Sounders,” Tech. Rep., 2019.
- [8] Y. Corre and Y. Lostanlen, “Three-dimensional urban em wave propagation model for radio network planning and optimization over large areas,” *IEEE Transactions on Vehicular Technology*, 2009.
- [9] J. Stephan and Y. Corre, R. Charbonnier, and Y. Lostanlen, “Increased reliability of outdoor millimeter-wave link simulations by leveraging lidar point cloud,” in *12th European Conference on Antennas and Propagation (EuCAP), London, UK*, April 2018.
- [10] G. Gougeon, Y. Corre, and M. Z. Aslam, “Sub-thz channel characterization from ray-based deterministic simulations,” *ITU Journal: ICT Discoveries*, vol. 2, no. 1, 11 2019.
- [11] ITU, “Recommendation ITU-R P.833-9, Attenuation in vegetation,” Tech. Rep., September 2016.
- [12] F. T. Ulaby, T. E. Van Deventer, J. R. East, T. F. Haddock, and M. E. Coluzzi, “Millimeter-wave bistatic scattering from ground and vegetation targets,” *IEEE Transactions on Geoscience and Remote Sensing*, vol. 26, no. 3, pp. 229–243, 1988.
- [13] F. K. Schwering, E. J. Violette, and R. H. Espeland, “Millimeter-wave propagation in vegetation: experiments and theory,” *IEEE Transactions on Geoscience and Remote Sensing*, vol. 26, no. 3, pp. 355–367, 1988.



- [14] M. Voicu, D. Pepe, and D. Zito, "Performance and Trends in Millimetre-Wave CMOS Oscillators for Emerging Wireless Applications," *International Journal of Microwave Science and Technology*, vol. 2013, p. 6, 2013. [Online]. Available:
- [15] C. Hager, A. G. i Amat, A. Alvarado, and E. Agrell, "Design of APSK Constellations for Coherent Optical Channels with Nonlinear Phase Noise," *IEEE Transactions on Communications*, vol. 61, no. 8, pp. 3362–3373, August 2013. [Online]. Available:
- [16] G. J. Foschini, R. D. Gitlin, and S. B. Weinstein, "On the selection of a two-dimensional signal constellation in the presence of phase jitter and gaussian noise," *The Bell System Technical Journal*, vol. 52, no. 6, pp. 927–965, July 1973. [Online]. Available:
- [17] M. R. Khanzadi, D. Kuylenstierna, A. Panahi, T. Eriksson, and H. Zirath, "Calculation of the Performance of Communication Systems From Measured Oscillator Phase Noise," *IEEE Transactions on Circuits and Systems I: Regular Papers*, vol. 61, no. 5, pp. 1553–1565, May 2014. [Online]. Available:
- [18] H. Mehrpouyan, M. R. Khanzadi, M. Matthaieu, A. M. Sayeed, R. Schober, and Y. Hua, "Improving bandwidth efficiency in E-band communication systems," *IEEE Communications Magazine*, vol. 52, no. 3, pp. 121–128, March 2014.
- [19] A. Demir, "Computing Timing Jitter From Phase Noise Spectra for Oscillators and Phase-Locked Loops With White and 1/f Noise," *IEEE Transactions on Circuits and Systems I: Regular Papers*, vol. 53, no. 9, pp. 1869–1884, Sept 2006. [Online]. Available:
- [20] N. J. Kasdin and T. Walter, "Discrete simulation of power law noise [for oscillator stability evaluation]," in *Proceedings of the 1992 IEEE Frequency Control Symposium*, May 1992, pp. 274–283. [Online]. Available:
- [21] L. Pometcu and R. D'Errico, "Characterization of Sub-THz and mmWave Propagation Channel for Indoor Scenarios," in *12th European Association on Antennas and Propagation (EurAAP 18)*, Apr 2018.
- [22] M. Martalo, C. Tripodi, and R. Raheli, "On the information rate of phase noise-limited communications," in *2013 Information Theory and Applications Workshop (ITA)*, Feb 2013, pp. 1–7.
- [23] R. Krishnan, A. G. i Amat, T. Eriksson, and G. Colavolpe, "Constellation Optimization in the Presence of Strong Phase Noise," *IEEE Transactions on Communications*, vol. 61, no. 12, pp. 5056–5066, December 2013. [Online]. Available:
- [24] S. Bicaïs, J.-B. Doré, and J.-L. Gonzalez Jimenez, "On the Optimum Demodulation in the Presence of Gaussian Phase Noise," in *2018 International Conference on Telecommunications (ICT)*, June 2018.
- [25] T. Moon and W. Stirling, *Mathematical Methods and Algorithms for Signal Processing*. Prentice Hall, 2000. [Online]. Available:

- [26] J.-B. Doré, Y. Corre, S. Bicaïs, J. Palicot, E. Faussurier, D. Kténas, and F. Bader, “Above-90GHz Spectrum and Single-Carrier Waveform as Enablers for Efficient Tbit/s Wireless Communications,” in *25th International Conference on Telecommunications (ICT’2018)*, Saint-Malo, France, Jun. 2018. [Online]. Available:
- [27] S. Bicaïs, J.-B. Doré, and J.-L. Gonzalez Jimenez, “Adaptive PSK Modulation Scheme in the Presence of Phase Noise,” in *2018 Signal Processing Advances in Wireless Communications (SPAWC)*, June 2018.
- [28] S. Mumtaz, J. Jornet, J. Aulin, W. Gerstacker, X. Dong, and B. Ai, “Terahertz Communication for Vehicular Networks,” *IEEE Transactions on Vehicular Technology*, vol. 66, pp. 5617–5625, 07 2017.
- [29] F. Kayhan and G. Montorsi, “Constellation design for channels affected by phase noise,” in *2013 IEEE International Conference on Communications (ICC)*, June 2013, pp. 3154–3158. [Online]. Available:
- [30] L. Pometcu and R. D’Errico, “Channel Model Characteristics in D-Band for NLOS Indoor Scenarios,” *2019 13th European Conference on Antennas and Propagation (EuCAP)*, pp. 1–4, 2019. [Online]. Available:
- [31] G. Gougeon, Y. Corre, and M. Z. Aslam, “Ray-based Deterministic Channel Modelling for sub-THz Band,” in *2019 IEEE International Symposium on Personal, Indoor and Mobile Radio Communications (PIMRC)*, Sep. 2019. [Online]. Available:
- [32] A. Garcia Armada, “Understanding the effects of phase noise in orthogonal frequency division multiplexing (OFDM),” *IEEE Transactions on Broadcasting*, vol. 47, no. 2, pp. 153–159, 2001.
- [33] O. Tervo, T. Levanen, K. Pajukoski, J. Hulkkonen, P. Wainio, and M. Valkama, “5G New Radio Evolution Towards Sub-THz Communications,” 2020.
- [34] S. Bicaïs and J.-B. Doré, “Phase Noise Model Selection for Sub-THz Communications,” in *2019 IEEE Global Communication Conference (GLOBECOM)*, December 2019.
- [35] J. Proakis, *Digital Communications 5th Edition*, ser. McGraw-Hill series in electrical and computer engineering : communications and signal processing. McGraw-Hill, 2007.
- [36] R. Krishnan, M. R. Khanzadi, T. Eriksson, and T. Svensson, “Soft metrics and their Performance Analysis for Optimal Data Detection in the Presence of Strong Oscillator Phase Noise,” *CoRR*, vol. abs/1310.1638, 2013. [Online]. Available:
- [37] F. Tosato and P. Bisaglia, “Simplified soft-output demapper for binary interleaved COFDM with application to HIPERLAN/2,” in *2002 IEEE International Conference on Communications. Conference Proceedings. ICC 2002 (Cat. No.02CH37333)*, vol. 2, 2002, pp. 664–668 vol.2. [Online]. Available:
- [38] J. hoon Lee and H. Chung, “Exact and approximate log-likelihood ratio of M-ary QAM with two-time dimensions,” *ICT Express*, vol. 5, no. 3, pp. 173 – 177, 2019. [Online]. Available:



- [39] 3rd Generation Partnership Project (3GPP), “Overall Description Stage 2,” Technical Specification Group Access Network 38.300, 12 2017, 2.0.0.
- [40] R. Hadani, S. Rakib, M. Tsatsanis, A. Monk, A. J. Goldsmith, A. F. Molisch, and R. Calderbank, “Orthogonal Time Frequency Space Modulation,” in *2017 IEEE Wireless Communications and Networking Conference (WCNC)*, March 2017, pp. 1–6. [Online]. Available:
- [41] S. M. Kay, *Fundamentals of Statistical Signal Processing: Estimation Theory*. Upper Saddle River, NJ, USA: Prentice-Hall, Inc., 1993.
- [42] J. Horton Conway and N. Sloane, *Sphere Packings, Lattices and Groups*, 01 1988, vol. 290. [Online]. Available:
- [43] G. Forney, R. Gallager, G. Lang, F. Longstaff, and S. Qureshi, “Efficient Modulation for Band-Limited Channels,” *IEEE Journal on Selected Areas in Communications*, vol. 2, no. 5, pp. 632–647, Sep 1984. [Online]. Available:
- [44] M. Simon and J. Smith, “Hexagonal multiple phase-and-amplitude-shift-keyed signal sets,” *IEEE Transactions on Communications*, vol. 21, no. 10, pp. 1108–1115, Oct 1973. [Online]. Available:
- [45] D. M. Arnold, H. Loeliger, P. O. Vontobel, A. Kavcic, and W. Zeng, “Simulation-Based Computation of Information Rates for Channels With Memory,” *IEEE Transactions on Information Theory*, vol. 52, no. 8, pp. 3498–3508, Aug 2006.
- [46] M. A. Tariq, H. Mehrpooyan, and T. Svensson, “Performance of circular QAM constellations with time varying phase noise,” in *2012 IEEE 23rd International Symposium on Personal, Indoor and Mobile Radio Communications - (PIMRC)*, Sep. 2012, pp. 2365–2370.
- [47] Z. Liu, Q. Xie, K. Peng, and Z. Yang, “APSK Constellation with Gray Mapping,” *IEEE Communications Letters*, vol. 15, no. 12, pp. 1271–1273, December 2011.
- [48] F. Schreckenbach, N. Gortz, J. Hagenauer, and G. Bauch, “Optimization of symbol mappings for bit-interleaved coded modulation with iterative decoding,” *IEEE Communications Letters*, vol. 7, no. 12, pp. 593–595, Dec 2003.
- [49] S. Allpress, C. Luschi, and S. Felix, “Exact and approximated expressions of the log-likelihood ratio for 16-QAM signals,” in *Conference Record of the Thirty-Eighth Asilomar Conference on Signals, Systems and Computers, 2004.*, vol. 1, Nov 2004, pp. 794–798 Vol.1. [Online]. Available:
- [50] A. Barre, E. Boutillon, N. Bias, and D. Diaz, “A polar-based demapper of 8PSK demodulation for DVB-S2 systems,” in *SiPS 2013 Proceedings*, Oct 2013, pp. 13–17. [Online]. Available:
- [51] T. Yoshida, K. Matsuda, K. Kojima, H. Miura, K. Dohi, M. Pajovic, T. Koike-Akino, D. S. Millar, K. Parsons, and T. Sugihara, “Hardware-efficient Precise and Flexible Soft-demapping for Multi-Dimensional Complementary APSK Signals,” in *ECOC 2016; 42nd European Conference on Optical Communication*, Sep. 2016, pp. 1–3.



- [52] M. Zhang and S. Kim, "Efficient soft demapping for M-ary APSK," in *ICTC 2011*, Sep. 2011, pp. 641–644.
- [53] H. Elayan, O. Amin, B. Shihada, R. M. Shubair, and M. Alouini, "Terahertz Band: The Last Piece of RF Spectrum Puzzle for Communication Systems," *IEEE Open Journal of the Communications Society*, vol. 1, pp. 1–32, 2020.
- [54] J. Groe, "Polar Transmitters for Wireless Communications," *IEEE Communications Magazine*, vol. 45, no. 9, pp. 58–63, September 2007. [Online]. Available:
- [55] C. T. Chen, C. H. Hsiao, T. S. Horng, and K. C. Peng, "Wireless polar receiver using two injection-locked oscillator stages for green radios," in *2011 IEEE MTT-S International Microwave Symposium*, June 2011, pp. 1–4. [Online]. Available:
- [56] A. Ghosh and et al., "Millimeter-wave enhanced local area systems: A high-data-rate approach for future wireless networks," *IEEE Transactions on Information Theory*, vol. 32, no. 6, pp. 1152 – 1163, June 2014.
- [57] I. 802.15.3d Standard Association, "IEEE Standard for High Data Rate Wireless Multi-Media Networks, Amendment 2:100 Gb/s Wireless Switched Point-to-Point Physical Layer," 2017.
- [58] I. 802.11ad Standard Association, "Amendment 3: Enhancements for Very High Throughput in the 60GHz Band," 2012.
- [59] I. 802.15.3e Standard Association, "IEEE Standard for High Data Rate Wireless Multi-Media Networks, Amendment 1: High-Rate Close Proximity Point-to-Point Communications," 2017.
- [60] M. Zhang and S. Kim, "Wireless D-band Communication up to 60 Gbit/s with 64QAM using GaAs HEMT technology," in *IEEE Radio and Wireless Symposium (RWS), 2016.*, 2016.
- [61] H. J. Song and T. Nagatsuma, "Present and future of terahertz communications," *IEEE Transactions on Terahertz Science and Technology.*, vol. 1, no. 1, 2011.
- [62] I. F. Akyildiz, J. M. Jornet, and C. Han, "Terahertz Band: Next Frontier for Wireless Communications," *Physical Communication (Elsevier) Journal.*, vol. 12, no. 1, 2014.
- [63] ——, "TeraNets: Ultra-broadband Communication Networks in the Terahertz Band," *IEEE Wireless Communications Magazine.*, vol. 21, no. 4, 2014.
- [64] J. Palicot and F. Bader, "Backing to Single Carrier in Tera Hertz Communications for Green Considerations," in *in Proc. of the 32nd International Union of Radio Science (URSI'2017) GASS. Montréal, Canada.*, Aug 2017.
- [65] R. D. L. Pometcu, "Characterization of Sub-THz and mmWave Propagation Channel for Indoor Scenarios," in *in the Proc. of the 12th European Association on Antennas and Propagation (EurAAP'18)*, April 2018.

- [66] N. Ishikawa, S. Sugiura, and L. Hanzo, “50 Years of Permutation, Spatial and Index Modulation: From Classic RF to Visible Light Communications and Data Storage,” *IEEE Communications Surveys and Tutorials.*, vol. 20, no. 3, 2014.
- [67] A. Younis, N. Serafimovski, R. Mesleh, and H. Haas,, “Characterization of Sub-THz and mmWave Propagation Channel for Indoor Scenarios,” in *in Proc. Signals, Syst. Comput.*, Apr Apr. 2018.
- [68] J. T. Wang, S. Y. Jia, and J. Song, “Generalised spatial modulation system with multiple active transmit antennas and low complexity detection scheme,” *IEEE Trans. Wireless Commun.*, vol. 11, no. 4, Apr. 2012.
- [69] E. Basar, U. Aygolu, E. Panayirci, and H. V. Poor, “Orthogonal Frequency Division Multiplexing With Index Modulation,” *IEEE Transactions on Signal Processing.*, vol. 61, no. 22, Apr 2013.
- [70] H. A. Ngo, C. Xu, S. Sugiura, and L. Hanzo, “Space-Time-Frequency Shift Keying for Dispersive Channels,” *IEEE Signal Processing Letters.*, vol. 18, no. 3, 2011.
- [71] L. D. Y. Xiao, Z. Yang, P. Yang, L. Yin, and W. Xiang, “Low-Complexity Signal Detection for Generalized Spatial Modulation,” *IEEE Communications Letters.*, vol. 18, no. 3, 2014.
- [72] R. Mesleh, H. Haas, S. Sinaovic, C. W. Ahn, and S. Yun, “Spatial modulation,” *IEEE Trans. Veh. Technol.*, vol. 57, no. 4, pp. 2228–2241, July 2008.
- [73] Y. A. Chau and S.-H. Yu, “Space modulation on wireless fading channels,” in *IEEE 54th Vehicular Technology Conference (VTC-Fall), Atlantic City, NJ, USA, Oct. 2001*, Oct 2001 Oct.2001.
- [74] J. Jeganathan, A. Ghayeb, and L. Szczecinski, “Generalized Space Shift Keying Modulation for MIMO Channels,” in *IEEE 19th International Symposium on Personal, Indoor and Mobile Radio Communications (PIMRC) 2008*, 2008.
- [75] S. L. Loyka, “Channel capacity of MIMO architecture using the exponential correlation matrix,” in *IEEE Commun. Lett.*, vol. 5, no. 9, pp. 369–371, Sept 2001.
- [76] A. Chatterjee, S. Chatterjee, and S. S. Das, “Evaluation of spatial correlation and its effect on channel capacity of uniform planar antenna array,” in *23rd National Conference on Communications (NCC), 2017*, 2017.
- [77] M. Koca and H. Sari, “Generalized spatial modulation over correlated fading channels: Performance analysis and optimization,” in *IEEE International Conference on Telecommunications (ICT), 2013*, 2013.
- [78] I. S. Association, “IEEE 802.15.3d TG3d Applications Requirements Document (ARD),” May 2015.
- [79] A. Ulusoy and H. Schumacher, “Multi-Gb/s Analog Synchronous QPSK Demodulator With Phase-Noise Suppression,” *IEEE Transactions on Microwave Theory and Techniques.*, vol. 60, no. 11, pp. 3591–3598, 2012.

- [80] N. Ishikawa, R. Rajashekhar, S. Sugiura, and L. Hanzo, "Generalized Spatial Modulation Based Reduced-RF-Chain Millimeter-Wave Communications," *IEEE Transactions on Vehicular Technology.*, vol. 66, no. 1, pp. 879–883, Jan. 2017.
- [81] S. K. G. Simha, N. Neha, M. Raghavendra, and U. Sripathi, "Redesigned Spatial Modulation for Spatially Correlated Fading Channels," in *Wireless Personal Communications, Springer Journal*, vol. 97, 5003–5030(2017), 2017.
- [82] L. X. et al., "Transmit Antenna Combination Optimization for Generalized Spatial Modulation Systems," in *IEEE Access*, vol. 6, pp. 41 866–41 882, Sept 2018.
- [83] "Back to Single-carrier for beyond-5G communications above 90 GHz-(BRAVE)," in *French funded project-ANR-17-CE25-0013*, vol. Available:<http://www.brave-beyond5g.com/>.
- [84] P. Yang, M. Di Renzo, Y. Xiao, S. Li, and L. Hanzo, "Design Guide-lines for Spatial Modulation," *IEEE Commun. Surv. Tuts.*, vol. 17, no. 1, pp. 6–26, Jan. 2014.
- [85] J. T. Wang, S. Y. Jia, and J. Song, "Generalised spatial modulation system with multiple active transmit antennas and low complexity detection scheme," *IEEE Trans. Wireless Commun.*, vol. 11, no. 4, pp. 1605–1615, Apr. 2012.
- [86] M. Di Renzo, H. Haas, A. Ghayeb, S. Sugiura, and L. Hanzo, "Spatial modulation for generalized MIMO: Challenges, opportunities, and implementation," *IEEE Trans. Wireless Commun.*, vol. 102, no. 1, pp. 56–103, Jan. 2014.
- [87] M. Saad, F. Bader, J. Palicot, A. C. A. Ghouwayel, and H. Hijazi, "Single Carrier with Index Modulation for Low Power Terabit Systems," in *2019 IEEE Wireless Communications and Networking Conference (WCNC), Marrakesh, Morocco*, 2019, pp. 1–7.
- [88] M. Saad, F. C. Lteif, A. C. Al Ghouwayel, H. Hijazi, J. Palicot, and F. Bader, "Generalized Spatial Modulation in Highly Correlated Channels," in *IEEE 30th International Symposium on Personal, Indoor and Mobile Radio Communications -PIMRC Workshops, Istanbul, Turkey*, 2019, pp. 1–6.
- [89] G. Zafari, M. Koca, and H. Sari, "Dual-Polarized Spatial Modulation Over Correlated Fading Channels," *IEEE Transactions on Communications*, vol. 65, no. 3, pp. 1336–1352, March 2017.
- [90] Y. Xiao, Z. Yang, L. Dan, P. Yang, L. Yin, and W. Xiang, "Low-Complexity Signal Detection for Generalized Spatial Modulation," *IEEE Communications Letters*, vol. 18, no. 3, pp. 1403–406, March 2014.
- [91] S. L. Loyka, "Channel capacity of MIMO architecture using the exponential correlation matrix," *IEEE Communications Letters*, vol. 5, pp. 369–371, Sept. 2001.
- [92] K. P. Liolis, J. Gomez-Vilardebo, E. Casini, and A. I. Perez-Neira, "Statistical Modeling of Dual-Polarized MIMO Land Mobile Satellite Channels," *IEEE Transactions on Communications*, vol. 58, no. 11, pp. 3077–3083, November 2010.



- [93] C. Oestges, B. Clerckx, M. Guillaud, and M. Debbah, “Dual-polarized wireless communications: from propagation models to system performance evaluation,” *IEEE Transactions on Communications*, vol. 7, no. 10, pp. 4019–4031, October 2008.
- [94] H. Asplund, J. Berg, F. Harrysson, J. Medbo, and M. Riback, “Propagation Characteristics of Polarized Radio Waves in Cellular Communications,” in *66th IEEE Vehicular Technology Conference (VTC)*, Baltimore, MD-USA, 2007, pp. 839–843.
- [95] M. Saad, A. F. Bader, C. Al Ghouwayel, H. Hijazi, N. Bouhel, and J. Palicot, “Generalized Spatial Modulation for Wireless Terabits Systems Under Sub-THZ Channel With RF Impairments,” in *IEEE International Conference on Acoustics, Speech and Signal Processing (ICASSP)*, Barcelona, Spain, 2020, pp. 5135–5139.
- [96] M. Saad, A. C. Al Ghouwayel, H. Hijazi, F. Bader, and J. Palicot, “MIMO Techniques for Wireless Terabits Systems under sub-THz Channel with RF Impairments,” in *IEEE International Conference on Communications -ICC*. Dublin, Ireland., 2020.